ISAS - INTERNATIONAL SCHOOL
FOR ADVANCED STUDIES

SLIM ACCRETION DISKS

Thesis submitted for the degree of
"Doctor Philosophiae"

Astrophysics Sector

Candidate:	Supervisor:
Ewa Szuszkiewicz	Prof. Marek A. Abramowicz

Academic Year 1987/88

TRIESTE

SISSA - SCUOLA
INTERNAZIONALE
SUPERIORE
DI STUDI AVANZATI
TRIESTE
Strada Costiera 11

SLIM
ACCRETION DISKS

Thesis submitted for the degree of
"Doctor Philosophiae"

Astrophysics Sector

Candidate:	Supervisor:
Ewa Szuszkiewicz	Prof. Marek A. Abramowicz

December 1988

Acknowledgements

I thank you so much

Contents

1. Introduction

Instead of making the usual sort of introduction, I would like to start by presenting two figures which sum up the main ideas of the thesis and give us overall guide to the work. Figure 1 illustrates observed properties of the objects discussed here while Figure 2 is its theoretical counterpart which summarizes all of the models calculated and described in detail in this thesis. In fact, the graphs really ought to be three dimensional, with a third axis representing viscosity and I will be considering various different viscosity parameters for the models represented in Figure 2. Both of the figures show relationships between mass and accretion rate, which having in mind connotations of accretion rate, translate into mass-luminosity relations. For normal stars the mass-luminosity relation is of fundamental importance and underlies our understanding of stellar structure and evolution. What is the present state of our knowledge about the nature of galactic and extragalactic x-ray sources? Here I will concentrate on Active Galactic Nuclei and introduce a new class of theoretical models for accretion disks - *slim accretion disks* (Abramowicz, Czerny, Lasota and Szuszkiewicz, 1988). The simplicity of these models combined with care in treating physical phenomena in the neighbourhood of compact objects, give rise to a powerful tool for exploration within this extremely interesting field.

The $\dot{M}(M)$ relation in Figure 1 has been obtained using data available in the literature. As a main source of masses and luminosities I used the paper by Padovani (1988) (a preprint of the Space Telescope Science Institute). and translated the luminosities into accretion rates using the $\dot{M} - L$ relation for slim disks. (The masses are measured in solar masses and the accretion rates in cgs units). The most interesting objects, which show evidence for the existence of accretion disks are represented in Figure 3, which shows a small part of the data in Figure 1. Among others there are Fairall 9, whose spectral properties I studied in collaboration with Binette, Prieto and Zheng (1988), NGC 1566, where disk instabilities seem to explain line and continuum variability (Abramowicz, Lasota, Xu, 1986), and PG 1211+143, whose "blue bump" has been fitted by accretion disk spectra calculated by Czerny and Elvis (1987).

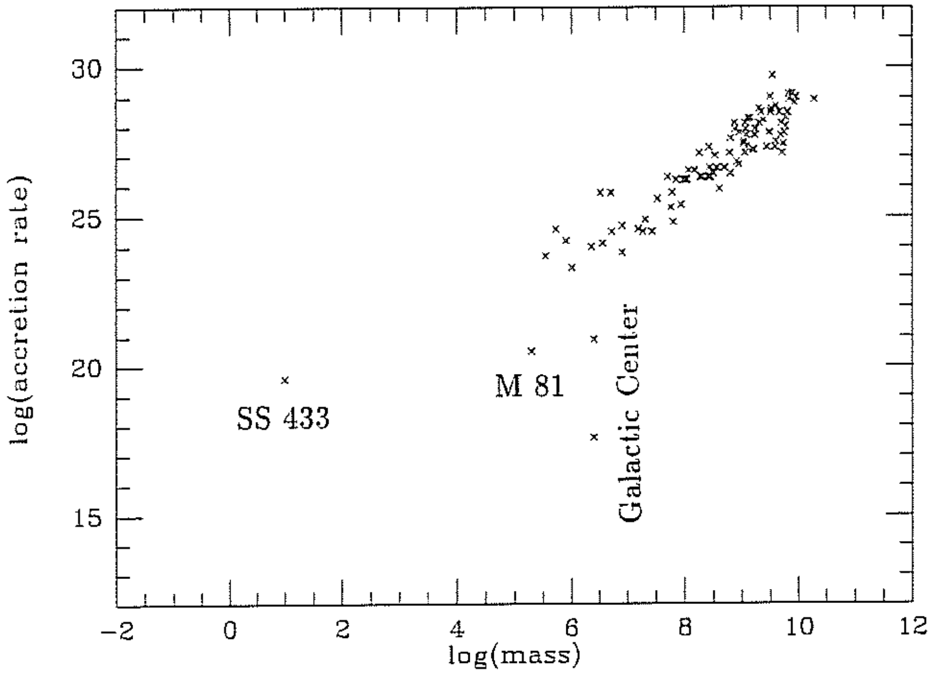

Figure 1: The $\dot{M}(M)$ relation for a sample of active galactic nuclei given by Padovani (1988) and a few other interesting objects.

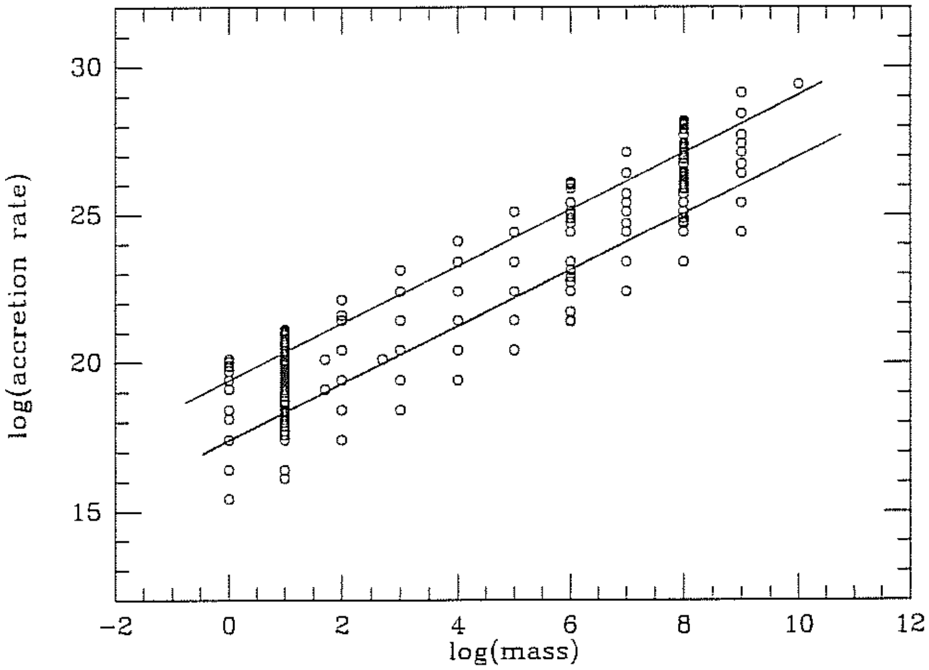

Figure 2: A set of models for slim accretion disks with three input parameters (α, m, $\dot{m}$) projected onto the $\dot{M} - m$ plane. The unstable equilibrium models are located in the region between the two straight lines.

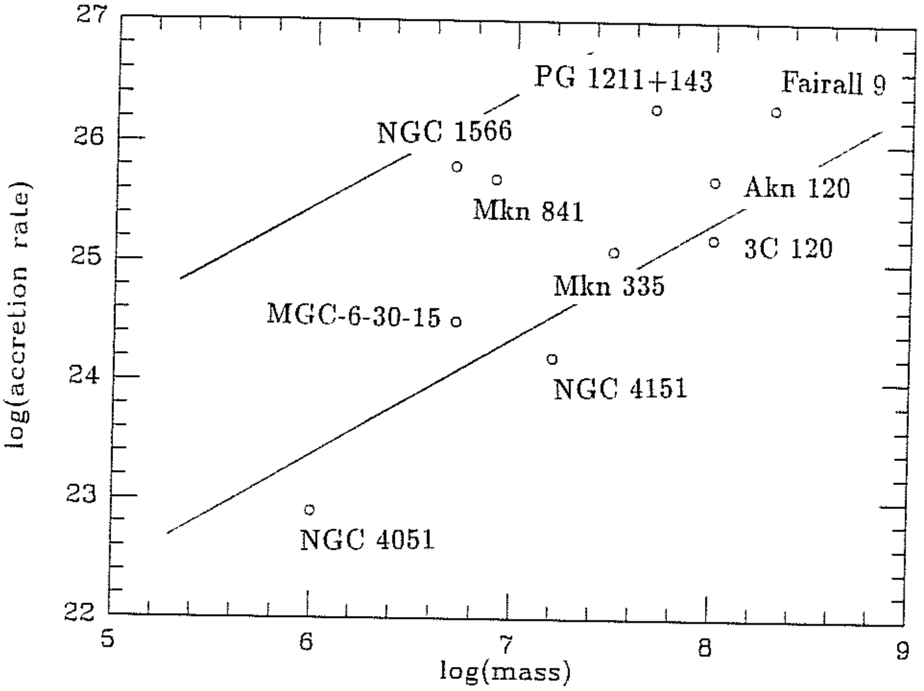

Figure 3: The sources from the TOP TEN list (Chapter 6) plotted in the $\dot{M}(M)$ diagram.

The two straight lines in Figure 2 mark boundaries of the region in which slim accretion disk models become unstable according to the limit cycle mechanism discussed in Chapters 5 and 8 (Abramowicz and Szuszkiewicz, 1988). This sort of instability can give rise to quasi-periodic oscillations with timescales typically of order thousands of days. In order to search for variability with such timescales it is crucial to increase the sample of objects for which long term regular monitoring is available. This has stimulated us (Barbieri, Cappellaro, Romano, Turatto and Szuszkiewicz, 1988) in pursuing a project of making optical observations of quasars at the Asiago Observatory. Other types of instability are discussed in Chapter 8 (Abramowicz, Livio, Soker and Szuszkiewicz, 1988), and Chapter 6 contains an account of recent results for models of slim disks around supermassive black holes.

2. The standard black hole model for active galactic nuclei

Most interpretations of active galactic nuclei (AGN) invoke a massive ($10^6 - 10^9 M_\odot$) and compact (size ≤ 1 pc) gravitational center. The search for the mechanism to power their active phase ($10^{45} - 10^{48}$ erg/s) leads to three well-known categories of models (Rees, 1978 and references therein):

- dense star clusters
- massive stars - spinars or magnetoids
- accretion onto massive black holes

It is very difficult to estimate the energy production efficiencies in these systems. For the first type of model the maximum efficiency is given by the maximum realizable energy of a supernova-like explosion, or by the maximum amount of binding energy that can be released in stellar collisions. For the second mechanism the limit is set by the onset of dynamical instability. The third type seems to be the most powerful and in this case about 10% of rest mass can be converted into electromagnetic radiation.

Systems dependent on gravitational energy, such as all of the mentioned above models, will undergo runaway instability. The almost inevitable endpoint for any dense star cluster or supermassive star will be the collapse of a large fraction of its total mass to a black hole. These two arguments explain why the third possibility has been considered as the standard model.

The standard model for AGN involves a supermassive black hole, located in a galactic center and accreting matter. Accretion occurs because of the action of viscous stresses: gas orbiting the central black hole gradually loses its angular momentum to the gas further out through friction. As the balance of the centrifugal force against gravity shifts in the favor of gravity, the inner gas spirals further inwards. Viscous stresses not only drive accretion by transporting mass inwards and angular momentum outwards, but also convert the liberated gravitational energy of the matter into heat. The heat diffuses towards the surface and is then radiated away.

The most important parameters which determine the observed appearance of the model and the natural timescales connected with it are: the mass of the central black hole M, the accretion rate $\dot{M}$, the dimensionless viscosity parameter α and the orientation angle Θ of the rotation axis with respect to the line of sight. It is convenient to introduce a dimensionless mass parameter $m_8 = M/10^8 M_\odot$ and a dimensionless accretion rate $\dot{m}_e = \dot{M}/\dot{M}_E$. Here $10^8 M_\odot$ was taken as a "typical" mass for the central black hole and $\dot{M}_E = 1.4 \times 10^{17}(M/M_\odot)$ $[g\ sec^{-1}]$ is the Eddington accretion rate, which is connected with the Eddington luminosity L_E by $L_E = \dot{M}_E c^2$.

The shortest timescale connected with the standard model is the *causal* timescale t_c which is the light crossing time for the gravitational radius of the black hole ($r_G = 2GM/c^2$) and is given by $t_c = r_G/c \approx 10^{-2} m_8$ (in days). Models in different regions of the parameter space ($\dot{m}_e$, α) are referred to as thin, thick and slim accretion disks. (Other models of accretion flows are reviewed e.g. by Treves, Maraschi and Abramowicz 1988.)

2.1 Thin accretion disks

The nature of the equilibrium and stability of these disks, which are characterized by $\dot{m}_e \ll 1$, and $0 < \alpha \leq 1$ is rather well understood in terms of the Shakura-Sunyaev model (reviewed by Pringle 1981). The vertical height of the disk, $h(r)$, is much smaller than the corresponding cylindrical radius r. This allows a one-dimensional treatment with all of the hydrodynamic equations being integrated in the vertical direction. The thin disks have very sub-Eddington luminosities, $L \ll L_E$. They rotate with angular velocity Ω equal, at each radius, to the Keplerian value, $\Omega_K \approx (GM/r^3)^{1/2}$. The corresponding orbital period defines the dynamical timescale, $t_d = 2\pi/\Omega_K$. The orbital period is equal to the crossing time of a sound wave in the vertical direction, $t_d = h/v_s$. Here v_s is the sound speed. It is assumed that the dominant component of the viscous stress tensor is proportional to the total pressure, $\tau_{\varphi r} = \nu(dln\Omega/dlnr) = -\alpha P$, which implies (for Keplerian rotation) that the kinematic viscosity coefficient is given by $\nu = \alpha v_s h$.

Most of the luminosity comes from the innermost part of the disk, close to the radius $r \approx 5r_G$. For this particular radius, and for disks which are radiation pressure supported and have opacity dominated by electron scattering, the dynamical timescale, t_d, thermal timescale, $t_t = t_d\alpha^{-1}$, and viscous timescale $t_v = t_t(h/r)^{-2}$ are respectively (in days):

$$t_d \approx 2m_8 \qquad t_t \approx 2m_8\alpha^{-1} \qquad t_v \approx 5\alpha^{-1}\dot{m}_e^{-2}m_8 \tag{1}$$

2.2 Thick accretion disks

When cooling processes in the accretion flow are not efficient enough, the vertical thickness of the flow cannot be small. There are two different physical situations in which this happens: for radiation pressure supported thick accretion disks (e.g. Abramowicz, Calvani and Nobili 1980) which are characterized by $\dot{m}_e \gg 1$, and $\alpha \ll 1$, and for ion pressure supported thick disks (Rees et al. 1982) which have $\dot{m}_e < 50\alpha^2$. Thick disks of both types have shapes resembling a sphere with two empty funnels along the rotation axis. Most of the radiation is produced close to $r \approx 5r_G$ and emerges through the funnels. However, while the radiation pressure supported disks have super-Eddington luminosities, the ion supported ones are always sub-Eddington. In both types of thick disks rotation is non-Keplerian.

Unlike the Shakura-Sunyaev model or its general relativistic version calculated by Novikov and Thorne (1973), the thick disks correctly describe relativistic effects which dominate the accretion flow close to the black hole. These effects are due to the transonic nature of the flow and to some peculiarities in the topology of the equipotential surfaces. One of the equipotentials crosses itself and is reminiscent of the Roche lobe in close binaries (Figure 1a). The crossing is not connected with the self-gravity of the disk (which is assumed to be negligible) but with the general relativistic nature of the gravitational field which is competing with the rotation of the disk (Abramowicz, Jaroszyński, and Sikora 1978). The crossing occurs at the *cusp* ($r = r_{in}$) where the matter rotates with exactly the Keplerian angular velocity. A nonzero thickness of the disk at the cusp implies Roche-lobe overflow and, as in close binaries, *dynamical mass loss.* The mass loss rate and the induced advective heat loss rate depend on the surface density and vertical thickness at the cusp (Abramowicz 1981): $\dot{M} = const \times \Sigma H$, $L = const \times \Sigma H^3$. The efficiency of the accretion $\eta = L/\dot{M}c^2$ is equal to minus the binding energy of the Keplerian orbit located at the cusp. It ranges (for non-rotating black holes) from a maximum value of about 0.1 for small accretion rates (when the cusp is located at the *marginally stable orbit*, $r_{in} = 3r_G$) to *zero* for high accretion rates (when the cusp is located at the *marginally bound orbit*, $r_{in} = 2r_G$). Because of the decrease in efficiency for high accretion rates, the luminosity is not

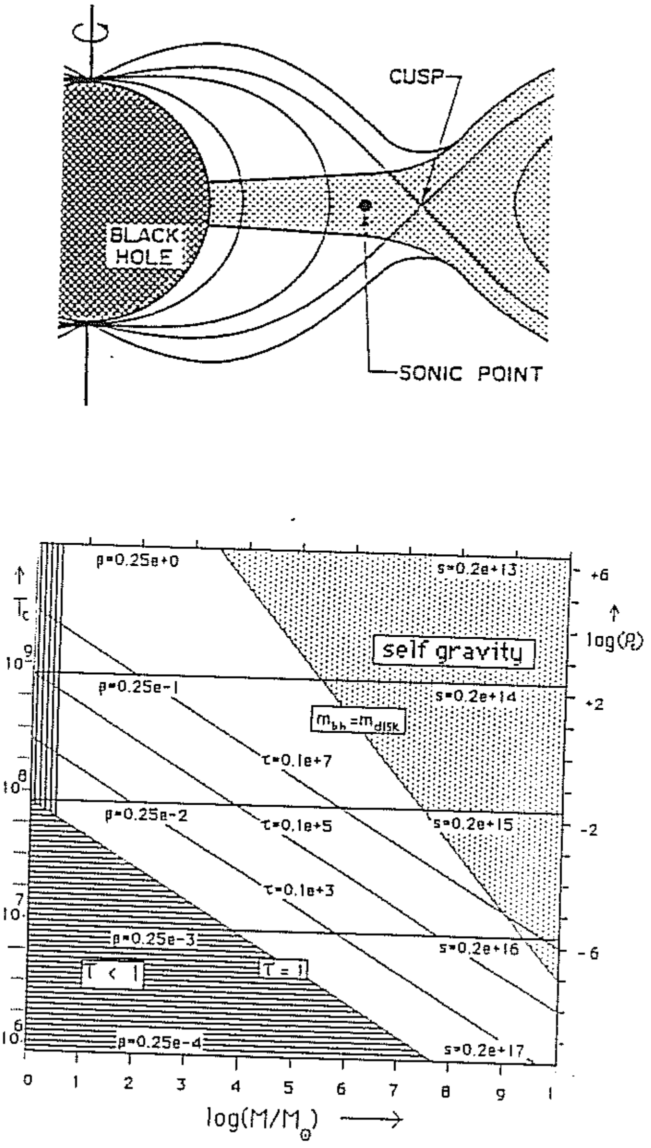

Figure 1: (a) The innermost part of an accretion disk. (b) Thermodynamic conditions of the center of a thick disk.

then proportional to the accretion rate, but rather $L \propto \log \dot{M}$. The cusp is located in the transonic part of the flow. Thermodynamic conditions at the pressure maximum of a thick disk in the Schwarzschild geometry ($r_{in} = 2.97 r_G$) are shown in Figure 1b, taken from Chakrabarti (1986).

Gas blown from the walls of the funnel may be accelerated by the radiation pressure gradient (Abramowicz and Piran 1980) or by electromagnetic forces (Rees et al. 1982) up to highly relativistic velocities, forming well collimated jets with Lorentz factors $\gamma \geq 10$. Variability with an intrinsic timescale t_{in} occurring in the jet (moving toward us at a small angle Θ) will be observed with a timescale shortened by a factor $\delta = \gamma/[1 - (vcos\Theta/c)]$. Here v is the velocity of the jet.

2.3 Slim accretion disks

Slim disks are characterized by $\dot{m}_e \approx 1$, and $\alpha \ll 1$. They have been introduced in a recent paper by Abramowicz, Czerny, Lasota and Szuszkiewicz (1988). The slim disk combines the good features of both thin and thick disk models while avoiding many of their problems. In particular, by adopting the vertical integration used for the thin disks, the slim disk models inherit the advantage of a one dimensional treatment. However, as in the thick disk models, they also include the effects of the horizontal pressure gradient and horizontal heat flux, the dynamical importance of the accretion velocity and deviations away from strictly Keplerian rotation. These effects (neglected in the thin disk models) are closely connected with the Roche lobe overflow mechanism, and therefore are dominant in the transonic part of the accretion flows.

Accretion onto black holes is always transonic and so stationary solutions have *critical points* at which some additional regularity conditions must be satisfied. These conditions cannot be satisfied for all of the choices of the boundary conditions (accretion rate, energy, angular momentum far away) and parameters (equation of state, opacity, viscosity) which describe the astrophysical situation. This creates *forbidden regions* in the parameter space of the problem and implies that not all of the astrophysically acceptable boundary conditions can lead to regular stationary flows.

2.4 Unified scheme for active galactic nuclei

The different types of accretion disk discussed in the previous sections may explain several observed properties of AGN. A few "unified schemes" for such an explanation have been proposed (see e.g. Begelman, Blandford and Rees 1984). The most recent review on this subject is that by Abramowicz, Calvani and Madau (1988). The optically quiet radio galaxies (e.g. M 87 or Cygnus A) may be associated with subcritical ion tori whose total emitted luminosity is channelled into kinetic energy of the jets. In this case much of the energy powering the source might be extracted electromagnetically from the spin of the hole (Phinney 1983). Bright quasars and Seyfert galaxies may be powered by nearly critically or supercritically ($L \approx L_E$) accreting black holes. Such a scheme would associate an increasing ratio of nonthermal to thermal emission with decreasing $\dot{m}_e$. The two parameters m_8, $\dot{m}_e$ are in some sense intrinsic for the source. What we observe depends also on how the source is situated in observer frame. The statistics (Cavaliere et al., 1986) and source appearance is affected by the orientation angle Θ of the rotation axis with respect to the line of sight. The main mechanisms for anisotropy are Doppler beaming, along the direction of motion of the radiation emitted by material in a relativistic jet (Blandford and Rees, 1978) and the strongly anisotropic radiation field emitted from thick supercritical accretion disks (Sikora, 1981). The shape of the disk may be relevant for understanding the polarization properties of Seyfert galaxies (Antonucci, 1983) with higher polarization being expected from thin disks. The different modes of accretion would then produce different kinds of emission spectra. Thermal emission from thin disks and radiation tori produces a peak in the optical/UV continuum of quasars and Seyfert galaxies can be decomposed into a single power low $F_\nu \propto \nu^{-\alpha}$ with $\alpha \simeq 1$ plus a superimposed optical/UV bump. Properties of thermal components are crucial for constraining M and $\dot{M}$. The observational classification of active galaxies has been reviewed by Lawrence (1987) who stressed ideas which can lead to a unified phenomenology for these objects with the hope that "there is only one kind of AGN". The observed variety then arises from four degrees of freedom:

- dust opacity
- viewing angle of the relativistic jet
- duty cycle of activity
- the overall luminosity

A final unified scheme should combine the both observational and theoretical schemes.

3. Thin accretion disks

The theory of thin accretion disks was developed in classical papers by Pringle and Rees (1972), Shakura and Sunyaev (1973), Novikov and Thorne (1973) and Lynden-Bell and Pringle (1974). We will consider here the thin disk models, discussing their most interesting properties, treating them as the small accretion rate limit of slim disks.

3.1 Equations

In all classical papers concerning accretion disks around black holes, the inner disk boundary coincides with the marginally stable orbit of a test particle. For a Schwarzschild black hole this orbit has a radius of $3r_G$, where $r_G = 2GM/c^2$ is the gravitational radius. For $r > r_G$ the disk rotation is Keplerian, for $r < r_G$ the matter is freely falling into the black hole. It is natural to adopt a no torque boundary condition at the inner disk radius, $r_{in} = r_{MS} = 3r_G$.

Stoeger (1976) pointed out that classical models give infinite gas density at r_{in}. To avoid the singularity Stoeger (1980) and Kato et al. (1981) considered gravitational and viscous effects but neglected hydrodynamical ones. This type of approach leads to unphysical effects, such as a disk with monotonic pressure. The proper treatment of the inner boundary condition in the disk models was initiated by Paczyński and Bisnovatyi-Kogan (1981), Muchotrzeb and Paczyński (1982) and will be discussed later in the Chapter devoted to slim disks and critical points. Figure 1 shows the schematic structure of the thin disk. The pressure gradient and radial velocity gradient in the equation of motion is neglected. The advective term in the energy balance equation is assumed to be not important. The angular momentum in the pseudo-Newtonian potential (Paczyński and Wiita, 1980),

$$\Phi = -\frac{GM}{r - r_G} \tag{1}$$

is given by:

$$l_K = (GMr)^{1/2}\frac{r}{r - r_G} \tag{2}$$

These assumptions give us the following set of equations:

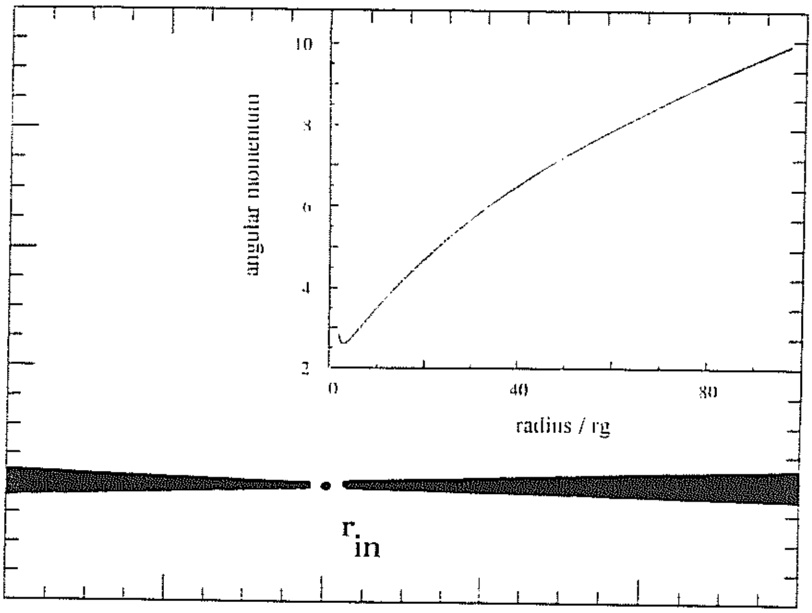

Figure 1: Schematic structure of a thin disk with its angular momentum distribution.

angular momentum conservation with the standard α viscosity prescription

$$\dot{M}(l_K - l_{Kin}) = 4\pi r^2 z \alpha P \tag{3}$$

energy balance equation with Q^+, the heat input due to viscous processes , equal to Q^-, the heat loss due to radiation leaving the disk surface.

$$Q^+ = \dot{M}(l_K - l_{Kin})(-\frac{d\Omega_K}{dr}) = 4\pi r F^- = Q^- \tag{4}$$

Hydrostatic equilibrium in the vertical direction:

$$\Omega_K^2 z^2 = B_4 \frac{P}{\rho} \tag{5}$$

Here:

$$\dot{M} = B_5 4\pi r \rho z v_r > 0 \tag{6}$$

is the accretion rate,

$$F^- = B_3 \frac{c}{\kappa\rho} \frac{aT^4}{3z} \tag{7}$$

is the radiative flux in the vertical direction,

$$\kappa = \kappa_e \tag{8}$$

is the opacity coefficient, which at the moment is only due to electron scattering. P, ρ, and T are usual thermodynamic quantities, z is the half-thickness of the flow. l_{Kin} is the angular momentum at the inner edge of the disk and B_i are coefficients depending on details of vertical structure with the following values: $B_3 = 6$, $B_4 = 6$, $B_5 = 0.5$. These coefficients puzzle many people and touch a very important problem (see Chapter 5B).

For convenience we will rewrite these equations using the following dimensionless quantities:

$$r = \frac{r}{r_G}$$

$$m = \frac{M}{M_\odot}$$

$$\dot{m} = \frac{\dot{M}}{\dot{M}_C}$$

where

$$\dot{M}_C = \frac{64\pi GM}{c\kappa_e}.$$

We will also introduce the dimensionless angular momentum:

$$\frac{l'_K}{(GMr_G)^{1/2}} = l_K = \frac{r^{3/2}}{r-1}$$

and the dimensionless angular velocity:

$$\frac{\Omega'_K}{(GM/r_G^3)^{1/2}} = \Omega_K = \frac{r^{-1/2}}{r-1}$$

We will use also the logarithmic derivative of the angular velocity, which is

$$-\frac{dln\Omega_K}{dr} = \frac{3r-1}{2r(r-1)}$$

Let us denote

$$-\frac{dln\Omega_K}{dr} = \mathcal{D}$$

and

$$(l_K - l_{Kin}) = \mathcal{F}.$$

Now the equations have the following form:

$$P^{3/2}\rho^{-1/2} = \frac{2c^5}{GM_\odot} B_4^{-1/2}\kappa^{-1}r^{-2}\mathcal{F}\Omega_K m^{-1}\dot{m}\alpha^{-1} \tag{9}$$

$$P^{-1/2}\rho^{-1/2}T^4 = 4\sqrt{2}cB_3^{-1}B_4^{1/2}(\frac{a}{3})^{-1}r^{-1}\mathcal{D}\mathcal{F}\dot{m} \tag{10}$$

$$zP^{-1/2}\rho^{1/2} = 2\sqrt{2}c^{-3}GM_\odot B_4^{1/2}\Omega_K^{-1}m \tag{11}$$

3.2 The standard solutions of the thin disk structure

The equations describing the structure of the disk can be solved analytically in two particular cases. This occurs when either the gas pressure or the radiation pressure dominates the total pressure. Every structural quantity can be expressed in terms of other structural quantities: for example, the three control parameters (m, $\dot{m}$, α), and the radial distance from the central source, r. This is what was done by Shakura and Sunyaev (1973) using the Newtonian gravitational potential, by Novikov and Thorn

(1973) for a Kerr black hole and by Abramowicz (1987) using the pseudo-Newtonian potential. We are repeating here the same formulas for the pseudo-Newtonian potential in a slightly different form. We would like to discuss them in more detail, considering also different opacity prescriptions. For those who are curious about how we derived the constant coefficients, the explicit formulas, including only physical constants and B_i coefficients, are given.

The fluid is described in the general case by the following equation of state;

$$P = \frac{k}{\mu H}\rho T + \frac{a}{3}T^4 \tag{12}$$

The standard solutions for the disk structure in two limiting cases:
(I)

$$P_{gas} \gg P_{rad}$$

and (II)

$$P_{gas} \ll P_{rad}$$

are listed below. We discuss the properties of these two models comparing the physical quantities one by one.

(I) Equatorial temperature [K]:

$$T = T_0 \kappa^{-1/5} f_T(r) m^{-1/5} \dot{m}^{2/5} \alpha^{-1/5} \tag{13}$$

$$T_0 = \left(\frac{8\sqrt{2}c^6}{B_3 G M_\odot}\right)^{1/5} \left(\frac{a}{3}\right)^{-1/5} \left(\frac{k}{\mu H}\right)^{-1/5} = 4.98 \times 10^8 \tag{14}$$

$$f_T(r) = r^{-3/5} \mathcal{F}^{2/5} \mathcal{D}^{1/5} \Omega_K^{1/5} \tag{15}$$

The behaviour of the function $f_T(r)$ is shown in Figure 2. The temperature at the inner disk radius is equal to zero. The maximum occurs at about $6r_G$.

(II) Equatorial temperature [K]:

$$T = T_0 \kappa^{-1/4} f_T(r) m^{-1/4} \alpha^{-1/4} \tag{16}$$

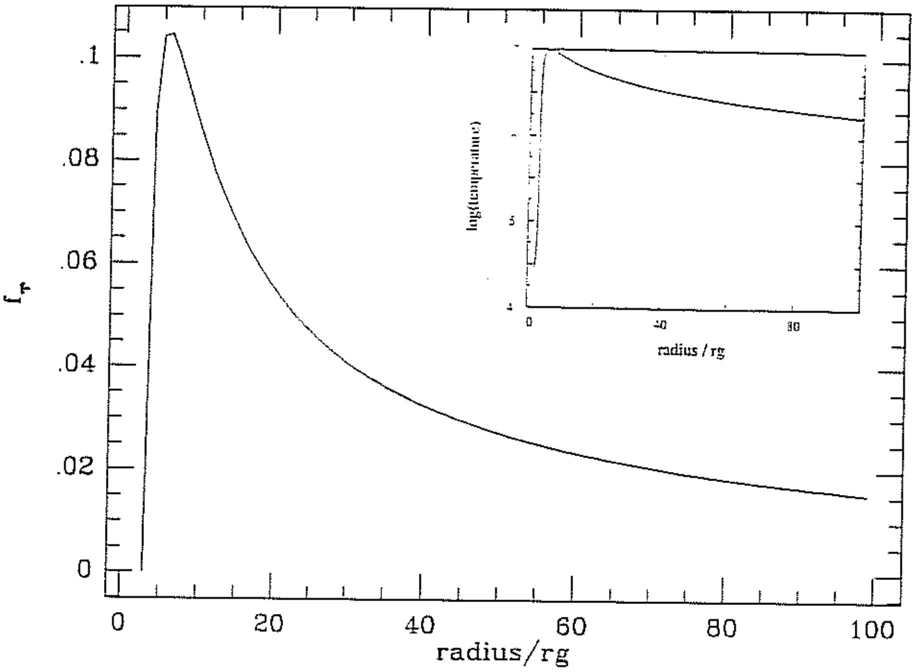

Figure 2: The distribution of temperature in a thin disk if the pressure is dominated by gas. For comparison, the temperature distribution of a slim disk with low accretion rate is given.

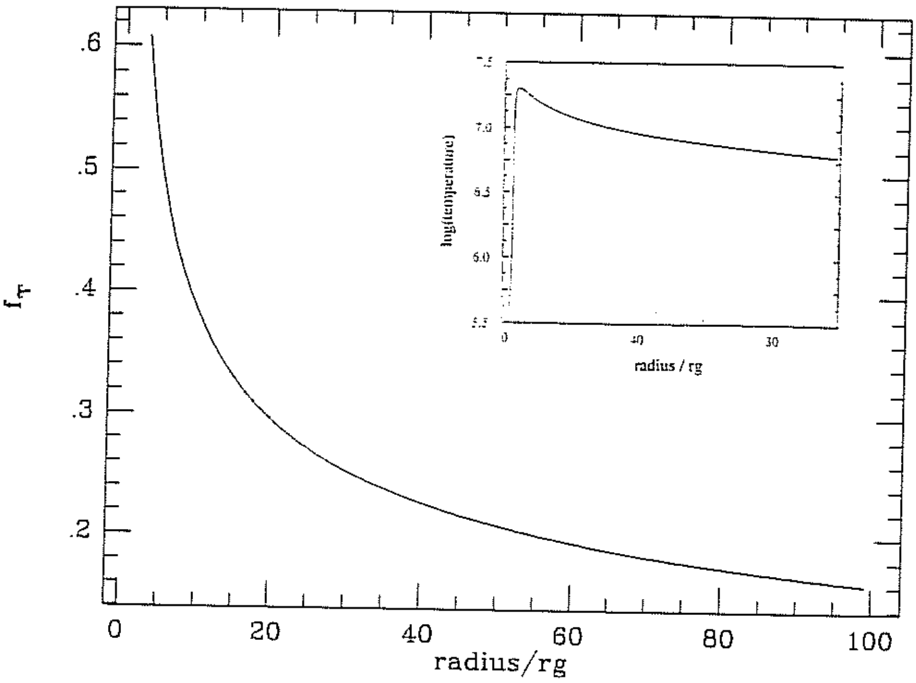

Figure 3: The temperature distribution for thin and slim disks if the pressure is dominated by radiation

$$T_0 = (\frac{c^4 B_3 B_4^{-1}}{G M_\odot 2\sqrt{2}})^{1/4} (\frac{a}{3})^{-1/4} = 3.04 \times 10^7 \tag{17}$$

$$f_T(r) = r^{-1/4} \mathcal{D}^{-1/4} \Omega_K^{1/4} \tag{18}$$

The temperature in the thin disk has no maximum. There is not enough cooling to balance viscous heating, giving rise to a thermal instability in the inner region

(I) Density [g/cm^3]:

$$\rho = \rho_0 \kappa^{-7/10} f_\rho(r) m^{-7/10} \dot{m}^{2/5} \alpha^{-7/10} \tag{19}$$

$$\rho_0 = \frac{2c^5}{G M_\odot B_4^{1/2}} (\frac{k}{\mu H})^{-6/5} (\frac{8\sqrt{2} c^6}{B_3 G M_\odot})^{-3/10} (\frac{a}{3})^{3/10} = 8.653 \tag{20}$$

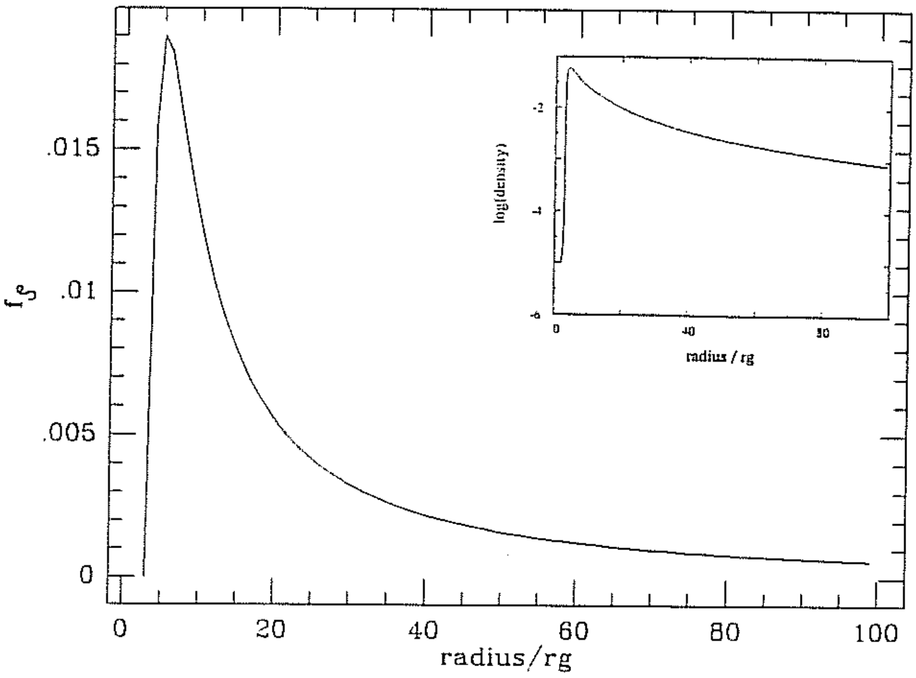

Figure 4: The density distribution in thin and slim disks (I)

$$f_\rho(r) = r^{-11/10}\mathcal{F}^{2/5}\mathcal{D}^{-3/10}\Omega_K^{7/10} \tag{21}$$

This function is shown in Figure 4. The density distribution is similar to the temperature distribution.

(I) Density [g/cm^3]:

$$\rho = \rho_0 \kappa^{-1} f_\rho(r) m^{-1} \dot{m}^{-2} \alpha^{-1} \tag{22}$$

$$\rho_0 = \frac{c^2 B_4^{-2} B_3^3}{G M_\odot 64\sqrt{2}} = 4.49 \times 10^{-7} \tag{23}$$

$$f_\rho(r) = r\mathcal{F}^{-2}\mathcal{D}^{-3}\Omega_K \tag{24}$$

In the case of thin disk the density diverges at the inner edge (Figure 5).

(I) Total pressure [dyn/cm^2]:

$$P = P_0 \kappa^{-9/10} f_P(r) m^{-9/10} \dot{m}^{4/5} \alpha^{-9/10} \tag{25}$$

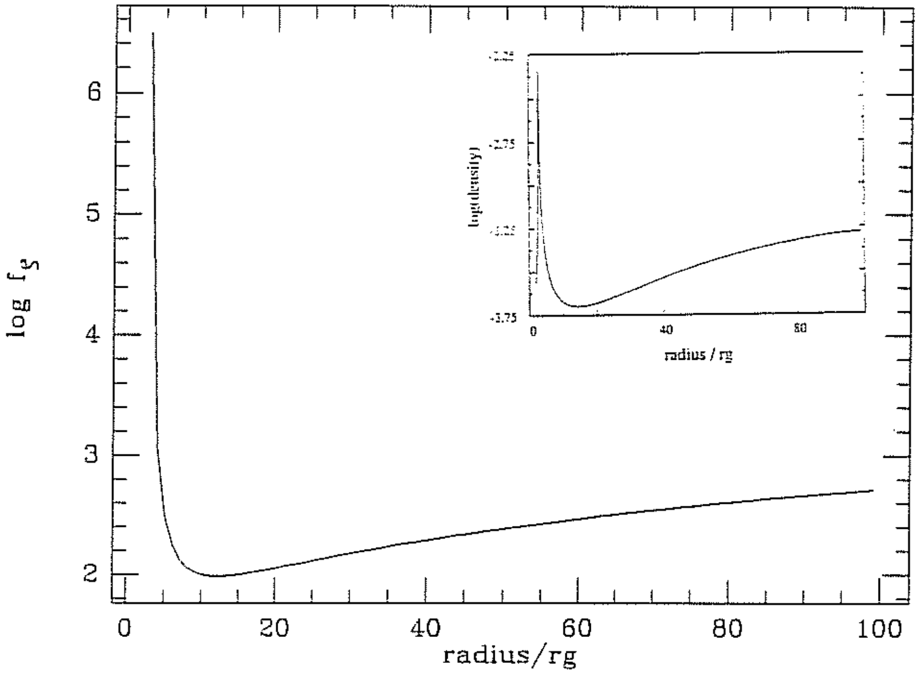

Figure 5: The density distribution for both models (II)

$$P_0 = \frac{2c^5}{GM_\odot B_4^{1/2}}(\frac{k}{\mu H})^{-2/5}(\frac{8\sqrt{2}c^6}{B_3 GM_\odot})^{-1/10}(\frac{a}{3})^{1/10} = 5.77 \times 10^{17} \qquad (26)$$

$$f_P(r) = r^{-17/10}\mathcal{F}^{4/5}\mathcal{D}^{-1/10}\Omega_K^{9/10} \qquad (27)$$

The pressure distribution in the disk is showed in Figure 6.

(II) Total pressure [dyn/cm^2]:

$$P = P_0 \kappa^{-1} f_P(r) m^{-1} \alpha^{-1} \qquad (28)$$

$$P_0 = \frac{c^4 B_3}{GM_\odot B_4 2\sqrt{2}} = 2.15 \times 10^15 \qquad (29)$$

$$f_P(r) = r^{-1}\mathcal{D}^{-1}\Omega_K \qquad (30)$$

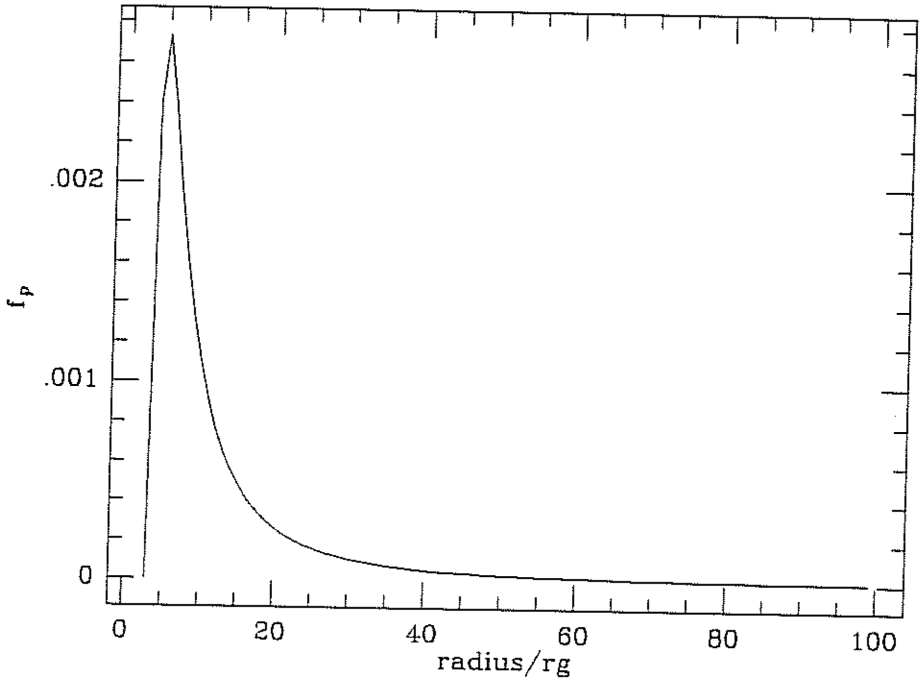

Figure 6: The pressure in thin disk (I)

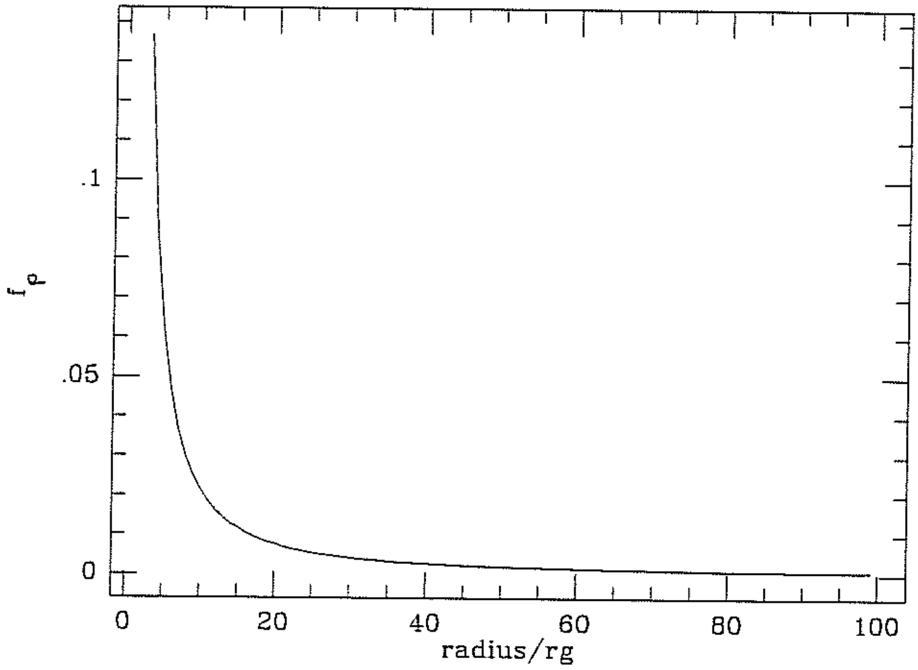

Figure 7: The pressure as a function of radius for a thin disk (II)

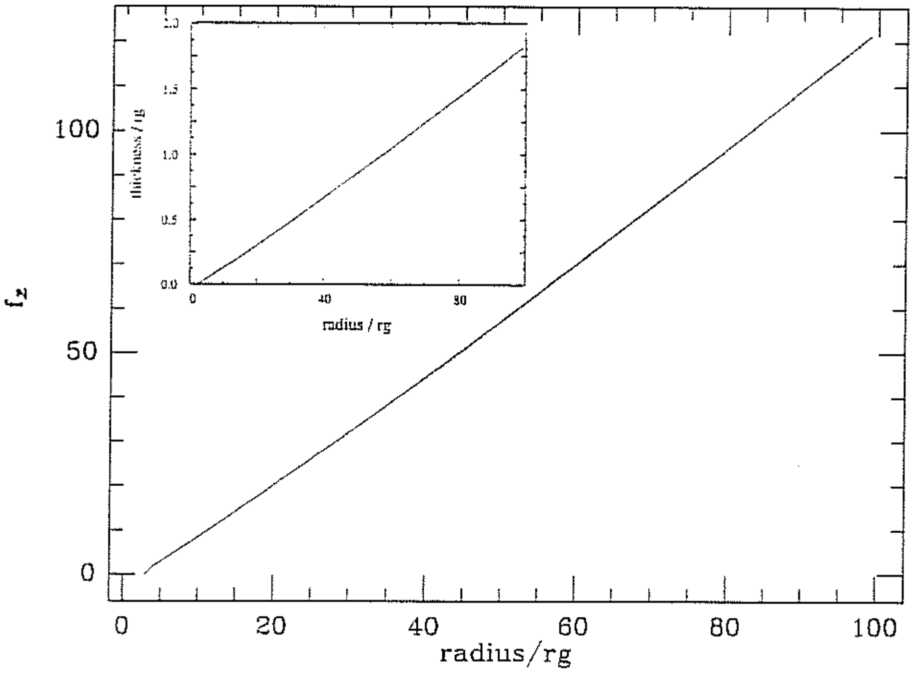

Figure 8: The thin and slim disk thickness (I)

The behaviour of the pressure is shown in Figure 7.

(I) Half-thickness of the disk [cm]:

$$z = z_0 \kappa^{-1/10} f_z(r) m^{9/10} \dot{m}^{1/5} \alpha^{-1/10} \tag{31}$$

$$z_0 = \sqrt{2} B_4^{1/2} \frac{2GM_\odot}{c^3} (\frac{8\sqrt{2}c^6}{GM_\odot})^{1/10} (\frac{k}{\mu H})^{2/5} (\frac{a}{3})^{-1/10} = 8.81 \times 10^3 \tag{32}$$

$$f_z(r) = r^{-3/10} \mathcal{F}^{1/5} \mathcal{D}^{1/10} \Omega_K^{-9/10} \tag{33}$$

The radial function $f_z(r)$ is monotonic (Figure 8).

(II) Half-thickness of the disk [cm]:

$$z = z_0 f_z(r) m \dot{m} \tag{34}$$

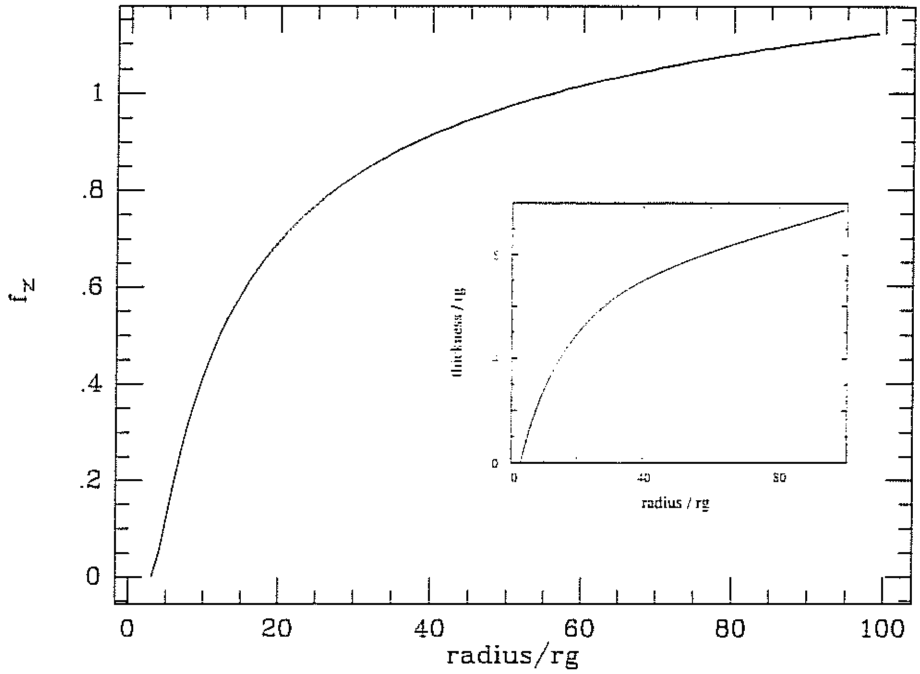

Figure 9: The thickness of the disks (II)

$$z_0 = \frac{16B_4B_3^{-1}GM_\odot}{c^2} = 2.36 \times 10^6 \tag{35}$$

$$f_z(r) = r^{-1}\mathcal{F}\mathcal{D}\Omega_K^{-1} \tag{36}$$

The thickness of the thin disk is very similar to the classical thick disk shape (Figure 9).

(I) Surface density [g/cm^2]:

$$\Sigma = \Sigma_0\kappa^{-4/5}f_\Sigma(r)\dot{m}^{3/5}\alpha^{-4/5}m^{1/5} \tag{37}$$

$$\Sigma_0 = 8\sqrt{2}c^2(\frac{8\sqrt{2}c^6}{B_3GM_\odot})^{-1/5}(\frac{k}{\mu H})^{-4/5}(\frac{a}{3})^{1/5} = 1.525 \times 10^5 \tag{38}$$

$$f_\Sigma(r) = r^{-7/5}\mathcal{F}^{3/5}\mathcal{D}^{-1/5}\Omega_K^{-1/5} \tag{39}$$

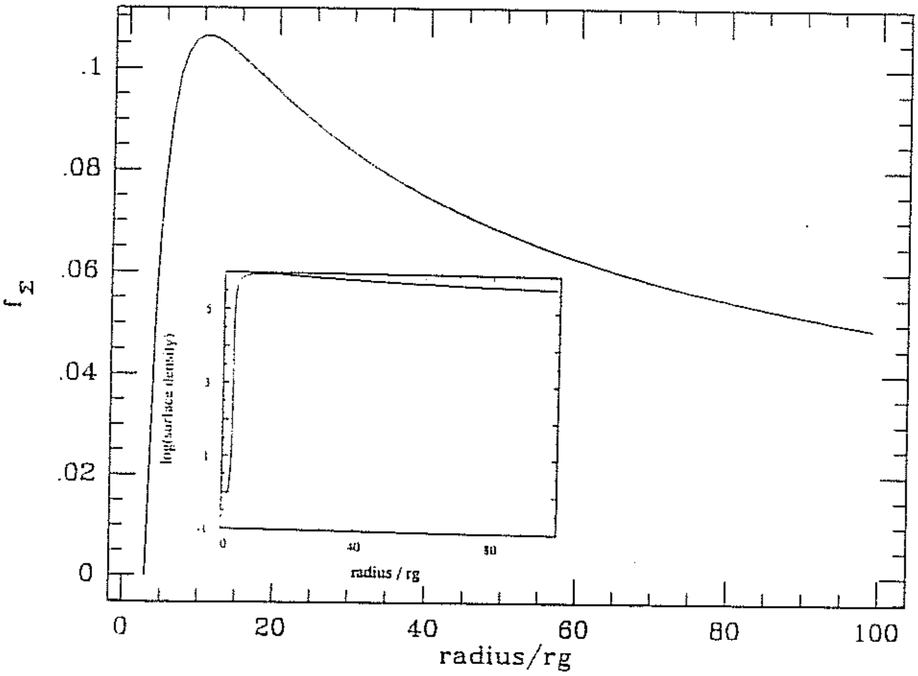

Figure 10: The surface density of the thin and slim disks (I)

The radial distribution of surface density is shown in Figure 10.

(II) Surface density [g/cm^2]:

$$\Sigma = \Sigma_0 \kappa^{-1} f_\Sigma(r) \dot{m}^{-1} \alpha^{-1} \tag{40}$$

$$\Sigma_0 = \frac{B_4^{-1} B_3^2}{2\sqrt{2}} = 2.12 \tag{41}$$

$$f_\Sigma(r) = \mathcal{F}^{-1} \mathcal{D}^{-2} \tag{42}$$

Figure 11 illustrates the radial distribution of the surface density.

(I) Dimensionless radial velocity

$$\frac{v}{c} = v_0 \kappa^{-1/5} f_v(r) m^{-1/5} \dot{m}^{2/5} \alpha^{4/5} \tag{43}$$

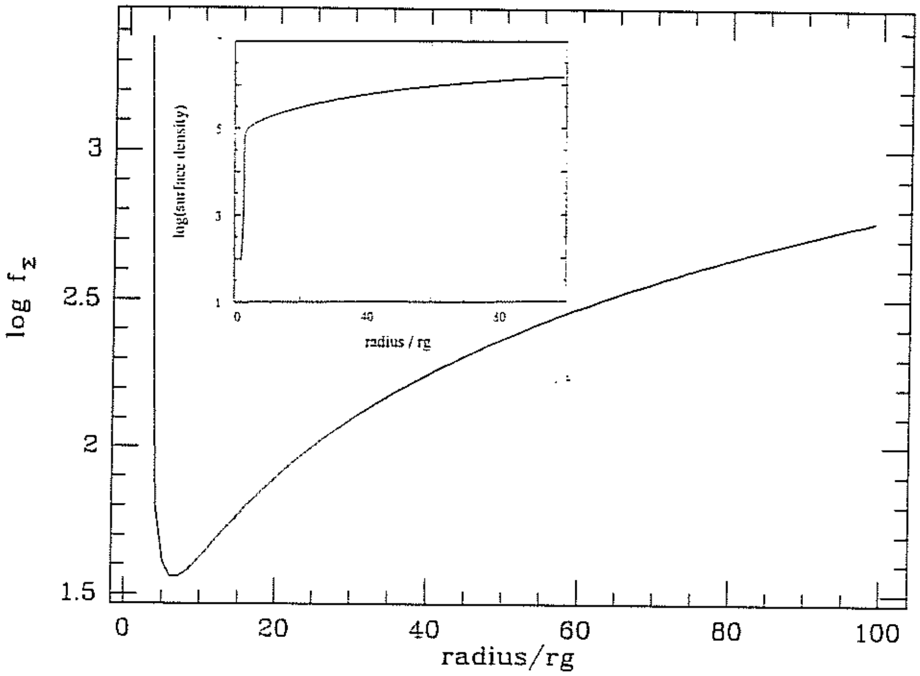

Figure 11: The surface density for both models (II)

$$v_0 = \sqrt{2}B_5^{-1}c^{-2}(\frac{k}{\mu H})^{4/5}(\frac{a}{3})^{-1/5}(\frac{8\sqrt{2}c^6}{B_3 G M_\odot})^{1/5} = 2.10 \times 10^{-4} \tag{44}$$

$$f_v(r) = r^{2/5}\mathcal{F}^{-3/5}\mathcal{D}^{1/5}\Omega_K^{1/5} \tag{45}$$

The radial drift velocity is divergent at $r_{in} = 3r_G$ (Figure 12).

(II) Dimensionless radial velocity

$$\frac{v}{c} = v_0 f_v(r)\dot{m}^2\alpha \tag{46}$$

$$v_0 = \frac{4B_4}{\sqrt{2}B_3^2 B_5} = 0.94 \tag{47}$$

$$f_v(r) = r^{-1}\mathcal{F}\mathcal{D}^2 \tag{48}$$

In this case the velocity does not diverge (Figure 13).

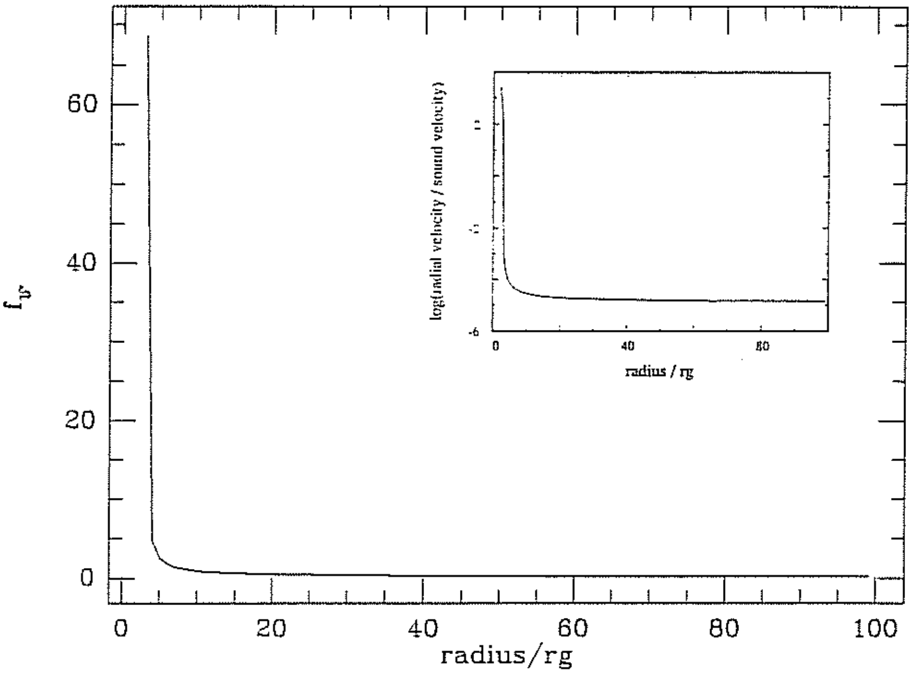

Figure 12: The distribution of radial velocity in the thin and slim disks (I)

(I) and (II) radiative flux [erg/s cm]

$$F^- = F_0^- \kappa^{-1} f_{flux}(r) m^{-1} \dot{m} \tag{49}$$

$$F_0^- = \frac{2c^5}{GM_\odot} = 3.64 \times 10^{26} \tag{50}$$

$$f_{flux}(r) = r^{-1} \mathcal{F} \mathcal{D} \Omega_K \tag{51}$$

The flux reaches the maximum at about $5r_G$ (Figure 14).

The flux in both cases (gas dominance and radiation pressure dominance) is the same because of the assumption about optical thickness of the flow. The radiative flux for the thin and slim disk models is shown in Figure 15.

3.3 Sequence of equilibrium models

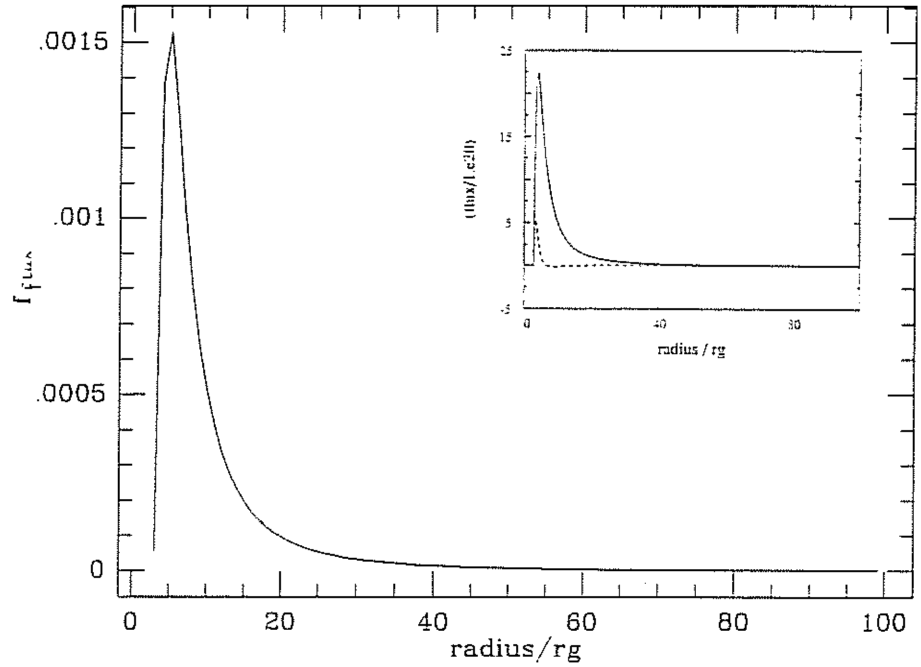

Figure 15: The flux for the thin and slim disk from the surface (II). The dashed line represents the advective flux.

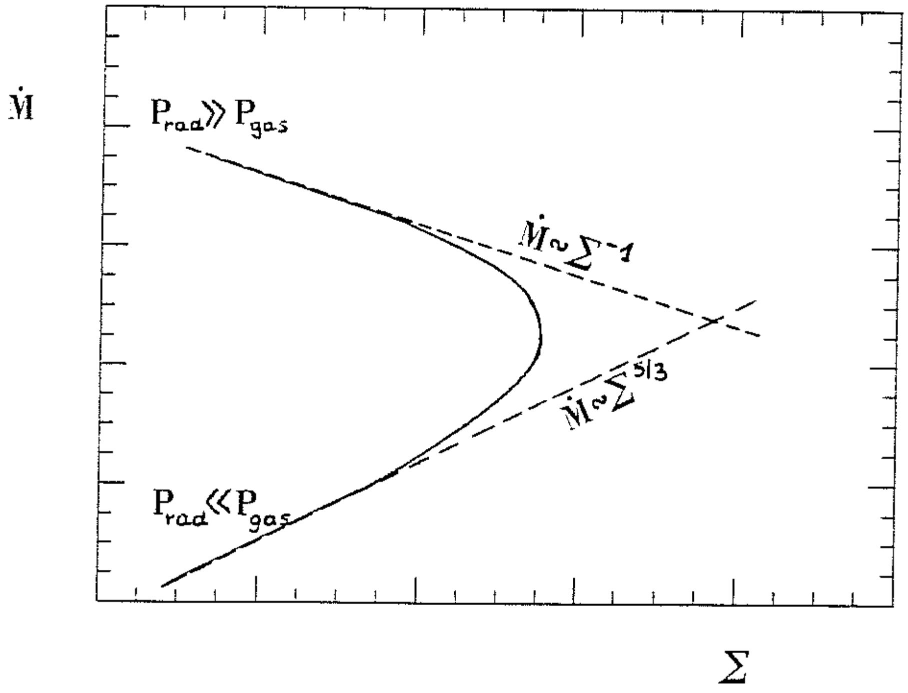

Figure 16: Lower and middle branches with the asymptotic solutions

We can study the sequence of equilibrium models at a fixed radius, r, but with different values of the control parameters. It is natural to choose the region where the most energy is released, that is $r \approx 5r_G$. How do physical conditions at this radius depend on m, $\dot{m}$ and α? We represent the models in the $log(\dot{m}) - log(\Sigma)$ plane (Figure 16). Two dashed lines correspond to the already discussed standard solutions. For the lower branch ($P_{rad} \ll P_{gas}$) accretion rate is proportional to the surface density to power $\frac{5}{3}$, for the middle ($P_{gas} \ll P_{rad}$) the slope of this relationship is equal to -1. Therefore, the curve $\Sigma = \Sigma(\dot{M})$ has somewhere for $P_{gas} \approx P_{rad}$ a turning point. We can find easily the turning point from equations (9)-(11), requiring that $log(\Sigma)/log(\dot{m}) = 0$. The result is

$$\frac{dln\Sigma}{dln\dot{M}} = \frac{5(\beta - 2/5)}{3\beta + 2}.$$

At this point $P_{gas} = 3/2P_{rad}$. The dependence of accretion rate at this point on other parameters as m and α is described by the following exact

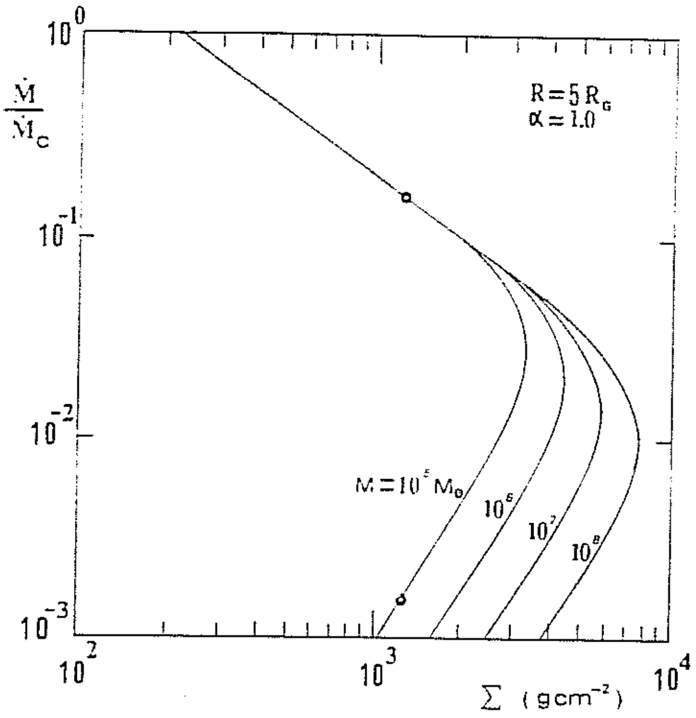

Figure 17: Lower and middle branches for the different mass of the central object.

formula:

$$\dot m = \dot m_0 \kappa^{-1/8} r^{11/8} \mathcal{F}^{-1} \mathcal{D}^{-9/8} \Omega_K^{1/8} m^{-1/8} \alpha^{-1/8} \tag{52}$$

Coefficient $\dot m_0$ is equal to

$$\dot m_0 = c^{-1/2} \frac{B_4^{-5/8} B_3^{9/8}}{(GM_\odot)^{1/8}} \sqrt{2}^{-10/8} 8^{-9/8} (\frac{a}{3})^{-1} (\frac{k}{\mu H})^{9/16} \tag{53}$$

How the $\Sigma - \dot m$ relation depends on the mass of the black hole and on viscosity parameter is shown in Figure 17 and 18.

a) More realistic opacity coefficient

Electron scattering is not the only one mechanism for opacity in the disk. We can ignore line opacity and bound-free opacity, but we must include the free-free absorption which plays significant role in the cooler part of the disk. The opacity coefficient can be expressed by Kramers rule:

$$\kappa = \kappa_e + \kappa_0 \rho T^{-7/2} \tag{54}$$

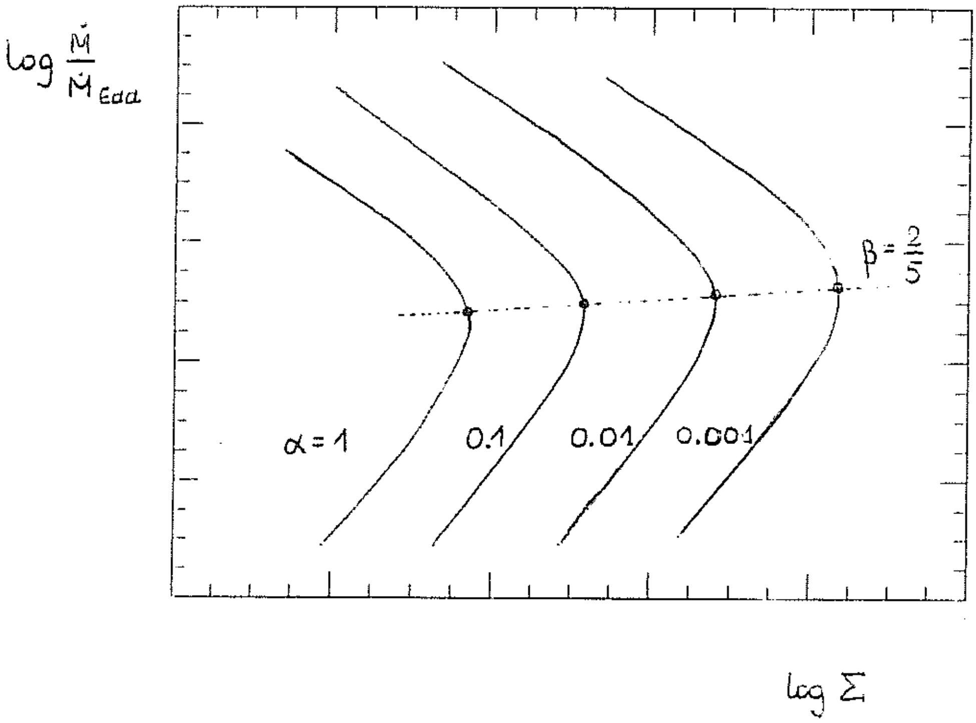

Figure 18: Lower and middle branches for different values of the viscosity coefficient

where κ_e is the opacity due to electron scattering and the second term describe the free-free absorption, $\kappa_0 = 0.64 \times 10^{23}$. We can obtain the asymptotic relations for Σ when free-free absorption become dominant, using the new form of κ. In case (I) (gas pressure greater than radiation pressure) opacity has the form:

$$\kappa \approx \kappa_0 \dot{m}^{-1}$$

The result does not depend on m and α. The surface density is given by

$$\Sigma \approx m^{1/5} \dot{m}^{7/5} \alpha^{-4/5}.$$

In case (II) (radiation pressure is grater then gas pressure)

$$\kappa \approx m^{-1/9} \dot{m}^{-16/9} \alpha^{-1/9}$$

and

$$\Sigma \approx m^{8/9} \dot{m}^{7/9} \alpha^{-8/9}.$$

The slope of the $\dot{m}(\Sigma)$ relation changes direction somewhere near $\kappa_e \approx \kappa_{ff}$. Schematically it is shown in Figure 19. Again one turning point can be found requiring that $log\Sigma/log\dot{m} = 0$. For this purpose we introduce a new quantity, ξ, which is the ratio of free-free absorption coefficient to the total opacity. We find at the turning point that

$$\xi = \frac{8}{15}.$$

This means that the ratio of free-free absorption to electron scattering must be equal to $\frac{8}{7}$ at the turning point.

b) Different viscosity prescriptions

The viscosity coefficient α may strongly depend on the accretion rate, due, for example, to the Papaloizou and Pringle (1984, 1987) instability, which for very small accretion rates may produce strong turbulence and thus viscosity, but for higher accretion rates switches off (Blaes, 1987). Assume that the viscosity coefficient depends on the accretion rate through the purely phenomenological relation

$$\alpha = \alpha_0 exp(-k\dot{M}/\dot{M}_C). \qquad (55)$$

The Shakura-Sunyaev models ($k = 0$) and their modifications ($k = 0.1,\ 1.$) are shown in the Figure 20.

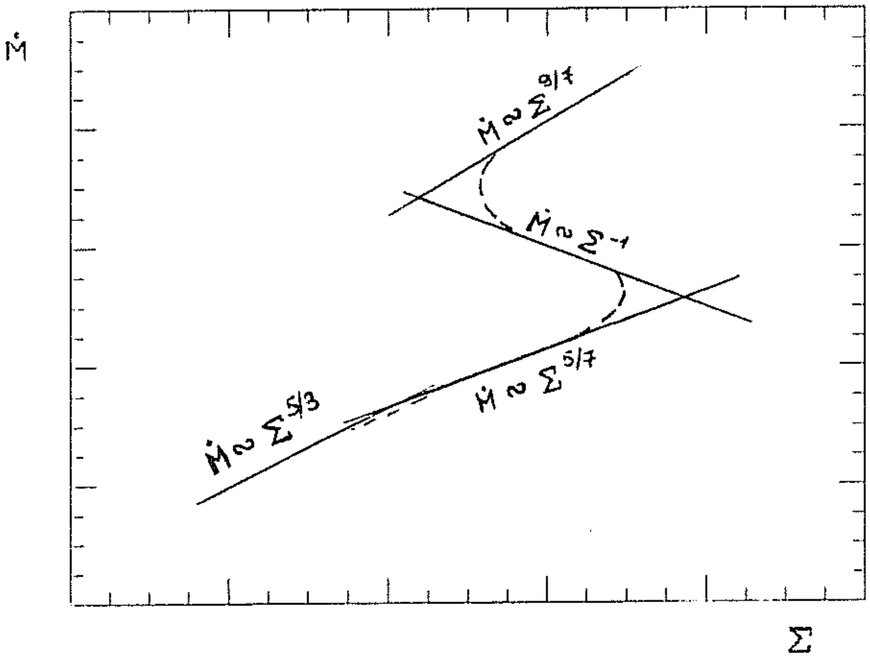

Figure 19: The influence of the opacity on the $\dot{m} - \Sigma$ relation.

c) The angular momentum is not exactly Keplerian

Consider the angular momentum which is not exactly Keplerian. The hydrostatic equilibrium in the radial direction has the form:

$$\frac{1}{\rho}\frac{dP}{dr} = r(\Omega^2 - \Omega_K^2).$$

We have allowed for some deviation from this standard distribution, keeping the derivative of angular velocity still equal to the derivative of the Keplerian angular velocity. We have found: $\Omega^2 \approx \dot{m}$. Therefore the surface density is described as follows

$$\Sigma \approx m^{-1}\alpha^{-1}.$$

The result is presented in Figure 21.

d) Turning on the heating (cooling) in the Shakura-Sunyaev approximation

The only difference we did was to add a new term in the energy

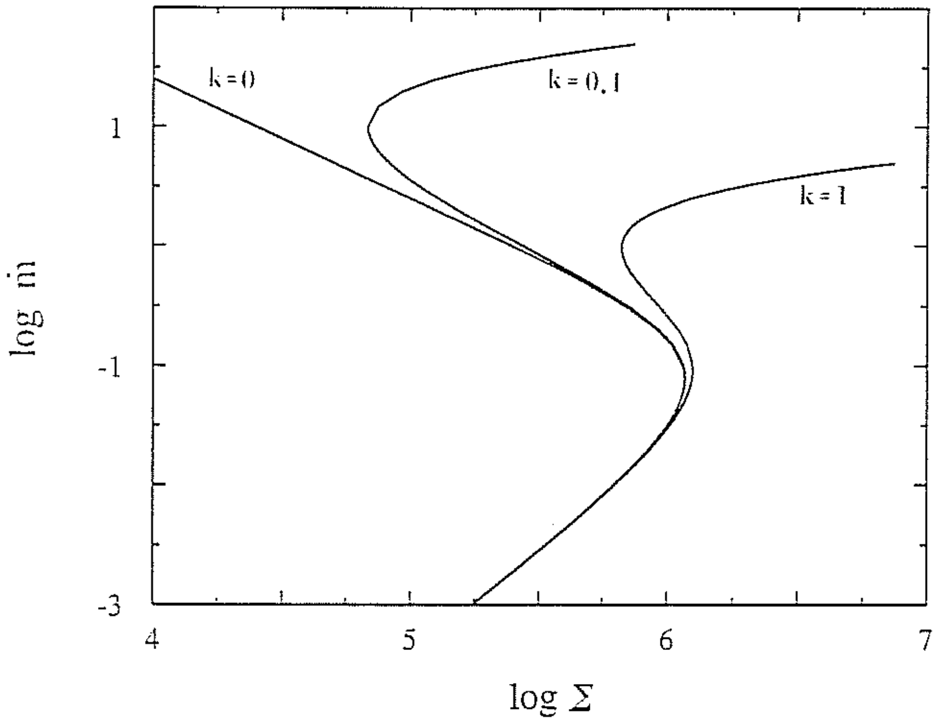

Figure 20: The $\dot{m}(\Sigma)$ relation for the Shakura-Sunyaev models with modified α viscosity given by equation (55).

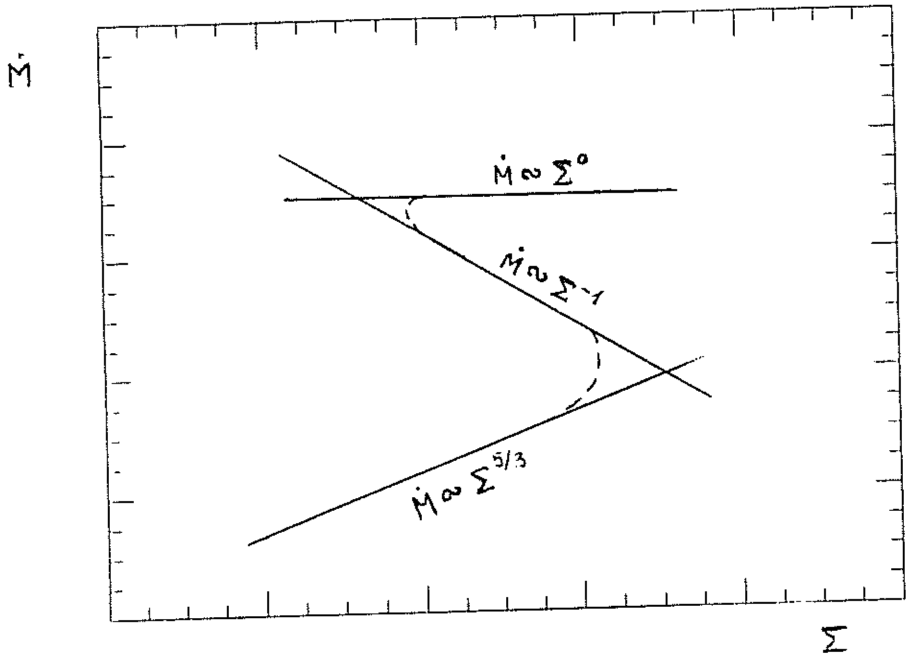

Figure 21: The $\dot{m}(\Sigma)$ relation showing the influence of the slightly different angular momentum distribution.

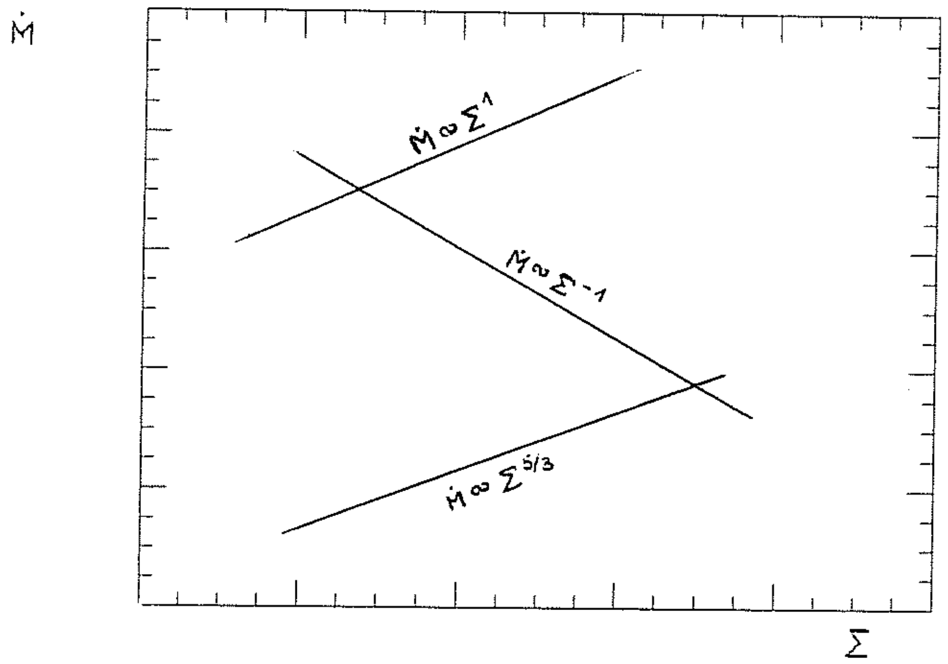

Figure 22: The effect of the additional term in energy balance equation.

balance equation. Equation (3) now has the form:

$$\dot m \mathcal{F}\mathcal{D} + q = 4\pi r F^- \tag{56}$$

We will consider only the case of radiation pressure dominance, when the additional heating (cooling) can stabilize the middle branch. The radial heat transfer can be written in the following way:

$$q \approx \pm 8 B_1 \frac{\dot m P}{\rho r}$$

This approximation leads us to a new surface density-accretion rate relation

$$\Sigma \approx \frac{1}{16\pi} r^{-3} B_1 \mathcal{D} \Omega_K \dot m \alpha^{-1} \tag{57}$$

The surface density does not depend on the mass of the black hole. The $\dot M - \Sigma$ relation has a positive slope. The effect of an additional term in the energy balance equation is shown in Figure 22.

3.4 A single disk with fixed accretion rate

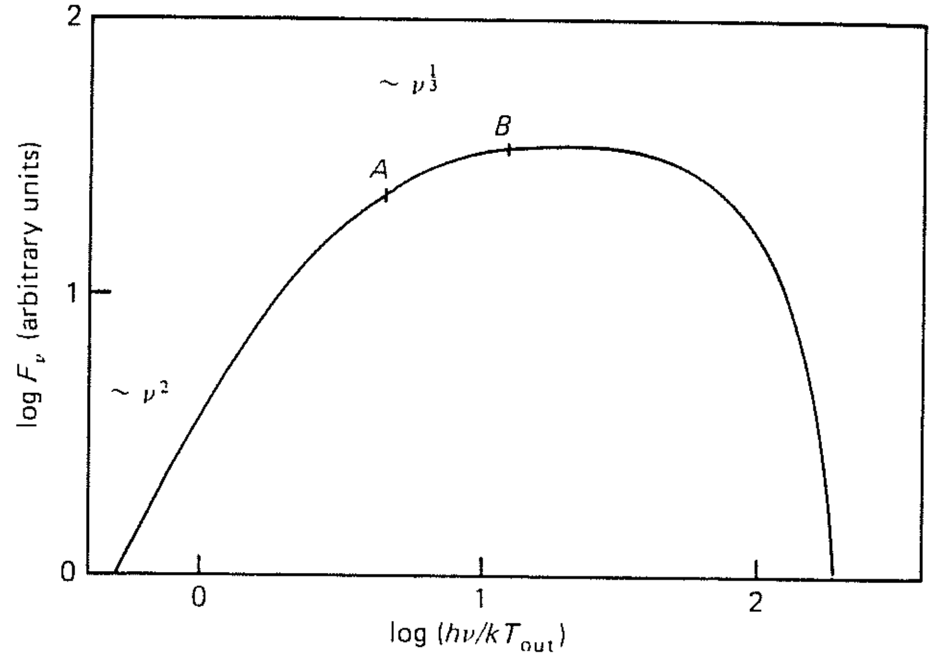

Figure 23: The standard disk spectrum.

The maximum temperature in the disk appears at about $r \approx 2r_{in}$. The dQ_+/dr is equal to zero there. This is a property which does not depend on m, $\dot{m}$, α. At this point the maximum temperature is given by

$$T_{max} \approx m^{-1/4}\dot{m}^{1/4} \tag{58}$$

assuming thermal radiation from the disk. The maximal emission frequency

$$\omega_{max} \approx m^{-1/4}\dot{m}^{1/4} \tag{59}$$

occurs in the range from optical to x-rays for disks around galactic black holes ($10M_\odot$) and in the optical/ultraviolet for supermassive black holes (10^8). The standard shape of the spectrum radiated from the disk is shown in Figure 23.

4. Thick accretion disks

In the standard theory of accretion disks described in the previous chapter one assumes a priori that the angular momentum distribution is Keplerian and that dissipative processes can be expressed by α-viscosity law.

Abramowicz, Jaroszyński and Sikora (1978), Kozlowski, Jaroszyński and Abramowicz (1978), Paczyński and Wiita (1980), Jaroszyński, Abramowicz and Paczyński (1980) proposed a new type of accretion disk, a thick disk, due to its almost spherical shape. In order to construct a model, a surface distribution of angular momentum and flux radiation is assumed. Given these two functions one can compute not only the total luminosity L and the accretion rate, $\dot{M}$, but also other disk characteristics.

4.1 Super-Eddington luminosities

It is well known that if the disk's luminosity exceeds the Eddington value then, some material would be blown off by the pressure of the supercritical radiation flux. This may lead to the conclusion that an accretion disk will not be able to have a luminosity much in excess of the Eddington one, because of the strict assumption of the small thickness of the disk. Maximal luminosity of any nonrotating, stationary, electromagnetically neutral object cannot exceed the Eddington luminosity. Only rotating objects can have $L > L_{Edd}$ and the reason for this is the following: in mechanical equilibrium the flux of radiation, emitted locally from the surface of a stationary and electromagnetically neutral body reaches its maximum value when the effective gravitational force is balanced by the radiation-pressure-gradient force. Therefore the maximal luminosity is

$$L_{max} = -\frac{c}{\kappa}\int_{\Sigma} \mathrm{g}_{eff} \cdot \mathrm{d}\Sigma, \qquad (1)$$

where Σ is the surface of the body and $\mathrm{d}\Sigma$ is the oriented surface element, g_{eff} is the effective gravity on the surface. In the case of a rotating object we have

$$\vec{\nabla} \cdot \vec{g_{eff}} = 4\pi G\rho - 2\sigma^2 + 2\omega^2 \qquad (2)$$

the rotating matter. The existence of the cusp for any stable angular momentum distribution is due to the reason that the distribution of l is stable if l increases outward (Seguin, 1975). Therefore in general, the angular momentum distribution can cross the Keplerian one in two points exactly like in the $l =$ constant case (Figure 1).

Abramowicz, Jaroszyński and Sikora (1978) gave five topological possibilities for the cusp existence, (all quantities are explained in Figure 1):

1) $l_0 < l_{ms}$. A disk will not form.

2) $l_0 = l_{ms}$. The disk exists as an infinitesimal thin unstable ring, located on the circle $r = r_{ms}$.

3) $l_{ms} < l_0 < l_{mb}$. Many disks can form without cusp but only one with a cusp.

4) $l_0 = l_{mb}$. A cusp is formed and is located on the marginally closed equipotential surface.

5) $l_0 > l_{mb}$. The disk has no cusp.

The cusp is located between the marginally bound and marginally stable circular orbit, and very close to the sonic point. For the Schwarzschild black hole it is

$$2r_G < r_S < 3r_G$$

where r_S is the location of the sonic point. When $\dot{M} \ll \dot{M}_C$ the cusp and the sonic point coincide with the marginally stable orbit, while for $\dot{M} \gg \dot{M}_C$ the cusp goes very close to the marginally bound orbit. The energy per particle released in the process is the binding energy of the circular orbit located at the cusp. Since this goes to zero at the marginally bound orbit a stationary disk with $\dot{M} \gg \dot{M}_C$ has very low efficiency compared to a standard disk.

There are two families of thick disk models: Jaroszyński's disks and b-disks (Jaroszyński, Abramowicz and Paczyński, 1980). These families together cover a substantial range of a physically relevant disk. $l(r)$ is subject to the following restrictions:
(hydrodynamic stability)

$$\frac{\partial l}{\partial r} \geq 0$$

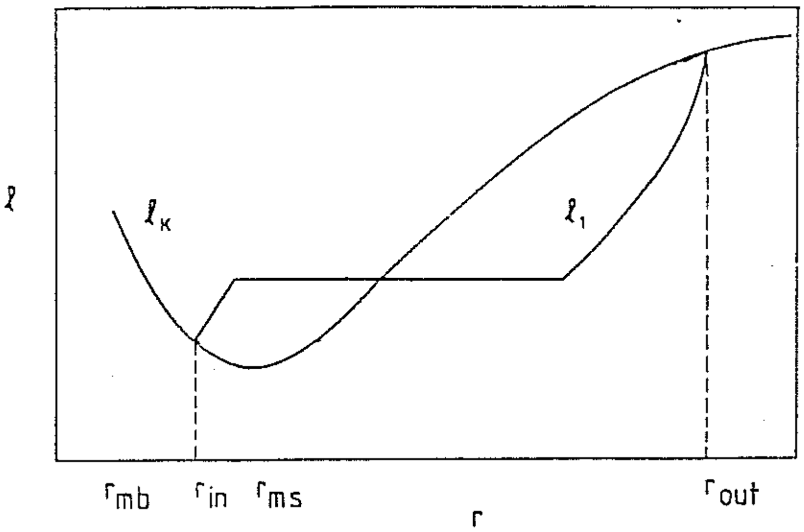

Figure 2: The Jaroszyński angular momentum distribution

(positive accretion)

$$\frac{\partial(lr^{-2})}{\partial r} \leq 0$$

and (mechanical equilibrium)

$$\int_{r_{in}}^{r_{out}} (l_K^2 - l^2) r^{-3} dr = 0.$$

The boundary conditions require the angular momentum to be Keplerian at both the inner and outer edges. These two sets of models are very different within the funnel region. In the first set, the disk surface rotates rigidly (Ω =constant) in the region close to the cusp, $r \geq r_{in}$. In the second family, the angular momentum, l, is constant in this region. These two cases are limiting cases and a real disk should have its properties in between near the cusp. Because of stability problem and restrictions given by the outer boundary conditions neither Ω = constant nor l = constant can be continued all the way from r_{in} to r_{out}. There are many possibilities to choose an angular momentum distribution in the remaining part of the disk. Following Jaroszyński, Abramowicz and Paczyński (1980) we discuss two of them here.

The first is shown in Figure 2. Abramowicz, Calvani and Nobili (1980) showed that this particular distribution maximizes the luminosity for a given r_{in} and r_{out}. Both the thick disk luminosity and accretion rate depends only on r_{in}. The resulting relation between luminosity and accretion rate is shown in Figure 3.

The second is presented in Figure 4. The thick disk surface consists of two sections, one with a constant angular momentum and one with the following prescription:

$$\Omega l^b = \Omega_{out} l^b_{out} = const \quad for \ r_c \leq r \leq r_{out}$$

for some constant b. The exponent b is chosen in such a way that the hydrostatic equilibrium is satisfied ($0 < b < 3$). The relation luminosity - accretion rate also for this case is shown in Figure 3.

Paczyński and Abramowicz (1982) constructed a geometrically thick accretion disk orbiting a 10 $M_\odot$ black hole. The interior is assumed to be in the convective equilibrium, and the accretion flow and heat generation are confined to the layers close to the equatorial plane. I would like to discuss these models in some detail because their structure is very similar to those obtained in a slim disk. Two models are given; one with a critical accretion rate, $\dot{m}$, and another with twice the critical accretion rate. The meridional cross sections of the disk models taken from that paper are shown in Figure 5.

4.3 Roche lobe overflow

Accretion onto the central object in the vicinity of the inner edge is driven by a slight overflowing of a critical equipotential surface, $W = W_{in}$ by the surface of the disk. It represents a small violation of mechanical equilibrium. In this case no viscosity is needed to support the accretion. Such a mechanism was suggested by Paczyński (1978, unpublished). There are three conditions for Paczyński's mechanism to work:

1) The surface $W = W_{in}$ should intersect itself at the inner edge, the central object should be inside the region bounded by $W = W_\infty$, and $|W(r_{in}, 0)| < |W_s| < |W_\infty|$.

2) There should be no infinite potential barrier between r_{in} and the surface of the central object.

3) From the inner edge to the surface of the central object the matter

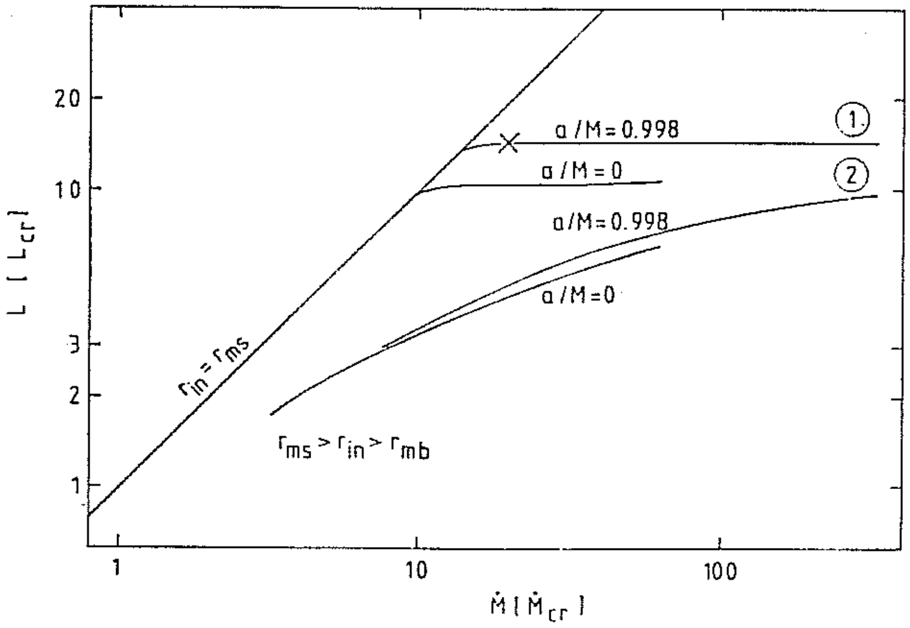

Figure 3: The $L - \dot{M}$ relation for the two described angular momentum distributions. The straight line corresponds to the maximum efficiency of converting accreted mass into outgoing radiation, i.e., to the case $r_{in} = r_{ms}$. $a/M = 0$ - Schwarzschild black hole, $a/M = 0.998$ - "canonical" Kerr black hole. The numbers, 1 and 2 correspond to Jaroszyński distribution and b-distribution of angular momentum (Jaroszyński, Abramowicz and Paczyński, 1978)

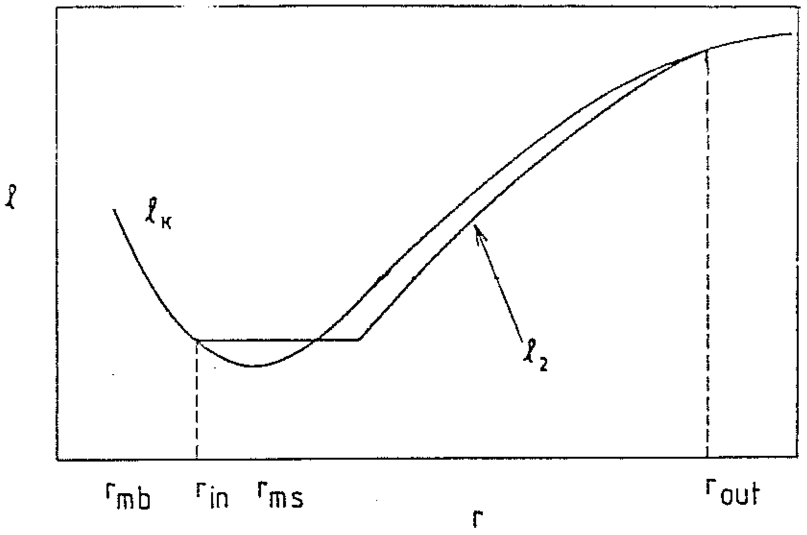

Figure 4: The so-called b-distribution of angular momentum

should move freely - $l = const.$ Between the inner edge and the surface of the central object there should be no stable circular orbits for free particles.

These conditions cannot be satisfied in Newtonian mechanics: Paczyński's mechanism is purely general-relativistic. The reason is that the Newtonian Keplerian distribution of angular momentum is monotonic, while in general relativity it has minimum at the marginally stable circular orbit.

As was noticed by Abramowicz (1981) the mass and energy loss connected with the relativistic Roche lobe overflow mechanism is able to cure a thermal instability to the disk, at least close to the sonic point. This will be discussed in detail in the Chapter 5.

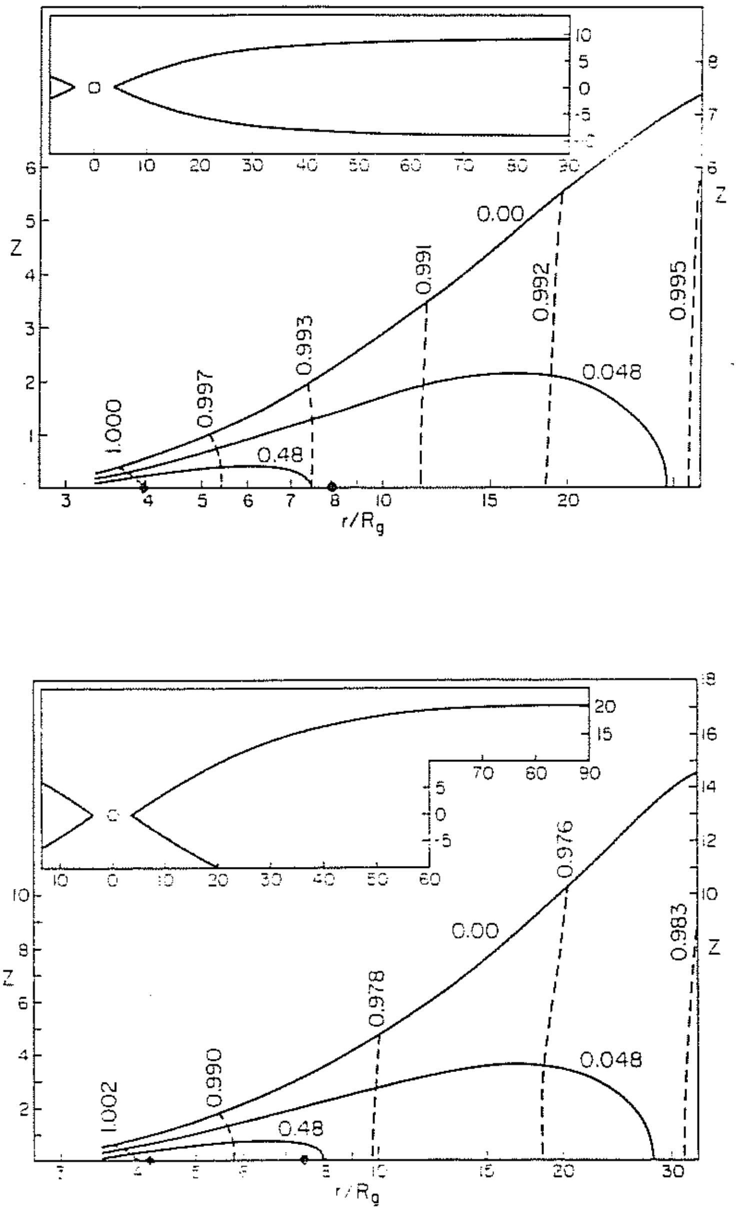

Figure 5: The meridional cross sections of a disk model with $\dot{m} = 1$ and $\dot{m} = 2$.

5. Slim accretion disks

The slim accretion disk models (Abramowicz, Czerny, Lasota and Szuszkiewicz, 1988) take advantage of the simplification due to vertical integration as used for the thin disks, but at the same time they use the correct thick disk approach to the transonic part of the flow. The momentum and energy equations for the slim disk, which we take from Paczyński and Bisnovatyi-Kogan (1981), contain more terms than the standard Shakura-Sunyaev (1973) equations. The additional inertial term, $v_r dv_r/dr$, describing the dynamical importance of the accretion velocity v_r, and the horizontal pressure gradient term, $\rho^{-1}dP/dr$ are included in the momentum equation, while the advective, horizontal heat flux, $v_r T dS/dr$, is added to the energy equation. The remaining equations are the same as the Shakura-Sunyaev ones. The pseudo-Newtonian potential (Paczyński and Wiita, 1980) is used to describe the gravitational field of the central black hole. The inner boundary condition uses the fact that there is no viscous torque across the surface of the black hole, while the outer boundary condition states that at large radii the model of the flow agrees closely with that of Shakura and Sunyaev. The equations together with the boundary conditions and the regularity condition at the sonic point define an eigenvalue problem for l_0, the specific angular momentum of matter crossing the horizon of the black hole. We have solved this eigenvalue problem numerically using a modification of the method described by Muchotrzeb and Paczyński (1982).

Our models form a three parameter family, with dimensionless parameters $(\alpha, \dot{m}, m)$. Here $m = M/M_\odot$ and $\dot{m} = \dot{M}/\dot{M}_C$. The accretion rate is scaled in terms of $\dot{M}_C = 16\dot{M}_E$ rather than $\dot{M}_E$, because, for small accretion rates, $1/16$ is the efficiency of accretion in the pseudo-Newtonian potential. Therefore the total (radiative) luminosity of the disk, expressed in the Eddington units $L/L_E = \eta\dot{M}/\dot{M}_E$ for small accretion rates is equal to $L/L_E = \dot{M}/\dot{M}_C$. Here η is efficiency of accretion. Figure 1 shows the total luminosity for our disk models (solid line) in function of the accretion rate.

The dashed line represents the rate of energy generation by viscous

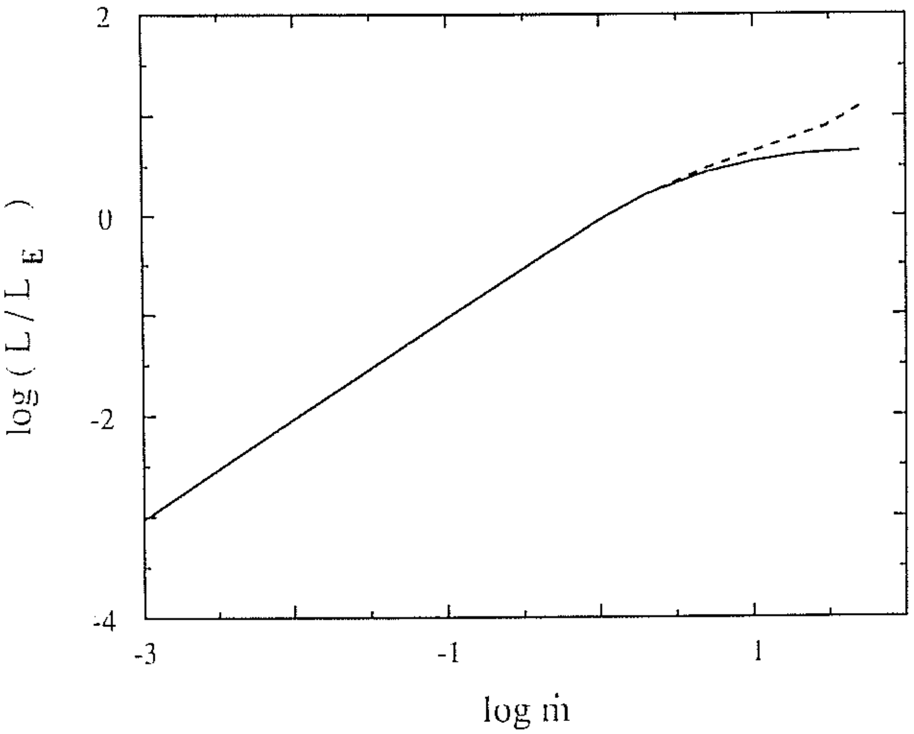

Figure 1: The total luminosity for slim disk models (solid line) in the function of the accretion rate $\dot{m}$. The dashed line represents the rate of energy generation by viscous stresses. $\dot{m}$ is a accretion rate in terms of critical accretion rate, $\dot{M}_C = 64\pi GM/c\kappa_{es}$. All the models are computed with central black hole mass $M = 10M_\odot$, viscosity parameter $\alpha = 0.001$.

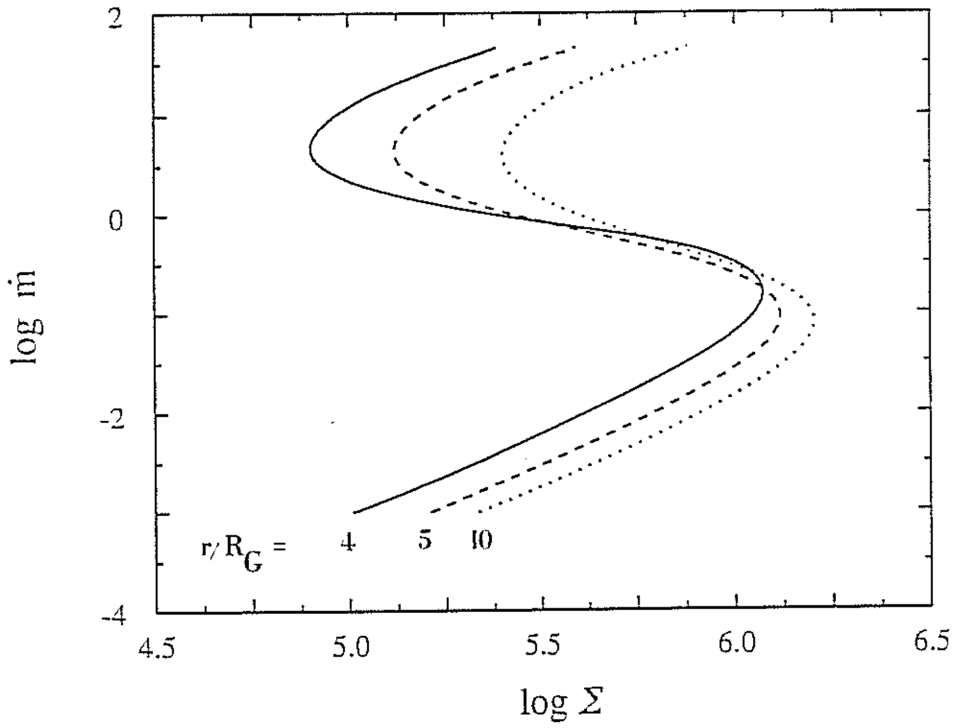

Figure 2: The $\dot{m}(\Sigma)$ relation for slim disk models for three fixed radii, $r/R_G = 4$ (solid line), 5 (dashed line), 10 (dotted line). Σ is a surface density in gcm^{-2}.

stresses. The gap between these lines is due to heat lost through the inner disk radius: for higher accretion rates the heat trapped in matter becomes important, and the flow of matter induces non negligible advective, horizontal heat flux. Thus, for higher accretion rates efficiency goes down and luminosity increases not in proportion to the accretion rate, but slower (Jaroszyński et al., 1980, Chapter 4, Figure 3). Smaller efficiency means that the inner radius of the disk goes closer to the black hole.

Sequences of models with different accretion rates, $0.001 < \dot{m} < 50$, and with the two other parameters fixed at $m = 10$ and $\alpha = 10^{-3}$, are shown in Figure 2. The relation between the accretion rate $\dot{M}$ and the surface density Σ at the fixed radius R has a characteristic S-shape with the three branches (lower, middle and upper) defining three regimes of accretion. On the *lower branch* the gas pressure P_g is greater than the radiation pressure P_r and the opacity is dominated by electron scattering. The cooling is provided by the vertical radiative flux. Accretion is stable against local thermal and viscous perturbations - as indicated by the positive slope of $\dot{M} = \dot{M}(\Sigma)$. On the *middle branch* the opacity and cooling mechanism are the same as on the lower branch, but $P_g \ll P_r$ here. Accretion is thermally and viscously unstable - as indicated by the negative slope of $\dot{M} = \dot{M}(\Sigma)$. The thermal instability is due to an insufficient dependence of the rate of radiative cooling Q^- on the vertical thickness of the flow H. For radiative cooling $Q^- \approx H$, while for viscous heating $Q^+ \approx H^2$. Thus, overheating causes expansion and expansion overheating and a thermal runaway instability arises (Pringle, Pacholczyk, and Rees, 1973). The general criterion for thermal stability of the Shakura-Sunyaev model is $(\partial lnQ^+/\partial lnH)_\Sigma < (\partial lnQ^-/\partial lnH)_\Sigma$ which, for this model, is equivalent to $\beta = P_g/(P_g + P_r) > 2/5$. On the *upper branch* accretion flows cannot be described by the Shakura-Sunyaev model. Here $P_g \ll P_r$ and the cooling is provided by both vertical radiative flux and horizontal advection. Because for advective cooling $Q^- \approx H^3$, thermal runaway is avoided and the accretion flow is thermally stable (Abramowicz, 1981). This corresponds to the positive slope of the $\dot{M} = \dot{M}(\Sigma)$ curve.

The existence of the S-shaped $\dot{M} = \dot{M}(\Sigma)$ curves connected with the $\beta > 2/5$ instabilities and advective cooling was first suggested in 1985 by Abramowicz and Lasota in an unpublished paper (see also Abramowicz, Lasota and Xu, 1986). The analogy with the dwarf novae case (Smak, 1984) is quite appealing. It may indicate the possibility of quasi-periodic outbursts or switching between high and low states for flows with accretion rates which belong to the unstable middle branch of the $\dot{M}(\Sigma)$ curve.

5.1 Basic assumption and equations of the model

Paczyński and Bisnovatyi-Kogan (1981) assumed that the vertical thickness of the flow, $H(r)$, is much smaller than the corresponding cylindrical radius, $H/r = \epsilon \ll 1$, and in each equation kept only terms of lowest order in ϵ. For the dimensionless ratios of the horizontal velocity component v_r, and the sound velocity $v_s = (\partial P/\partial \rho)_S^{1/2}$ with the azimuthal velocity component, v_φ, they adopted $v_r/v_\varphi \approx \epsilon^2$ and $v_S/v_\varphi \approx \epsilon$. Because the vertical velocity component v_z is of the order of ϵv_r , they assumed that $v_z = 0$. They also assumed $\partial v_r/\partial z = 0$ and $\partial v_{varphi}/\partial z = 0$. Strictly speaking, these assumptions about the velocity field can be made *independently* of the assumption $H/r \ll 1$ and one can obtain consistent physical models with $H/r < 1$. Therefore, the physical validity of the model is not directly connected with the small vertical thickness of the flow. However, the numerical method used here works for not too high accretion rate, $\dot{m} < 50$. Numerical difficulties are connected with the radial integration (iteration to get the eigensolution which crosses the critical point); they do not depend on the accuracy of the vertical structure.

If the action of viscosity is due only to shear viscosity and the bulk viscosity can be neglected, the above assumption assure that the only relevant component of the viscous stress tensor entering the Navier-Stokes equations for the slim disk is

$$\tau_{\varphi r} = \tau_{r\varphi} = \rho\nu\Omega(\frac{dln\Omega}{dlnr}) \tag{1}$$

where ν is the kinematic coefficient of shear viscosity and $\Omega = v_\varphi/r$ is the angular velocity of rotating matter. According to the Shakura-Sunyaev (1973) viscosity prescription,

$$\tau_{\varphi r} = -\alpha P \tag{2}$$

where $\alpha = const$ is a dimensionless, phenomenological viscosity parameter and the pressure is taken at the equatorial plane, $z = 0$. According to (2) the viscous torque across a cylindrical surface $r = const$ is $g(r) = 4\pi r^2 \alpha P H$. Using (8) this can be written as $g(r) = \dot{M} r (P/\rho) B_2 v_r$. Because $v_r(R_G) = \infty$, one has $g(R_G) = 0$, i.e. there is no viscous torque across the surface of the black hole. Although this gives no additional restriction, we shall call the fact that $g(R_G) = 0$ *the inner boundary condition.* It will be used later for the integration of the angular momentum balance equation. General relativistic effects are included in our purely Newtonian treatment by using the pseudo-Newtonian potential (Chapter 3, eq.(1)). The self-gravity of the accretion disk is totally neglected. The radial component of the gravitational force on the equatorial plane $z = 0$ can be written conveniently as l_K^2/r^3 or $\Omega_K^2 r$, where l_K and Ω_K are the specific angular momentum and angular velocity on Keplerian, circular orbits in the pseudo-Newtonian potential . The stable Keplerian orbits, with $dl_K/dR < 0$, have radii greater than the radius R_{MS} of the marginally stable orbit located at $R_{MS} = 3R_G$ and the binding energy of the Keplerian orbits, $E_K = \Psi + (\Omega_K l_K)/2$, changes sign at R_{MB}, the radius of the marginally bound orbit. Orbits with radii $R < R_{MB} = 2R_G$ are unbound. The standard equation of state for a mixture of perfect gas and radiation is assumed:

$$P = \frac{\mathcal{R}}{\mu}\rho T + \frac{a}{3}T^4, \tag{3}$$

where μ is the mean molecular weight ($\mu = 0.6$ in what follows). The first law of thermodynamics is used to calculate the entropy gradient in terms of density and temperature gradients:

$$TdS = \frac{P}{\rho}[(12 - 10.5\beta)\frac{dT}{T} - (4 - 3\beta)\frac{d\rho}{\rho}]. \tag{4}$$

All of the quantities in our model are defined on the equatorial plane. The equations containing only thermodynamical quantities or their functions (equation of state, first low of thermodynamics, viscosity prescription, opacity law) refer to the equatorial plane with no change in form. The same is true for the momentum equation in r and φ directions which contains no z derivatives:

$$\frac{1}{\rho}\frac{dP}{dr} - (\Omega^2 - \Omega_K^2)r + v_r\frac{dv_r}{dr} = 0, \tag{5}$$

$$\dot{M}(l - l_0) = g(r) - g(R_G) = 4\pi r^2 H\alpha P \tag{6}$$

In the derivation of the last equation the inner boundary condition was used. The equation of hydrostatic equilibrium in the z direction, the continuity equation, and the energy equation, which contain z derivatives, are all integrated vertically. As the vertical disk structure is known only approximately, the results of the integration contain some correcting factors B_i, all of the order of unity. They convert the average vertical values of their $z-$integrated quantities to their equatorial plane values used in our model. In particular, the equation of hydrostatic equilibrium in the z direction and the continuity equation read:

$$\Omega_K^2 H^2 = B_4\frac{P}{\rho}, \qquad B_4 = 6 \tag{7}$$

$$\dot{M} = B_5 4\pi r H\rho v_r, \qquad B_5 = 0.5, \tag{8}$$

while the energy equation is

$$\dot{M}(l - l_0)(-\frac{d\Omega}{dr}) + B_1\dot{M}T\frac{dS}{dr} = 4\pi r F^-, \qquad B_1 = 0.67 \tag{9}$$

In the energy equation the term connected with the horizontal flux of radiation has been neglected, since it is always much smaller than the other terms, and in particular, much smaller than the vertical radiation flux, F^-:

$$F^- = B_3\frac{c}{\kappa\rho}\frac{aT^4}{3H}. \tag{10}$$

The last formula assumes that the effective optical depth in the vertical direction,

$$\tau_{eff} = (\kappa_{es}\kappa_{ff})^{1/2}(\Sigma/2) \tag{11}$$

is greater than one, and therefore radiation transfer can be treated in diffusion approximation. Here κ_{es} and κ_{ff} are the electron scattering and free-free opacity coefficients, and $\Sigma = 2H\rho$ is the surface density. In the numerical calculations the opacity coefficient, $\kappa = \kappa(\rho, T)$, was taken from Cox and Steward (1970).

We have adopted values of B_i from Paczyński and Bisnovatyi-Kogan who estimated them using a polytropic equation of state and averaged, somewhat arbitrarily, the $n = 3$ and $n = 3/2$ cases. The solution depends only very weakly on the particular choice of B_i.

From equations (5) and (8) one gets

$$\frac{dln v_r}{dln r} = \frac{a_s^2(1 + dlnH/dlnr) + v_\varphi^2(1 - \Omega_K^2/\Omega^2)}{v_r^2 - a_S^2} \tag{12}$$

where a_S is a "sound" velocity defined by

$$a_S^2 = (\frac{dP}{dr})(\frac{d\rho}{dr})^{-1} \tag{13}$$

Only for isoentropic flows is $v_S = a_S$. The numerator and denominator of the right hand side of (12) vanishes at the same *sonic radius* r_S where

$$v_r^2(r_S) = a_S^2(r_S), \tag{14}$$

$$1 + (\frac{dlnH}{dlnr})_{r_S} = -\frac{v_\varphi^2(r_S)}{a_S^2(r_S)}[1 - \frac{\Omega_K^2(r_S)}{\Omega^2(r_S)}] \tag{15}$$

Because $dlnH/dlnr > 0$, it follows (Abramowicz and Zurek, 1981) that at the sonic radius the angular velocity is *smaller* than the Keplerian value.

5.2 Construction of the model

There are four independent first order derivatives in the problem: two in equation (5) and two in equation (9). However, the number of independent integration constants which uniquely determine a regular transonic solution is not four, but three, because of an extra algebraic condition (15) at the sonic radius. These three independent integration constants may be connected with the physical conditions at very large radii where we assume that the solution agrees very closely, although not identically, with that of Shakura-Sunyaev. In the Shakura-Sunyaev approximation to the full problem one neglects the horizontal pressure gradient dP/dr and inertial force $v_r dv_r/dr$ in equation (5) and the entropy gradient in equation (9). Equation (5) reduces to $l = l_K$ or $\Omega = \Omega_K$. Putting this into the already reduced equation (9) eliminates the last derivative from the problem, which becomes purely algebraic. The location of the inner edge in the Shakura-Sunyaev model is given by $r_{in} = 3R_G$. It is assumed that in this model $g(r_{in}) = 0$. Therefore, the constant $l_0 = l_K(3R_G) = (3/2)^{3/2} R_G c$. The algebraic equations which determine the Shakura-Sunyaev solution are nonlinear and we have solved them numerically. However, when opacity is dominated either by gas, or radiation, the asymptotic forms derived in the Chapter 3 can be used. The Shakura-Sunyaev model is artificial singular at $r = 3R_G$. This is caused by incorrect treatment of the flow close to r_{in}, as first noticed Stoeger (1976). Slim disk models are similar to the thick ones at small radii and they have no singularity in r_{in}.

Our method of constructing a regular solution with "almost" Shakura-Sunyaev outer boundary conditions follows, with only minor modifications, that of Muchotrzeb and Paczyński (1982). We recall here only the most important features of it, leaving the technical details of the numerical code to the later section.

First, the value of the central mass M and viscosity parameter α are specified. Next, a value of $\dot{M}$ is chosen, and then, with these values of M, α, $\dot{M}$ we construct the Shakura-Sunyaev solution. This solution is used to determine an initial estimate of the three integration constants needed to start integration from r_{out} downstream. The fourth has already been fixed - it is $\dot{M}$. However, for a *regular* solution, the three integration constants cannot all be given by their Shakura-Sunyaev values, as they are not independent: the regularity condition at the sonic radius (15) gives an implicit relation between them which is not known a priori. Thus, the initial choice of the three constants must be adjusted, until, for a particular set, a regular transonic solution is found. In the actual numerical procedure instead of adjusting the three outer boundary conditions (i.e. the three integration constants) we change only the integration constant l_0, the angular momentum of matter at the surface of the central black hole. It appears in equation (6) and, as we explained earlier, is the eigenvalue of the problem. The above procedure leaves two unspecified constants in the problem,

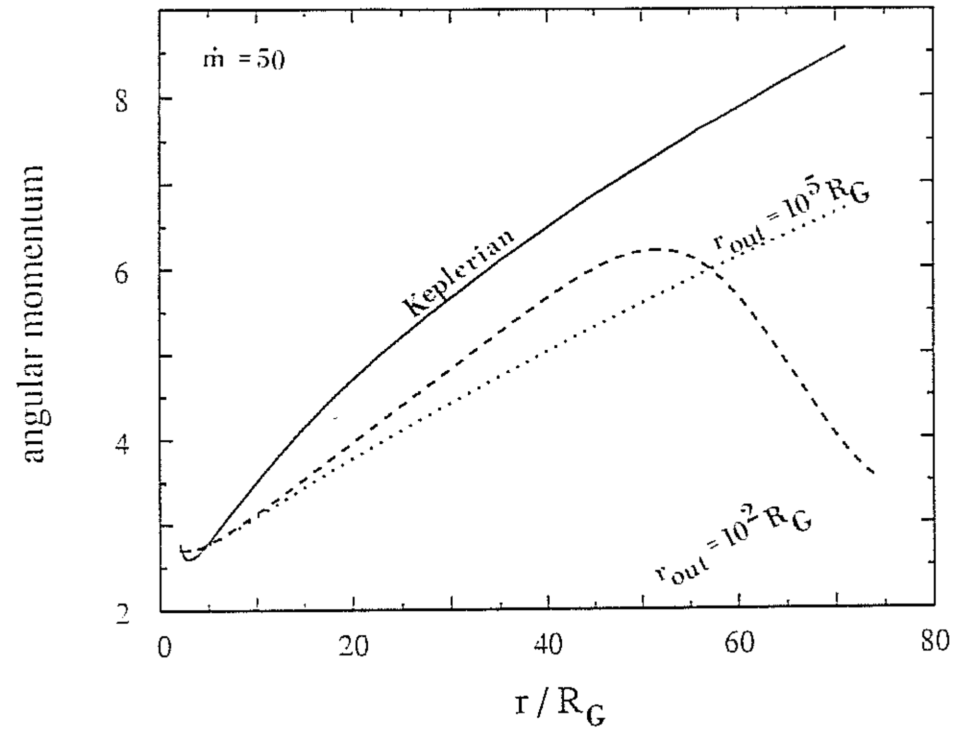

Figure 3: The angular momentum distribution for the model with $\dot{m} = 50$ and boundary conditions given in $r_{out} = 10^2 R_G$ (dashed line) and $10^5 R_G$ (dotted line). Solid line represents the Keplerian angular momentum. Angular momentum is given in $(GMR_G)^{1/2}$.

connected with differences between the functions at the outer radius r_{out} and their Shakura-Sunyaev values. However, the solution at small radii is almost completely insensitive to these remaining degrees of freedom: when the outer boundary conditions are close to the Shakura-Sunyaev ones, the regular transonic solution at small radii is almost *uniquely* determined by M, α and $\dot{M}$. The value of the outer radius r_{out} where the outer boundary conditions are imposed does not influence the solution at the small radii (Figure 3).

5.3 The S-curves

The most important result found in the paper by Abramowicz, Czerny, Lasota, and Szuszkiewicz (1988) is the existence, at any fixed radius, of an S-shaped relation $\dot{M}(\Sigma)$. We present this first for a fixed radius, $r = 5R_G$, and then for all radii $r_S < r < r_{out}$. We choose the first particular value of $r = 5R_G$ because most of the heat is produced close to $r = 5R_G$

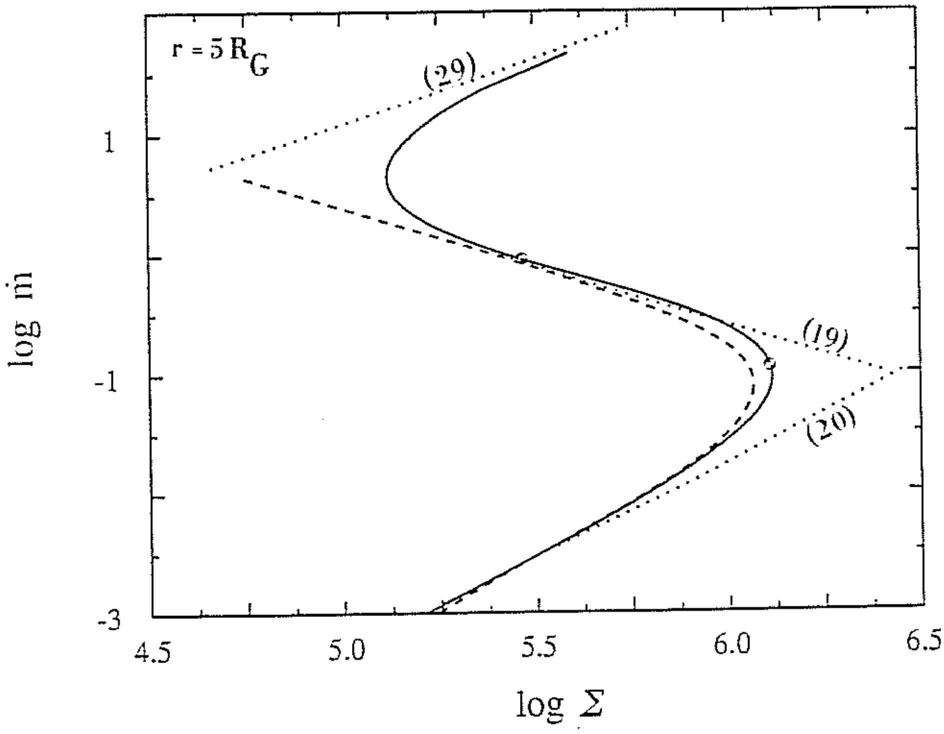

Figure 4: The $\dot{m}(\Sigma)$ relation for $r = 5R_G$. Full transonic solution (solid line), Shakura-Sunyaev approximation (dashed line), analytic asymptotic solutions for the gas dominated (dotted (20) line) and radiation dominated pressure (dotted (19) line), approximation for the upper branch slope dotted (29) line).

(see Figure 12) and therefore this region is most relevant for the observed properties of the disk.

Figure 4 shows the relation between the accretion rate $\dot{M}$ and the surface density Σ at $r = 5R_G$ for models with $\alpha = 0.001$ and $M = 10M_\odot$. The solid curve represents our full transonic solution and the dashed one shows the corresponding Shakura-Sunyaev approximation. The two dotted lines, labelled by (19) and (20), are the analytic asymptotic solutions for radiation dominated pressure and gas dominated pressure, given by equations (**) and (**) in Chapter 3. The meaning of the third dotted line, labelled by (29), was explained also in Chapter 3. The two circles show the models computed by Muchotrzeb and Paczyński (1982). The Figure quite clearly indicates that both the lower and middle branches of the S-curve are very well described by the Shakura-Sunyaev approximation. Thus the physical properties of the accretion flows belonging to these branches, in particular the stability properties, maybe understood in terms of the Shakura-Sunyaev model. Stability properties of the lower and middle branch models have been already summarized in the Introduction. We have recalled there the classical result that the positive slope of the $\dot{M}(\Sigma)$ curve corresponds to stable models and the negative slope - to unstable models. We discussed further details of these models in the Section 3. Now we turn our attention to the upper branch of the S-curve. Obviously, this branch cannot be approximated by the Shakura-Sunyaev model.

General relativistic effects in the gravitational field of a black hole, modelled here in terms of the pseudo-Newtonian potential (*), cause a characteristic behaviour of the equipotential surfaces close to the *inner edge* of the disk, defined as the smaller of the two roots of the equation

$$l(r_{in}) = l_K(r_{in}) \tag{16}$$

The larger root corresponds to the *physical center* of the disk. On the equipotential surfaces, the total potential (gravitational plus centrifugal), defined by

$$W(r,z) = \Psi(r,z) + \int l^2(r) r^{-3} dr \tag{17}$$

is constant. In Figure 5, the equipotential surfaces (solid lines) are shown for a particular model with $\dot{M} = 10\dot{M}_C$. The surface of the disk is marked with dashed lines. The location of the sonic point r_S is indicated by a small cross. Note that $r_S < r_{in}$ in agreement with our comment in connection with equation (15). One of the equipotentials, $W = W_R$, crosses itself at $r = r_{in}$. When $r_{in} < 3R_G$ a characteristic *cusp* is formed at the crossing. If the surface of the disk, $W = W_S$, slightly overflows the critical equipotential $W = W_R$, called *the Roche lobe*, then the mechanical equilibrium is slightly destroyed causing mass loss, and consequently also a heat loss. The physical picture is analogous to Roche lobe overflow in close binaries. In the case when $r_{in} > 3R_G$ no cusp is formed and the Roche lobe mechanism does not operate. The heat loss rate close to the cusp has the behaviour

$$Q^- \approx H^3 \tag{18}$$

Exact formulae for mass loss and cooling due to the Roche lobe overflow mechanism have been given by Abramowicz (1986). The criterion mentioned in the Introduction for thermal stability of Shakura-Sunyaev disk

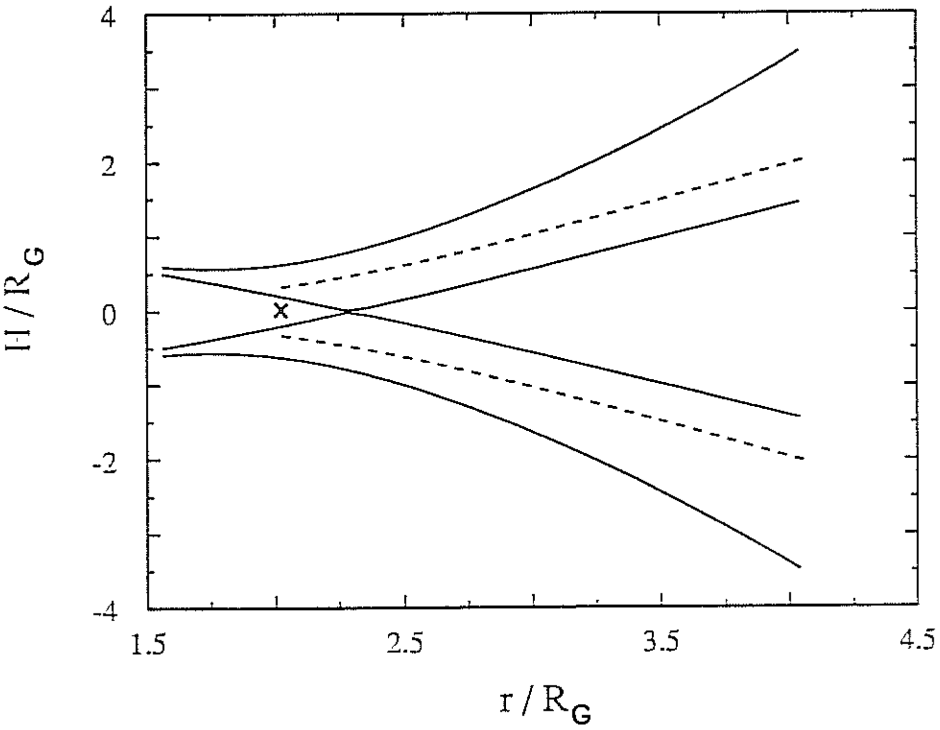

Figure 5: The equipotential surfaces (solid lines)and the surface of the disk model with $\dot{m} = 10$ (dashed lines). Cross indicate the position of the sonic point.

models states

$$(\frac{\partial ln Q^-}{\partial ln H})_\Sigma > (\frac{\partial ln Q^+}{\partial ln H})_\Sigma \qquad (19)$$

and will be described in full details in the Chapter 7. Because for the standard viscosity law (2) the right hand side of this inequality is equal to 2, and for Roche lobe overflow cooling the left hand side is equal to 3, according to (18), the inequality is fulfilled, which means that the region of the disk cooled by the Roche lobe overflow mechanism is thermally stable.

For small accretion rates the stabilized region lies in the immediate vicinity of the inner edge, but for $\dot{M} \geq \dot{M}_C$ the size of the region is substantially greater, as demonstrated by the following argument. Consider a fluid element located at a distance Δr from the inner edge of the disk, in the unstable part. The element expands vertically in the *thermal* time $t_{th} = 2\pi/\Omega\alpha$ because of the overheating caused by the thermal instability. At the same time it is traveling downwards in a radial drift time, t_{dr} which, in Shakura-Sunyaev model, equals the viscous time, $t_{vis} = t_{th}(H/r)^{-2}$. If the element is able to arrive at $r = r_{in}$ before it expands the distance H, the Roche lobe overflow mechanism will cool the element, and the instability will be suppressed. Therefore, in the stabilized region $t_{vis} \approx t_{th}$, or $H \approx r$. In the above argument the expressions for t_{th} and t_{vis} have been taken from Shakura-Sunyaev model, which assumes a Keplerian distribution of angular momentum. However, for the disk with sufficiently high accretion rates the angular momentum at small radii is not Keplerian, but almost constant (see Figure 9). Thus less viscous reprocessing of the angular momentum is needed and the element travels the distance Δr in a time shorter thant_{vis}. This simple argument correctly predicts that the Roche lobe overflow stabilization is important for flows with accretion rates $\dot{M} \approx \dot{M}_C$ or greater, and therefore, that the S-curve should bend at approximately $\dot{M} \approx \dot{M}_C$. The Roche lobe overflow cools down globally the whole innermost part of the disk. Locally, however, at some radius $r < 5R_G$, the advective flux F_{adv} could either cool or heat the flow . At higher accretion rates the advective flux in the more distant parts of the disks is always an important cooling mechanism (Figure 6).

At the radius $r = 5R_G$ the accretion rates at the lower (labelled B) and upper (labelled A) turning points of the S-curve are

$$\dot{M}_B(5R_G) = 0.09\dot{M}_C, \qquad \dot{M}_A(5R_G) = 4.5\dot{M}_C \qquad (20)$$

Figure 7 shows the accretion rates at the turning points for different radii

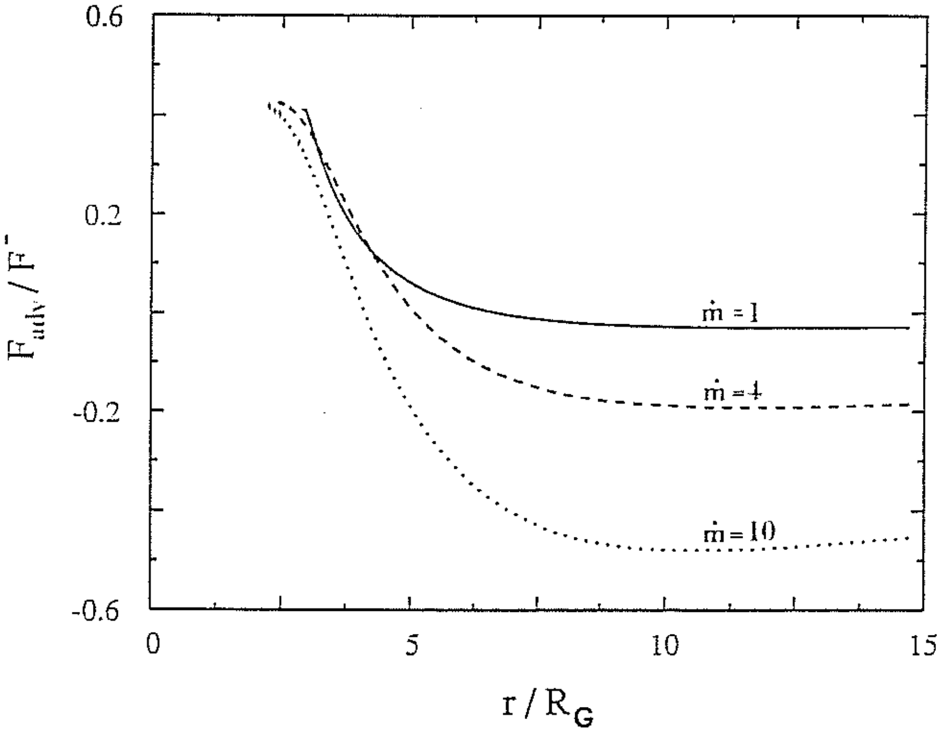

Figure 6: The ratio of the advective and radiative fluxes as a function of radius for three accretion rates $\dot{m}$ = 1, (solid line) 4, (dashed line) 10 (dotted line).

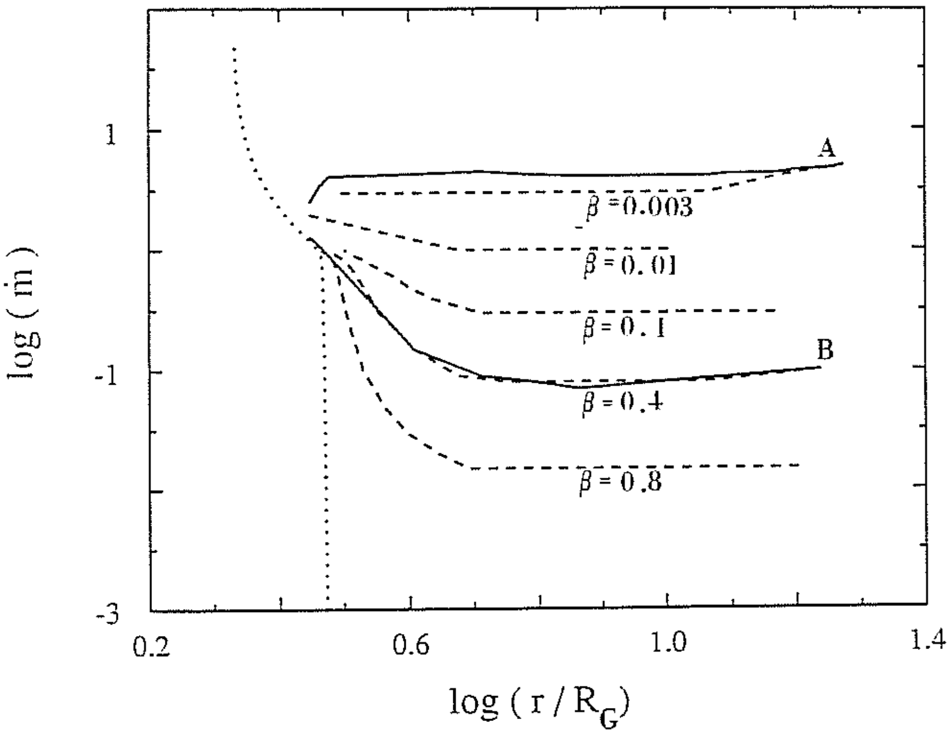

Figure 7: The location of the turning points on the S-curves as a function of radius (solid lines labelled A and B). The dashed lines indicate the lines of the constant β. The dotted one represents the location of the sonic point.

(solid lines marked A,B). In the same Figure the dashed lines are those of $\beta = const.$ They are labelled by the values of β. The dotted line represents the location of the sonic point in the models with different accretion rates.

With the exception of a small region at $r \approx r_S$ the $\dot{M}_B(r)$ curve agrees with that for $\beta = 2/5$ for all r as it should be in the Shakura-Sunyaev model. In particular, for $r = 6.4 R_G$ it has a minimum

$$\dot{M}_{min} = 0.1 \dot{M}_C \tag{21}$$

predicted by the Shakura-Sunyaev model. The Shakura-Sunyaev approximation for the $\dot{M}_B(r)$ curve gives an analytic expression (Abramowicz, 1987, also Chapter 3)

$$\dot{m}(r) = 8.796 \times 10^{-4} \mathcal{C}^{-9/8} \mathcal{R}^{7/16} \mathcal{D}^{7/8} \mathcal{F}^{-1} \alpha^{-1/8} m^{-1/8} \tag{22}$$

This diverges at $r = r_{in} = 3R_G$, but this is an artifact of the Shakura-Sunyaev model, connected with the improper treatment of the flow close to the inner edge. Accretion flows with $\dot{M} < \dot{M}_{min}$ are everywhere stable against the $\beta < 2/5$ instability.

The location of the sonic point changes from the radius of the marginally stable orbit $R_{MS} = 3R_G$ for small accretion rates, to the radius of marginally bound orbit $R_{MB} = 2R_G$ for very high accretion rates. This is typical behaviour for thick accretion disks, which have very low values of $\alpha < 0.001$. (See e.g. Madau, 1988 or Begelman, Blandford and Rees, 1984 for a discussion of the limits on α in thick disk). Kozłowski, Jaroszyński and Abramowicz (1978) proved, using an exact analytic method, that for $\alpha = 0$ the inner edge of a thick disk is always located between R_{MS} and $R_M B$, while other authors (e.g. Paczyński 1980, or Różyczka and Muchotrzeb 1982) who used numerical thick disk models with $\alpha \ll 1$ found a behaviour similar to that shown in Figure 7. However, for accretion flows with higher values of α the situation is remarkably different. We discuss this point in Section 6.

5.4 Details of the slim disk models

Figure 2 in the Introduction shows how the surface density Σ depends on accretion rate for three radii, $r/R_G = 4,\ 5,\ 10$. The behaviour at other radii is similar.

To discuss other properties of slim disks we have chosen five models with

$$\dot{m} = 0.01,\ 0.1,\ 1,\ 4,\ 10,$$

located at characteristic points of the S-curve. (The three branches and two turning points). Figure 8 shows how the thickness of the flow depends on radius for these five accretion rates. The initially thin disk ($H/r \ll 1$) becomes thicker with increasing accretion rate but always remains slim, i.e. the assumption $H/r < 1$ is always satisfied.

The question of how to specify the correct boundary conditions at large radii is not an easy one. Figure 9 clearly indicates that with increasing accretion rate the angular momentum differs more and more from the Keplerian distribution at both small and large radii. The tendency of the angular momentum distribution to become flatter with increasing accretion rate , evident in our numerical models, was found, on general theoretical grounds, by Begelman (1978) in the thick disk case. The agreement suggest a continuous path from slim to thick disks along the sequence of models with increasing accretion rate, correctly placing the slim disks between the thick

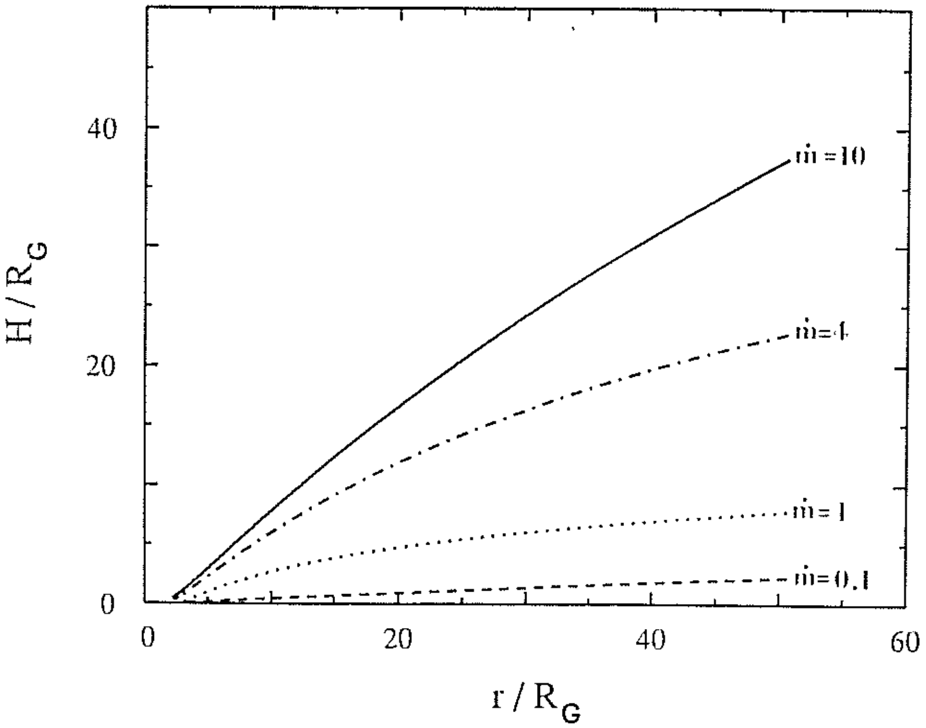

Figure 8: The thickness of the flow for the different accretion rates: $\dot{m} = 0.1$ (dashed line), 1 (dotted line), 4 (dashed-dotted line), 10 (solid line).

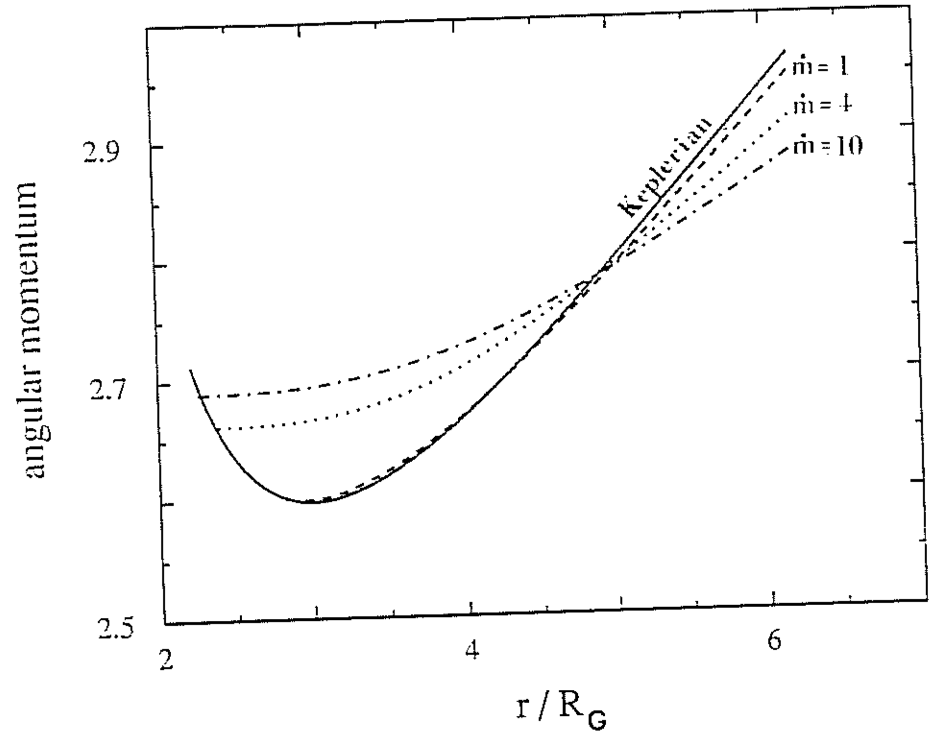

Figure 9: The angular momentum distribution for $\dot{m} = 1$ (dashed line), 4 (dotted line), 10 (dash-dotted line) and the Keplerian one (solid line).

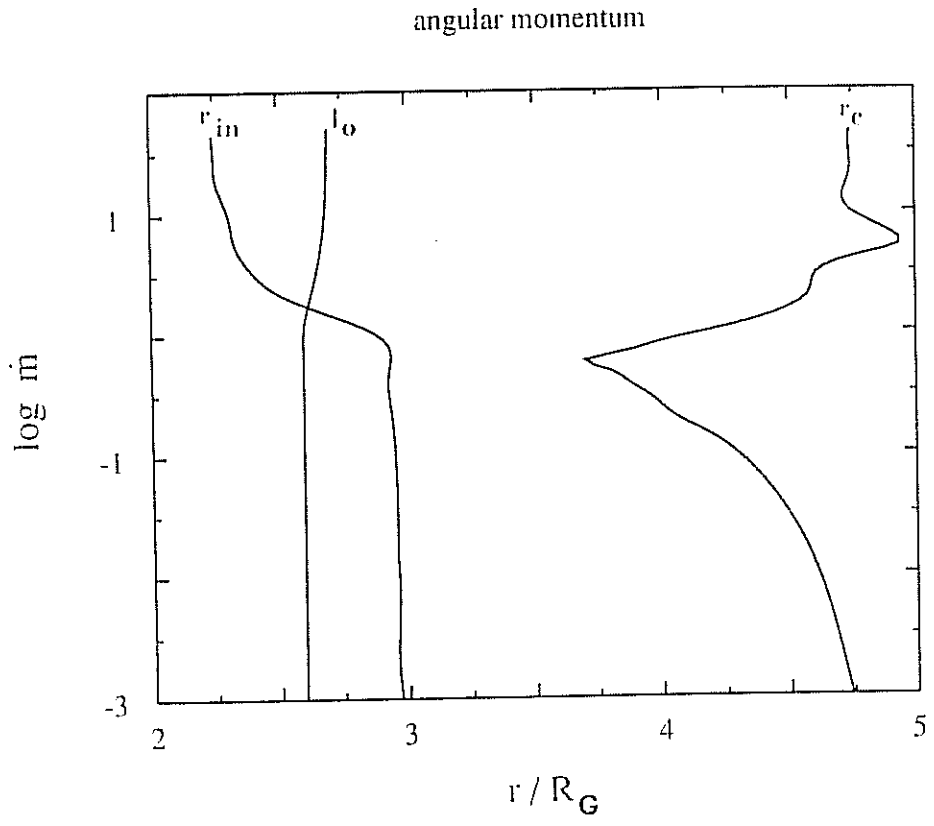

Figure 10: The location of r_{in}, r_c, and l_0 as a function of accretion rate

and thin ones. However, this path cannot be completed in practice with the actual method used by us, because the method fails for $\dot{M} > 50\dot{M}_C$.

We have already discussed the meaning and the physical importance of the points r_c and r_{in} at which $l(r)$ crosses the Keplerian distribution, $l_K(r)$. The location of these points, and the value of l_0, the angular momentum of matter at the black hole surface, are all shown in Figure 10 as a functions of the accretion rate.

For small accretion rates, $l_0 \approx l_{MS}$, and $r_{in} \approx R_{MS} = 3R_G$ as in the standard Shakura-Sunyaev model. The precise location of r_c for small accretion rates cannot be correctly estimated in the standard model, because it depends critically on the details of heat and angular momentum balance which are not treated properly in this model; the curves $l(r)$ and $l_K(r)$ are almost parallel close to $r = r_c$. For high accretion rates, $r_{in} \approx R_{MB} = 2R_G$ and $l_0 \approx l_{MB}$, in excellent agreement with the thick disk theory. Because, as we have already mentioned, for high accretion rates $l(r) \approx$ *const* at small radii, from the above described behaviour of r_{in} and l_0 it follows that, for high accretion rates, r_c should be $\approx 5R_G$, which can clearly be seen to be

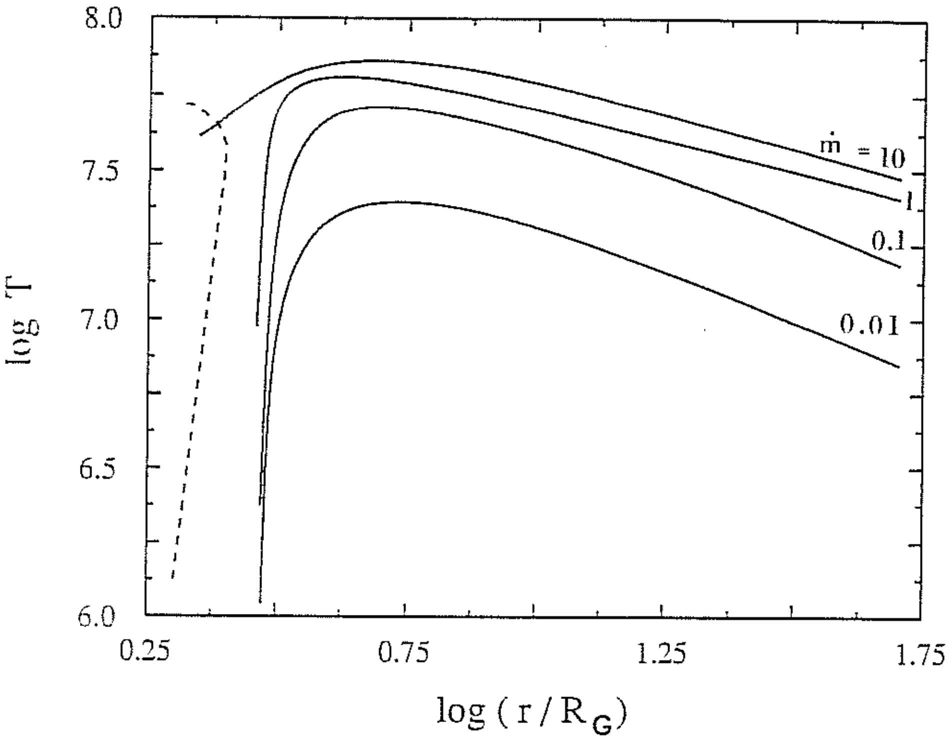

Figure 11: The temperature distribution for models with $\dot{m} = 0.001, 0.1, 1, 10$. The boundary of the region where $\tau_{eff} < 1$ is shown by the dashed line.

the case in our numerical models. Figures 11 and 12 show the variation of the temperature with radius and also the closely connected variation of the vertical radiation flux F^-. These curves are very similar to those familiar from the Shakura-Sunyaev models. In particular, the maximum value of the temperature, T_{max} is reached at a small radius, between $4R_G$ and $6R_G$, with the precise value depending on the accretion rate. The function $T_{max}(\dot{M})$ is shown in Figure 13 by the solid line. The Shakura-Sunyaev model predicts $logT_{max} \approx \frac{1}{4} log\dot{M}$. Our models where constructed for $\tau_{eff} > 1$; c.f. eq (11). This condition was always checked a posteriori and it was found to be true almost everywhere in all the models, with exception of a small region shown in Figure 11 (left from the dashed line).

5.5 Discussion

In this section we discuss only the assumption about the magnitude and form of the viscosity, because only this assumption is really restrictive. Modifications of it introduce *qualitative* changes in the physical properties

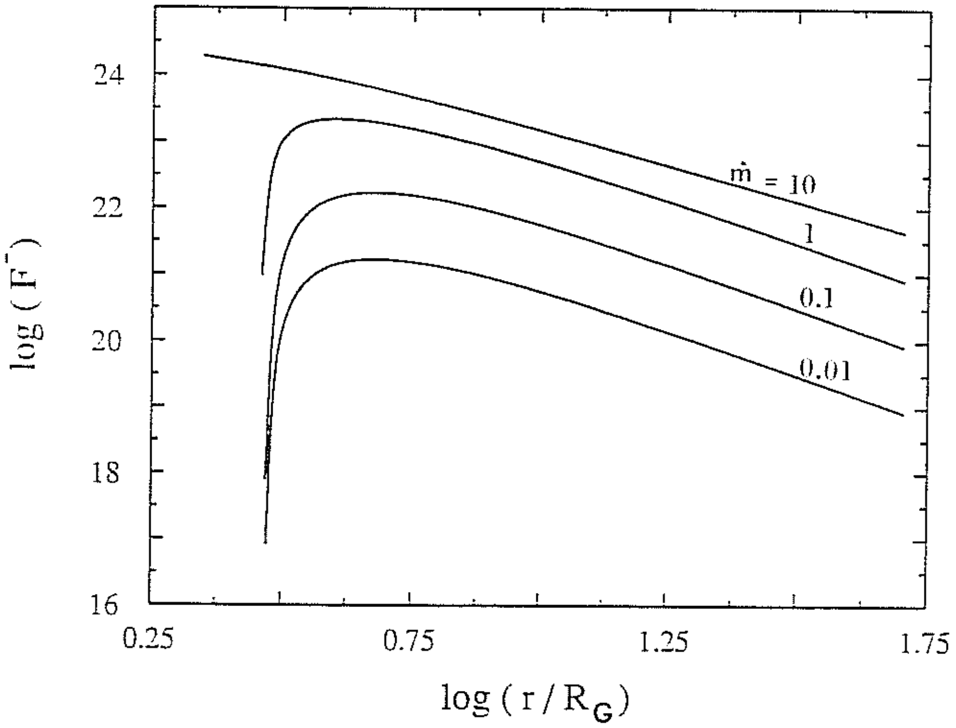

Figure 12: The radiative flux from the disk surface as a function of radius for $\dot{m} = 0.01,\ 0.1,\ 1,\ 10$.

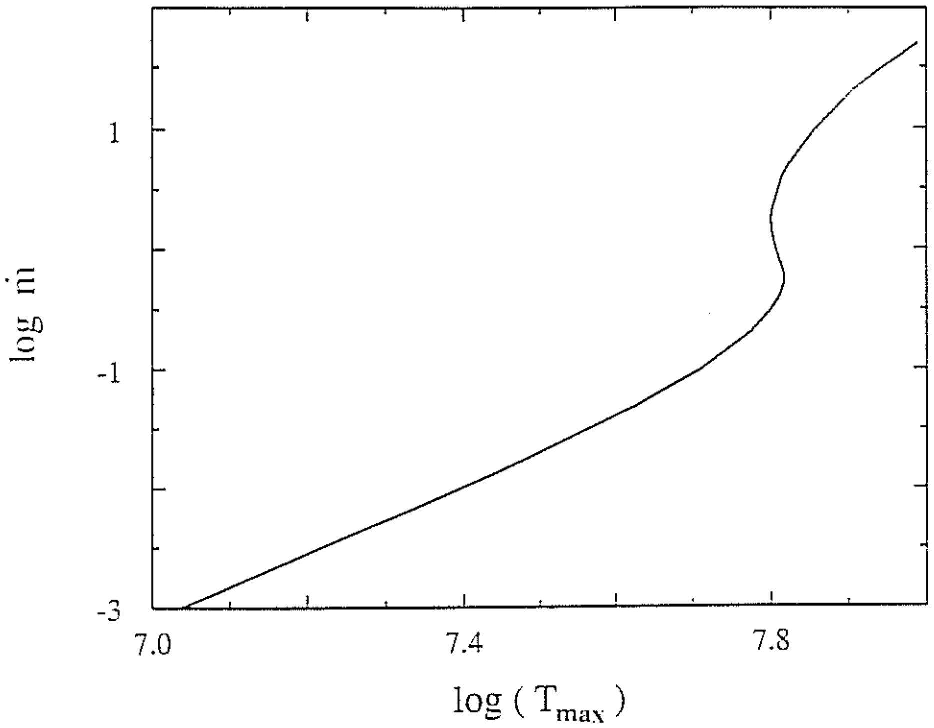

Figure 13: The accretion rate-maximum temperature relation.

of the model. The other assumptions and approximations are relevant for accuracy, but not for physics.

a) The magnitude of α in Shakura-Sunyaev viscosity prescription (2)

The fact that transonic accretion flows with small and large α are qualitatively different was noticed by Muchotrzeb (1983) and has been discussed by many authors (e.g. Matsumoto et al., 1984). In Figure 14 we show the location of the sonic point as a function of the accretion rate for $\alpha = 10^{-4}$, 5×10^{-2}, 0.1, and 0.5. For small α, equal to 10^{-4}, the typical behaviour for the thick accretion disks is evident: with increasing accretion rate the sonic point moves from R_{MS} towards R_{MB} (c.f. Paczyński 1980 and Różczka and Muchotrzeb 1982).

For the highest value of α, equal to 0.5, the sonic point moves with increasing accretion rate in the opposite direction , while for the intermediate value, $\alpha = 0.1$, the behaviour is more complicated, but for both small and large accretion rates it is similar to that for $\alpha = 0.5$. The physical reason for these two different behaviours i explained in Figure 15 which compares the Keplerian angular momentum distribution (the dotted line) with the

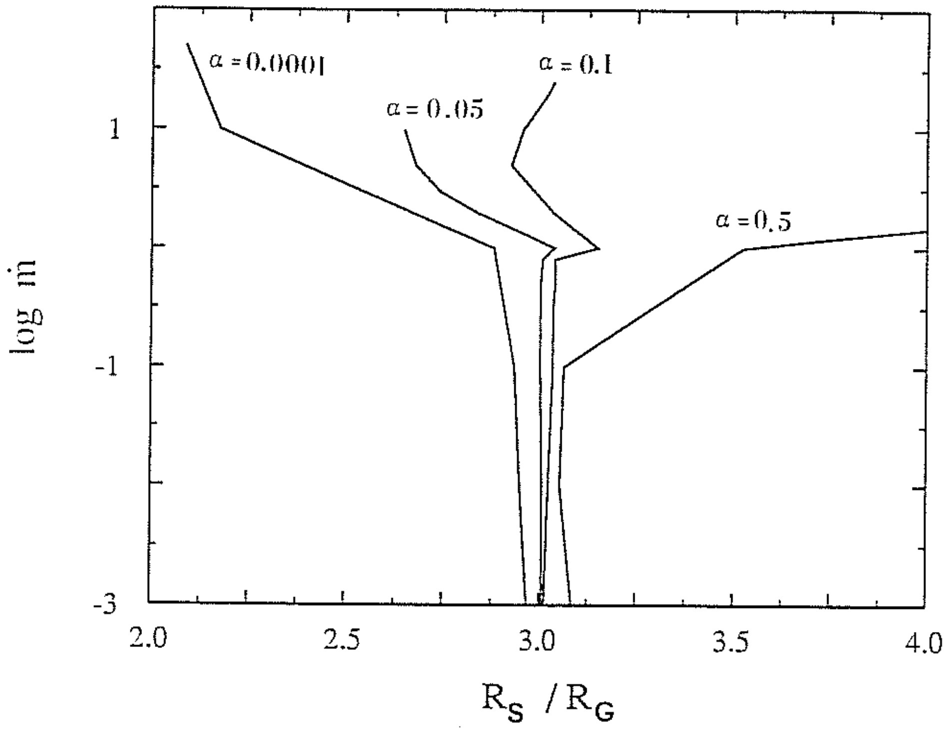

Figure 14: The location of the sonic point in function of the accretion rate for $\alpha = 10^4,\ 0.05,\ 0.1,\ 0.5$.

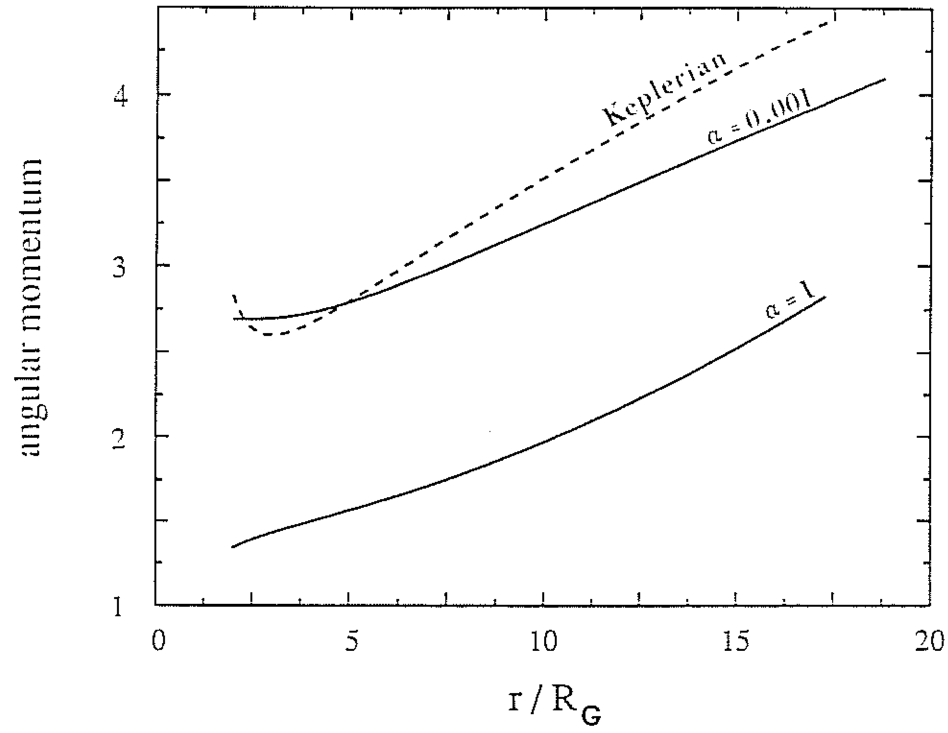

Figure 15: The comparison of the Keplerian angular momentum distribution (dashed line) with the distribution in the models with $\alpha = 0.001$ and 1 (solid lines), belonging to the two types of accretion.

distribution in two accretion disks models (the solid lines): one with small $\alpha = 0.001$ and the other with high $\alpha = 1$.

In the low viscosity case, the $l(r)$ curve crosses the Keplerian one in two points corresponding to the physical center r_c and the inner edge r_{in} of the disk (in addition $r_{in} < 3R_G$). It is well known from the thick accretion disk theory (e.g. Abramowicz, Calvani and Nobili, 1980) that in this case the Roche lobe overflow mechanism operates at $r = r_{in}$. Accretion onto the central object is due to a slight violation of mechanical equilibrium and needs no help from viscosity. In the high viscosity case the angular momentum is everywhere sub-Keplerian, the Roche lobe overflow mechanism does not operate, and accretion is due only to viscous processes. The same is true if $l(r)$ crosses the Keplerian curve, but all the crossing points are at $r > 3R_G$. Muchotrzeb-Czerny (1986) found that when the outer boundary conditions are very close to Shakura-Sunyaev ones (in the sense discussed in Section 3), then, which of the two different types of accretion actually occurs depends on whether α is greater or smaller than a critical value, $\alpha \approx 0.01$. She also found, that in the high viscosity case (the second type of accretion flow) the solution is not always unique. For this reason the lines on the right hand side of Figure 14 should really be replaced by stripes. If the magnitude of the viscosity parameter, fixed in this paper to be $\alpha = 0.001$, was increased to put the models into the second regime, the whole physical picture described here would change.

b) Different viscosity prescription

We have used the original Shakura-Sunyaev viscosity prescription (2) which assumes that the only relevant component of the viscous stress tensor, $\tau_{r\varphi}$, is proportional to the total pressure. For strictly Keplerian accretion disks this is equivalent, with accuracy up to an irrelevant constant factor, to another phenomenological viscosity prescription

$$\nu = \alpha v_s H \tag{23}$$

However, when the rotation law differs from the Keplerian one, the two viscosity prescriptions lead to physically different models. The formal reason for this is that the original Shakura-Sunyaev viscosity prescription suppress the derivative $d\Omega/dr$, in $\tau_{r\varphi}$. Thus, with the viscosity prescription given by (23) there is no more differential equation in the problem. Abramowicz and Kato (1988) found that in the case of isothermal accretion with the viscosity prescription (2), the sonic point is either of the saddle or the nodal type, while for the viscosity law given by (33) only the saddle type is allowed. The different topological types of the sonic (critical) points are connected with stability and are thus physically relevant. Another widely used variation of the original Shakura-Sunyaev viscosity law assumes that $\tau_{\varphi r} = \alpha P_g$, i.e. that the viscous stress is proportional to the gas pressure rather than total pressure. It is known that in this case the $\beta < 2/5$ instability is absent, which implies that the $\dot{M}(\Sigma)$ curves may have shapes very different from those presented here.

The viscosity coefficient α may strongly depend on the accretion rate due, for example, to the Papaloizou and Pringle (1984, 1987) instability, which for very small accretion rates may produce strong turbulence and thus viscosity, but for higher accretion rates switches off (Blaes, 1987). Assume that the viscosity coefficient depends on the accretion rate through the purely phenomenological relation

$$\alpha = \alpha_0 exp(-k\dot{M}/\dot{M}_C) \tag{24}$$

The Shakura-Sunyaev models ($k = 0$) and their modifications ($k = 0.1,\ 1$) are shown in Figure 20 Chapter 3. Although all of the above examples indicate clearly that the exact shapes of the S-curves depend strongly on the viscosity assumption, they should not be taken as a case against the generality of the existence of the S-shaped relation $\dot{M}(\Sigma)$. In the innermost part of the accretion disks around black holes (which belong to the first type of transonic accretion) this relation is due , as we have explained in Section 4, to the relativistic Roche lobe overflow mechanism and strong advective cooling connected with it. The mechanism operates independently of viscosity. Thus, the existence of the S-shaped $\dot{M}(\Sigma)$ relation does not depend on the viscosity assumption, even if the details of particular models are very sensitive to it.

c) The mass of the central black hole

Here we consider only the case $m = 10$, which is relevant to the galactic black holes. Physical processes discussed here do not depend on a particular value of m, however. The slim accretion disks around supermassive black holes, relevant for active galactic nuclei, will have the same general properties. The scaling from small to large masses is no linear and to get the quantitative description of slim disks in the case of $m > 10^6$ one must repeat the calculations presented here. The results of this calculations are presented in the next Chapter.

5.6 Conclusions

We have discussed the role of horizontal pressure and entropy gradients in accretion disks with moderate super Eddington accretion rates (slim accretion disks). We have found, that these gradients are very important in the innermost, transonic part of the disks orbiting black holes. The most astrophysically relevant effect produced is a strong horizontal heat flux, which changes the energy balance in the disk. Due to this advective flux the well known $\beta < 2/5$ instability disappears when accretion rate is high enough. For this reason the relation between accretion rate and surface density is characteristically S-shaped. The S-shaped $\dot{M}(\Sigma)$ relation in the case of accretion disks in dwarf novae plays an important role in the explanation of the outbursts (see e.g. Smak, 1984). Similar non-stationary, quasi-periodic behaviour should be expected also in the innermost, transonic part of the slim accretion disks.

5A. Schematic structure of the numerical code

From the numerical point of view, our problem is treated as a two point boundary value problem, which means that the ordinary differential equations are required to satisfy boundary conditions at more than one value of an independent variable. The "standard" two point boundary value problem has the following form: we want the solution to a set of N coupled first-order ordinary differential equations, satisfying n_1 boundary conditions at the starting point x_1 and a remaining set of $n_2 = N - n_1$ boundary conditions at the final point x_2.

One of the two classes of numerical methods for solving two point boundary value problems is the shooting method, in which we choose values for all dependent variables at one boundary. They are arranged to depend on arbitrary free parameters, whose values we initially guess "randomly". We then integrate the equations, using initial value methods,up to the other boundary. In general we find discrepancies from the desired boundary values there. Now we have a multi-dimensional root-finding problem: find the adjustment of the free parameters at the starting point that cancels the discrepancies at the other boundary point. More details about this class of methods can be found in e.g. Press, Flannery, Teukolsky and Vetterling (1986).

There are two important problems: the eigenvalue problem for differential equations and the free boundary problem, which both can be reduced to the standard boundary problem and solved using the described method.

The equations of the structure of the disk presented in this chapter are rewritten, for numerical reasons, in the following way (Muchotrzeb, 1983):

$$\frac{dlnT}{dr} = -\frac{3\kappa\rho}{16\pi B_6 c(1-\beta)Prz} F_r \tag{1}$$

$$\frac{dln\rho}{dr} = \frac{(4-3\beta)(1-U)(\frac{dlnT}{dr}) + (1-\frac{l^2}{l_K^2})\Omega_K^2 r \frac{\rho}{P} - U\frac{5r-3r_G)}{r(r-r_G)}}{U-\beta(1-U)} \tag{2}$$

$$\frac{dF_r}{dr} = \dot{M}(l - l_{in})(-\frac{d\Omega}{dr}) + \dot{M}B_1T\frac{dS}{dr} - 4\pi rF^- \tag{3}$$

where $U = \frac{1}{2}v_R^2\rho/P$. (The other quantities are defined in the previous chapters).

The input parameters are : α, m, $\dot{m}$

These input parameters are put into the program and are kept there always constant.

The outer boundary conditions result from the assumption of asymptotic Keplerian character of the solution.

The outer boundary conditions are:

$$\rho(r_{out}) = \rho_K(r_{out})$$

$$T(r_{out}) = T_K(r_{out})$$

$$F_r(r_{out}) = \tfrac{16\pi}{3}B_3\tfrac{c(1-\beta_K)P_K}{\kappa\rho_K}rz_K\tfrac{dlnT}{dr}_K$$

where the index K corresponds to the value obtained from the disk structure equation (3) and algebraic equations ((6)-(8) in Chapter 5) in the case $l = l_K$, $F_r = 0$, $B_1 = 0$. Because of the unknown parameter l_0 in equation (3) a fourth boundary condition is necessary. It is placed at the inner edge of the disk.

The free input parameter is:l_0

For a given α, m, $\dot{m}$, the free parameter, l_0 should be searched for in a such manner that a smooth transonic flow is obtained. We guess the initial value of this parameter and then we integrate inward starting from outer boundary. At the inner boundary we check the regularity condition which must be satisfied at the inner point and if necessary, we change l_0 and start the integration again. We repeat this procedure until the condition at the inner edge is satisfied. The equations are integrated from $r = r_{out} = 100r_G$. The few first steps of integration are shown in Figure 1.

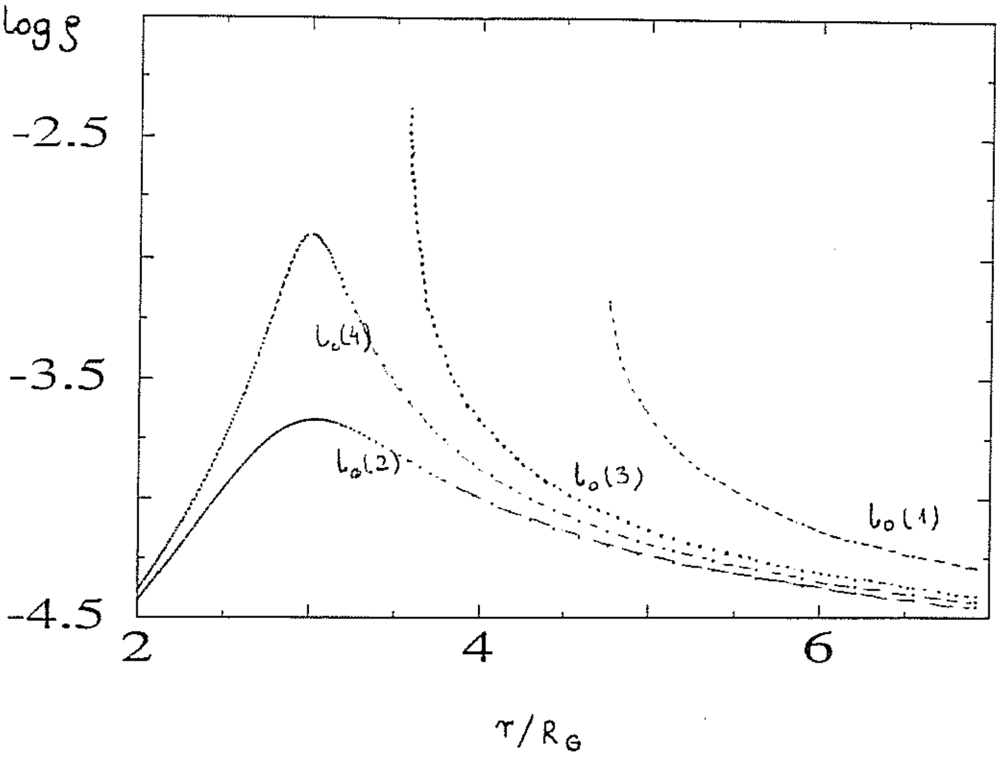

Figure 1: The integral curves for few values of free parameter l_0

For some set of runs this procedure does not converge. In the neighbourhood of a critical point the change of l_0 by a factor $\Delta l = 10^{-7}$ gives a divergence and no transonic solution is obtained. In such a case smaller step is needed. The procedure is shown in Figure 2. The two integral curves correspond to l_0 and $l_0 + \Delta l$, calculated in the first integration. They are close to the critical one but not enough to pass through the sonic point. Following integration we check the distance between them. If it reaches a small assumed value, δ,then we stop the calculation. Having stored the values of all variables in this particular point we start integration from this place taking these values as the boundary values. Now l_0 is fixed and we look for a critical solution, changing the boundary values, choosing them always in the interval between integral curves. If none of them enables passing through the sonic point, we calculate again until the transonic solution is reached.

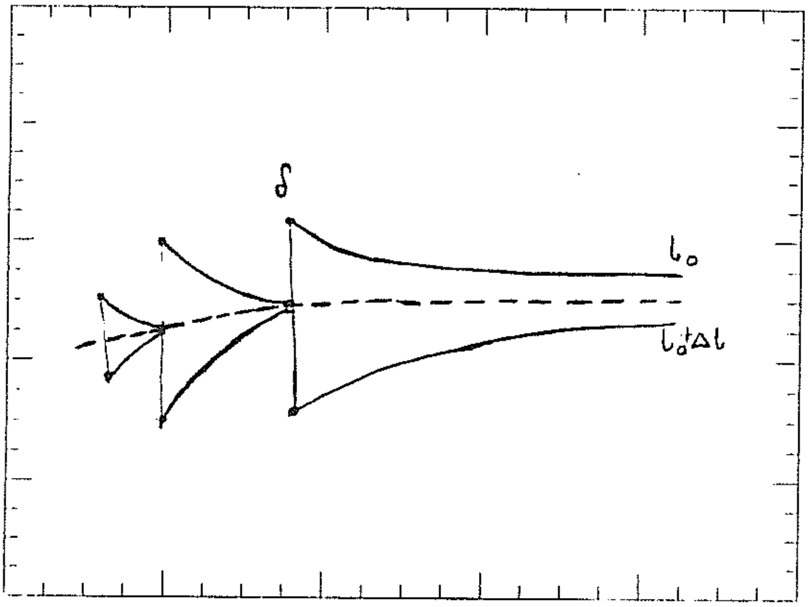

Figure 2: The finer integration scheme.

5B. A puzzle of B_i coefficients

I call this mini-chapter -a puzzle of B_i coefficients- not because they cause a problem by themselves. They appear in a particular approximation (Paczyński and Bisnovatyi-Kogan, 1981) of a two dimensional hydrodynamical flow around compact objects. They form a small and maybe not important part of the problem which, on the other hand, is extremely important and still needs to be solved. We already discussed how they were obtained. Now I would like to place them in more general picture.

We have studied stationary, axially symmetric, equatorial plane symmetric, shock-free accretion of non-self-gravitating gas onto a central object, with a mass M and a small enough radius R_0: $R_0 < 3r_G$ i.e. a black hole. We use a Newtonian model for the gravitational potential for this object. It describes the relevant general relativistic effects very accurately, as long as the central object is nonrotating or rotating slowly. Long range electromagnetic fields are assumed to be absent. We have assumed that accreted material is a mixture of a perfect gas and radiation. We treat radiation transfer inside the flow in the diffusion approximation. The optical depth is assumed to be large in both horizontal and vertical directions. The opacity coefficient is taken, as a function of density and temperature from Cox and Steward (1970). The action of viscosity is described in terms of the viscous stress tensor. Here we adopt the Shakura-Sunyaev prescription.

The above assumptions define a two-dimensional hydrodynamical problem with dissipation, differential rotation, heat transfer, radiation, and transonic motion - too complex for the existing numerical codes. The question of how to reduce it to something tractable without removing relevant physics is the question which we would like to address.

In a standard treatment, the equations describing the structure of the disk , except for the momentum equation in the vertical direction (which describes vertical hydrostatic balance), are simplified by integrating the equations over the vertical coordinate. Integration is sometimes replaced by the corresponding mean value multiplied by thickness of the disk, which gives rise to unnecessary uncertainties in the basic equations. Hoshi (1977) has introduced a concept of polytrope in the vertical distribution of accretion disk matter in order to get rid of those uncertainties.

The same approach was used by Paczyński and Bisnovatyi-Kogan (1981), who vertically integrated most of the Navier-Stokes equations and obtained a set of ordinary differential equations describing the problem.

Paczyński (1978) gives derivation of the coefficient B_4 which appears in hydrostatic equilibrium in the z direction, showing that

$$B_4 = 2(n+1)$$

where n is the polytropic index. The vertical disk structure can be approximated with a polytrope with n between 1.5 and 3. From some rather arbitrary evaluation of the polytrope index, one can get the numerical value of B_4. Having the density distribution in the z direction:

$$\rho = \rho_c(1 - \frac{z^2}{z_0^2})^n$$

where ρ_c is central density (at the equatorial plane) and z_0 is the thickness of the disk from equatorial plane to the surface, one can integrate the density, pressure, viscous stress and energy loss rate over the vertical coordinate z, and evaluate the other coefficients B_i.

Czerny (1983) studied how good this procedure of vertical integrating for the small accretion rates is. She used the fact that for small accretion rates the distribution of angular momentum is very close to the Keplerian value. The vertical structure of a Keplerian disk can be calculated in a similar way as for calculating the structure in stellar interiors. The comparison between the structure of such a disk and a disk with the vertical integrated equations gives quite good agreement, Czerny (1983).

Another way to simplify the problem is to consider a geometrically thin conical flow (Abramowicz and Zurek, 1981). They expand equations describing the structure of the adiabatic flow with respect to powers of $cos\Theta$, keeping only zeroth, first and second orders terms. The resulting set of two algebraical and five ordinary differential equations for seven unknown radial functions has a trivial analytic solution in the case of a nearly radial accretion flow, i.e. when $v_\Theta = 0(cos^3\Theta)$. This assumption of a nearly radial flow is severe. A more general case has also been considered, in which Abramowicz, Livio and Lu (1986) obtained a set of nine equations, forming a closed, self-consistent system.

However, all presented methods have their weak points and limitations. They restrict both the geometry and thermodynamics of the flow. It is necessary to treat the vertical structure of the disk in more detail using analytical or semi-analytical methods. A fully realistic model will perhaps not be obtained until a numerical code capable of dealing with all complexity.

5C. Analysis of the critical points.

Transonic accretion was discussed by Liang and Thompson (1980), Abramowicz and Zurek (1981), Loska (1982), Kato et al.,(1982), Muchotrzeb and Paczynski (1981), Muchotrzeb (1983), Matsumoto et al., (1984) and recently by Abramowicz and Kato (1988). The last paper gives us a way to treat the inner boundary conditions in the disk correctly. Differential equations describing transonic dissipative flows have critical and subcritical points (Flammang, 1982). We require our solution to pass through these points regularly. In other words, we are looking for a smooth, continuous solution with no shocks.

Abramowicz and Zurek (1982) found that in the case of dissipation-free black hole accretion, the forbidden region separates two physically different regimes. The first one, Bondi accretion, contains a solution with the sonic point far away from the hole. The second regime, disk accretion, contains a solution with the sonic point close to the hole.

Muchotrzeb (1983) studied a dissipative accretion onto black hole. She suggested the existence of an upper limit of α, above which no stationary solution is possible. Matsumoto et al. (1984) showed that unstable nodal type transonic solutions exist beyond the boundary found by Muchotrzeb. Abramowicz and Kato (1988) explained that the local regularity conditions and the global topological demands do not prevent a steady, transonic, isothermal accretion flows to exist for any value of the Shakura-Sunyaev viscosity parameter. However, these conditions cut off some forbidden regions of the parameter space in the problem. Except for isothermal flows a similar analysis for the more realistic situation is quite complicated. Matsumoto et al. (1984) concluded that the generalization (including viscous heating and radiative cooling), the qualitative nature of the critical points do not change from that in isothermal case. This statement needs deeper examination. We present results from the analysis in the case of slim disk models below.

The aim of this section is to have a better understanding of the solutions near the critical points. Such an analysis is crucial for constructing numerical methods.

5C.1 Equations

We will start from the most general form of equations (without assumption that gradient of radial flux is negligible) (Muchotrzeb, 1983). She discussed the differences between spherical accretion and disk accretion. The differences in a physical situation manifest themselves in differences in the position of the critical points. In the adiabatic approximation a critical point is described by

$$v_r^2 = \frac{2v_{ad}^2}{\Gamma_1 + 1} \tag{1}$$

where v_{ad} is the adiabatic velocity of sound and Γ_1 is the adiabatic index. In the non-adiabatic flow a critical point occurs when

$$v_r^2 = \frac{2v_T^2}{1 + \beta} \tag{2}$$

The complexity in the case of non-adiabatic flow comes from the multi-dimensionality of the problem. Here we present the equations in a form convenient for analysis. The most general case can be written as follows

$$\begin{bmatrix} 4-3\beta & \beta & x^2 & 0 & 0 \\ 12-10.5\beta & -(4-3\beta) & 0 & \frac{-y\alpha}{B_1 B_5 x} & F \\ \frac{1}{2}(4-3\beta) & \frac{1}{2}(\beta+1) & 1 & 0 & 0 \\ \frac{3}{2}(4-3\beta) & \frac{1}{2}(3\beta-1) & 0 & -\frac{B_5 x y}{\alpha} & 0 \\ 1 & 0 & 0 & 0 & 0 \end{bmatrix} \begin{bmatrix} \frac{dlnT}{dlnr} \\ \frac{dln\rho}{dlnr} \\ \frac{dlnv_r}{dlnr} \\ \frac{dln\Omega}{dlnr} \\ \frac{dlnF_r}{dlnr} \end{bmatrix} = \begin{bmatrix} y^2 - y_k^2 \\ \frac{B_3 c(1-\beta) y_k^2}{B_4 B_1 B_5 \kappa v_* \rho r x} \\ \frac{dln\Omega_k}{dlnr} - 1 \\ 2(\frac{B_5 x y}{\alpha} - 1) \\ \frac{dlnT}{dlnr} \end{bmatrix}$$

where $F = \frac{B_6 c(1-\beta) G}{B_1 B_5 \kappa \rho x v_* r}$. Further new definitions are:

$x = v_r/v_s$ (the ratio of the radial velocity to the sound velocity), where $v_s = (P/\rho)^{1/2}$,

$y = v_\varphi/v_s$ (the ratio of the azimuthal velocity to the sound velocity),

y_k is the same as y but for the Keplerian motion, i.e. $\Omega = \Omega_k$. r is given in units of r_G. The Keplerian angular velocity is given by:

$$(\sqrt{\frac{GM}{r_g^3}})\frac{r^{-1/2}}{r-1}$$

and its logarithmic derivative by:

$$\frac{dln\Omega_k}{dlnr} = -\frac{1}{2} - \frac{r}{r-1}$$

If we neglect the term dF_r/dr in the energy balance equation the set reduces to

$$\begin{bmatrix} 4-3\beta & \beta & x^2 & 0 \\ 12-10.5\beta & -(4-3\beta) & 0 & \frac{-y\alpha}{B_1 B_5 x} \\ \frac{1}{2}(4-3\beta) & \frac{1}{2}(\beta+1) & 1 & 0 \\ \frac{3}{2}(4-3\beta) & \frac{1}{2}(3\beta-1) & 0 & -\frac{B_5 xy}{\alpha} \end{bmatrix} \begin{bmatrix} \frac{dlnT}{dlnr} \\ \frac{dln\rho}{dlnr} \\ \frac{dlnv_r}{dlnr} \\ \frac{dln\Omega}{dlnr} \end{bmatrix} = \begin{bmatrix} y^2 - y_k^2 \\ \frac{B_3 c(1-\beta) y_k^2}{B_4 B_1 B_5 \kappa v_* \rho r x} \\ \frac{dln\Omega_k}{dlnr} - 1 \\ 2(\frac{B_5 xy}{\alpha} - 1) \end{bmatrix}$$

5C.2 The standard approach

Equations of the stationary disk structure in the slim disk approximation are written in the form:

$$\mathbf{A}_{ij}\frac{dQ_j}{dr} = \mathbf{B}_i$$

It can be treated as a classical dynamical system where the evolution occurs not in time but in space. We can apply standard methods to find and describe the characteristics of the critical points. First we rewrite these equations in the form of a standard dynamical system as

$$\frac{dQ_j}{dr} = \frac{F_j}{F}$$

It is convenient to perform a coordinate transformation $r \rightarrow \tau$ where

$$\frac{d\tau}{dr} = \frac{1}{F}$$

and write the system in the form

$$\frac{dQ_j}{d\tau} = F_j(Q_1, ..., Q_n).$$

In that way we remove the singularity from the system. To keep track of our problem, instead of going away into all details of the theory, we get the meaning of Q_j as follows:

$$Q_1 = lnT$$
$$Q_2 = ln\rho$$
$$Q_3 = lnv_r$$
$$Q_4 = ln\Omega$$
$$Q_5 = lnF_r$$
$$Q_6 = lnr$$

It should be stressed here that only three independent differential equation exist in the problem. We used five because of some convenience in algebraical manipulations. It will be necessary to compress that form, leaving the x, y, and r as the parameters of the flow.

A point $(Q_1^o, ..., Q_n^o)$ is called a critical point of the dynamical system if

$$F_j(Q_1^o, ..., Q_n^o) = 0 \qquad (3)$$

for all j. The problem of finding all critical points of the system and the corresponding solutions is thus reduced to the problem of solving a system of algebraic equations (3).

5C.3 Location of critical points in the slim disk

From the method described previously we obtained the six following equations

$$\frac{dlnr}{dln\tau} = \frac{B_5 xyF}{\alpha}(\frac{1}{2}(\beta+1)x^2 - \beta) \qquad (4)$$

This equation gives the necessary condition for existence of the critical points. They appear if $x^2 = 2\beta/(\beta+1)$, which is in agreement with relation (2) found by Muchotrzeb (1983). In that case $v_T = \beta P/\rho$.

$$\frac{dlnT}{dln\tau} = G\frac{B_5 xyF}{\alpha}(\frac{1}{2}(\beta+1)x^2 - \beta) \qquad (5)$$

where we have chosen G to be the logarithmic derivative of the temperature. For this reason the formula (5) is very similar to the previous one.

$$\frac{dln\rho}{dln\tau} = \frac{B_5xyF}{\alpha}(-(y^2 - y_K^2) + x^2(\frac{dln\Omega_K}{dlnr} - 1) - G(4 - 3\beta)(\frac{1}{2}x^2 - 1)) \quad (6)$$

The new condition describing critical solution follows from this equation .

The term in brackets should be equal to 0.

$$\frac{dlnv_r}{dln\tau} = \frac{B_5xyF(\beta + 1)}{2\alpha}((y^2 - y_K^2) - \frac{2\beta}{\beta + 1}(\frac{dln\Omega_K}{dlnr} - 1) - G\frac{4 - 3\beta}{\beta + 1}) \quad (7)$$

For the regularity of the solution the same condition as in (6) should be satisfied.

$$\frac{dln\Omega}{dln\tau} = F(2(\frac{B_5xy}{\alpha} - 1)(\beta - \frac{1}{2}(\beta + 1)x^2) -$$
$$\frac{1}{2}(3\beta - 1)((y^2 - y_K^2) - x^2(\frac{dln\Omega_K}{dlnr} - 1)) + G(4 - 3\beta)(x^2 - \frac{1}{2})) \quad (8)$$

Also this equation gives the same condition. The last equation does not give us any additional conditions. Right hand side of the relation is equal zero when $dlnr/dln\tau = 0$.

$$\begin{aligned} &\frac{dlnF_r}{dln\tau} = \\ &\frac{y\alpha}{B_1B_5x}((2(\frac{B_5xy}{\alpha} - 1)(\beta - \frac{1}{2}(\beta + 1)x^2) - \\ &\frac{1}{2}(3\beta - 1)((y^2 - y_K^2) - x^2(\frac{dln\Omega_K}{dlnr} - 1)) + \\ &\frac{B_5xy}{\alpha}(\frac{B_3c(1 - \beta)y_k^2}{B_4B_1B_5\kappa v_s\rho rx}(\frac{1}{2}(\beta + 1)x^2 - \beta) - \\ &(4 - 3\beta)((y^2 - y_K^2) - x^2(\frac{dln\Omega_K}{dlnr} - 1)) \\ &+G\frac{y\alpha(4 - 3\beta)}{B_1B_5x}(x^2 - \frac{1}{2})) - \frac{B_5xy}{\alpha}G(-f_\beta + \frac{1}{2}x^2f_{\beta+1}) \end{aligned} \quad (9)$$

where

$$f_\beta = (4-3\beta)^2 + \beta(12-10.5\beta) \tag{10}$$

$$f_{\beta+1} = (4-3\beta)^2 + (\beta+1)(12-10.5\beta) \tag{11}$$

To summarize this very technical discussion we can say that the critical point appear when

$$x^2 = \frac{2\beta}{\beta+1} \tag{12}$$

and

$$(y^2 - y_K^2) - \frac{2\beta}{\beta+1}(\frac{dln\Omega_K}{dlnr} - 1) = G\frac{4-3\beta}{\beta+1} \tag{13}$$

It can be noticed that this result is similar to that obtained by Abramowicz and Kato (1988). The left hand side is equal zero instead of $G(4-3\beta)/(\beta+1)$. In fact this term is vanishing in the isothermal case because $G = dlnT/dlnr$.

The simplified case, without dF/dr in the energy balance equation is actually even more complicated. The procedure is equally easy but the expressions describing the critical solutions are quite complex. The first equation we would like to consider is

$$det(\mathbf{A}_{ij}) = F_6 = \frac{d\tau}{dlnr} = 0.$$

which leads to the fourth order algebraical equation:

$$\begin{gathered} x^4[\tfrac{1}{2}\tfrac{B_5}{\alpha}((\beta+1)(12-10.5\beta)+(4-3\beta)^2)] - \\ x^2[(4-3\beta)\tfrac{\alpha}{B_1B_5} + \tfrac{B_5}{\alpha}((4-3\beta)^2+\beta(12-10.5\beta))] + \\ \tfrac{1}{2}(4-3\beta)\tfrac{\alpha}{B_1B_5} = 0 \end{gathered} \tag{14}$$

It is easy to show that this equation has always (for all values β) four different, real solutions. Two of them are positive and are two negative and located symmetrically on both sides of x=0. Physically we are interested only in the two positive ones. x depends explicitly only on β and α. Introducing the function g

$$g(\beta,\alpha) = (4-3\beta)\frac{\alpha^2}{B_1B_5} + B_5 f_\beta \tag{15}$$

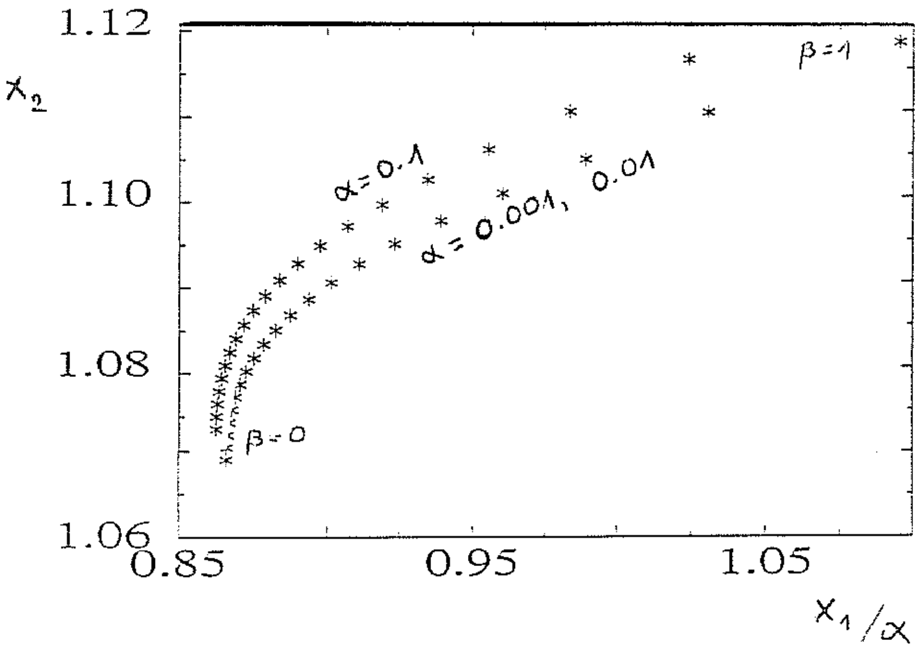

Figure 1: Critical solutions for $\beta \approx 1$

then it is possible to write the solutions in the form

$$x_1^2 = \frac{g(\beta,\alpha) - \sqrt{g^2(\beta,\alpha) - \frac{\alpha^2 f_{\beta+1}(4-3\beta)}{B_1}}}{B_5 f_{\beta+1}} \tag{16}$$

$$x_2^2 = \frac{g(\beta,\alpha) + \sqrt{g^2(\beta,\alpha) - \frac{\alpha^2 f_{\beta+1}(4-3\beta)}{B_1}}}{B_5 f_{\beta+1}} \tag{17}$$

The exact solutions for different values of parameter α and for all β's are illustrated on the Figure 1. The first solution corresponds to the sonic point, but the second one is also connected with α, that is with angular momentum transport. These two points are the candidates for the critical ones. Careful analysis is needed to extract the physical one. We noticed that two cases are important: one with the gas pressure dominance ($\beta \approx 1$), the other with the radiation pressure dominance ($\beta \approx 0$). The intermediate situation is very rare (Figure 2).

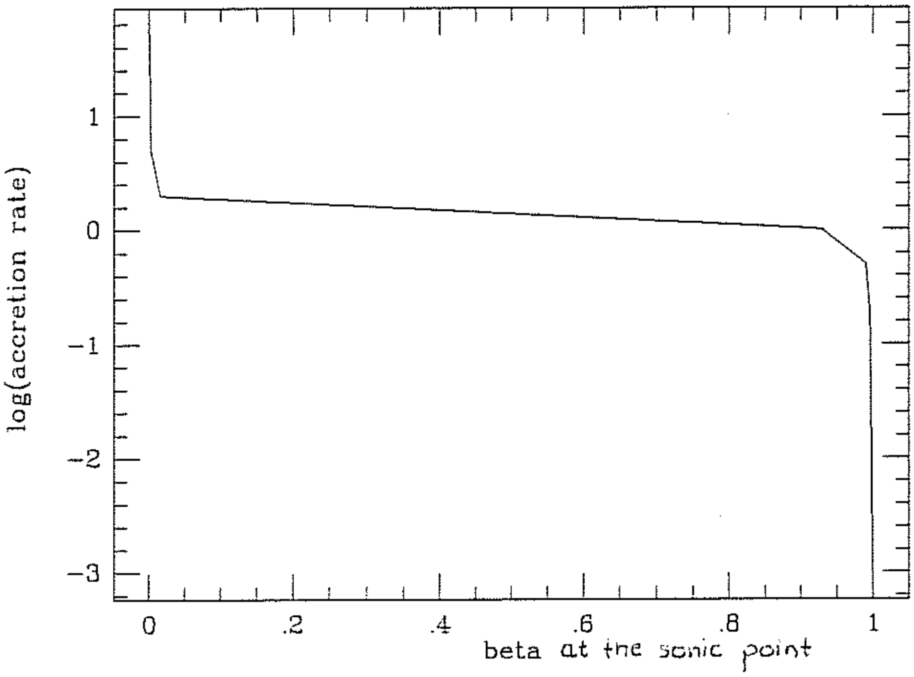

Figure 2: The $\dot{m}(\beta)$ relation in the inner part of the disk

a) $\beta \approx 1$

This assumption is correct for small accretion rates in the inner part of the disk. In this case the solutions of the equation (14) is a function of α only

$$x_{1,2}^2 = \frac{3\alpha^2 + \frac{5}{4} \pm \sqrt{9\alpha^4 + \frac{3}{2}\alpha^2 + \frac{25}{16}}}{2} \tag{18}$$

For small α these two solutions give

$$x_1^2 = \alpha, \quad x_2^2 = \frac{5}{4}.$$

The dependence on viscosity can have some reasonable influence only when $\alpha \approx 1$. For this reason, we first consider the zero order approximation, assuming that viscosity is negligible and then we will discuss the general case.

From the condition that all numerators should at the same time be equal to zero we get

$$y^2 - y_K^2 = \frac{5}{4}(\frac{dln\Omega_K}{dlnr} - 1) \tag{19}$$

and

$$x^2 = \frac{5}{4} \tag{20}$$

This relation is analogous to that given by Abramowicz and Zurek (1981) for non-dissipative accretion. The same conclusion is easily reached: the angular momentum at the sonic point is smaller than the Keplerian value. Going back to the equations of the disk structure we can estimate the physical conditions at the sonic point, expressing them for example in terms of the temperature in this point. Thus

$$(v_r)_s^2 = \frac{5}{4}\frac{k}{\mu H}T_s \tag{21}$$

$$z_s = (B_4\frac{k}{\mu H}T_s)^{1/2}\Omega_K^{-1} \tag{22}$$

$$\rho_s = \frac{\dot{M}\Omega_K}{4\pi B_5 B_4^{1/2}(\frac{5}{4})^{1/2} r_s \frac{k}{\mu H}T_s} \tag{23}$$

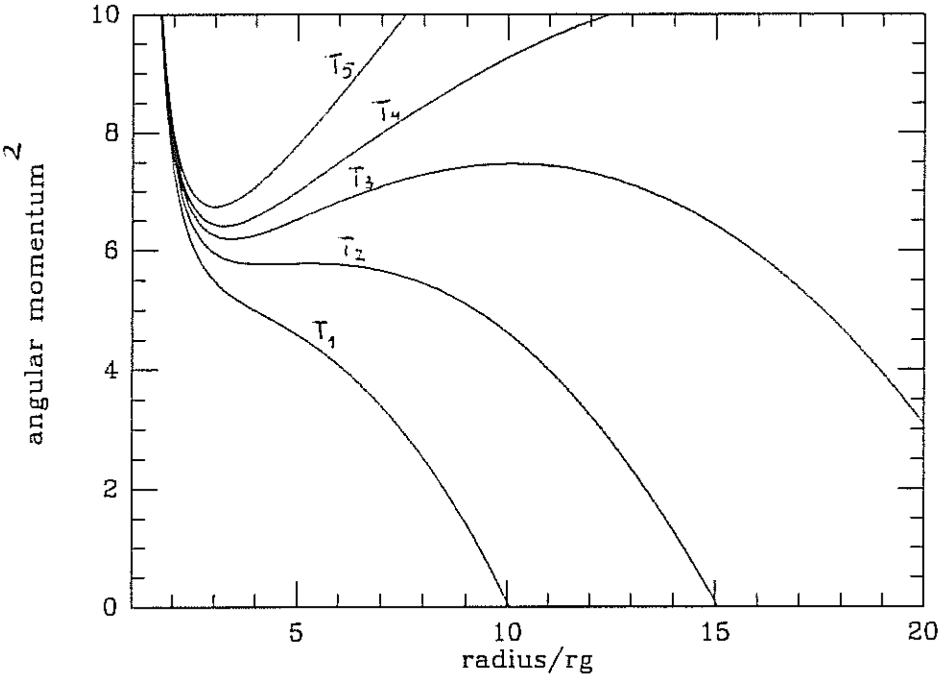

Figure 3: The square of angular momentum as the function of the critical point location

The angular momentum as a function of the position of the sonic point is shown in Figure 3. The temperature at the sonic point is chosen as a parameter.

The general case (for any value of viscosity) should be qualitatively the same. The necessary and sufficient conditions for a critical points give the relation identical to (19) with the difference that now x^2 is one of the general solutions and

$$y^2 - y_K^2 = \frac{5B_5^2 x^2 B_1(4x^2 - 5) + 2\alpha^2 x^2 + 5\alpha^2}{4B_5^2 x^2 B_1(4x^2 - 5) - 8\alpha^2 x^2 + 16\alpha^2}\left(\frac{dln\Omega_K}{dlnr} - 1\right) \qquad (24)$$

b) $\beta \approx 0$

For high accretion rates, $\dot{m} > 1$, the disk is almost completely dominated by radiation . As we can see from Figure 2, $\beta \approx 0$ is an excellent approximation in the inner part of the disk.

The nondissipative ($\alpha \approx 0$) case is analogous to the situation where gas pressure is dominant. The solutions of the equation (14) are

$$x_{1,2}^2 = \frac{2(3\alpha^2) \pm \sqrt{36\alpha^4 + 6\alpha^2 + 16}}{7} \qquad (25)$$

For the viscosity it reads

$$x_1 = \alpha, \quad x_2 = \frac{8}{7} \qquad (26)$$

Our analysis of the type of the critical points is extremely difficult, because of the multi-dimensionality of the problem. The result of this analysis will be given in a forthcoming paper.

6. Slim disks around supermassive black holes

6.1 How big are supermassive black holes?

a) Starting at the beginning (The birth of a supermassive black hole).

Rees (1978), Begelman and Rees (1978), and Rees (1984) have sketched possible routes by which a supermassive black hole may be born via a run-away evolution in an active galactic nucleus. They found a standard mass of $\approx 10^8 M_\odot$. Recently, Kochanek, Shapiro, and Teukolsky (1987) presented a simple way of estimating the size of a supermassive black hole formed during the collapse of an unstable spherical star cluster. Their black holes have masses in the range: $10^6 < M/M_\odot < 10^9$.

b) Emission lines as a mass indicator.

The method is based on the assumption that the rotation of the gas in the neighbourhood of the nucleus is compensated by the gravitational attraction of the central body. This was originally due to Woltjer (1959). The expression for the mass has the form $M \approx v^2 r/G$, where v is the velocity distribution of the clouds at the gravitational center, r is a size of the region where the lines are formed (Broad Line Region, BLR), G is the gravitational constant. Gas velocities have been determined from emission lines in the spectra of galactic nuclei by various authors (e.g. Dibai, 1984, Wandel and Yahil, 1985). They used the half-intensity level of the line profile to measure the gas velocity. The next problem is to evaluate the characteristic size, r, of the BLR. This quantity can be derived from two parameters: the electron density of the gas and the geometry, (the volume filling factor). Dibai (1980) gives the values of the central mass for 37 Seyfert 1 galaxies and 12 nearby quasars. All masses are in the range $10^6 - 10^9 M_\odot$. Wandel's (1986) mass-luminosity relation is shown in Figure 1. $10^8 - 10^9 M_\odot$ is a common range for both Seyferts and quasars. $10^6 - 10^8 M_\odot$ is the Seyfert domain and the region $10^9 - 10^{10} M_\odot$ is mainly populated by quasars.

Joly et al. (1985) pointed out one of the problems with such an

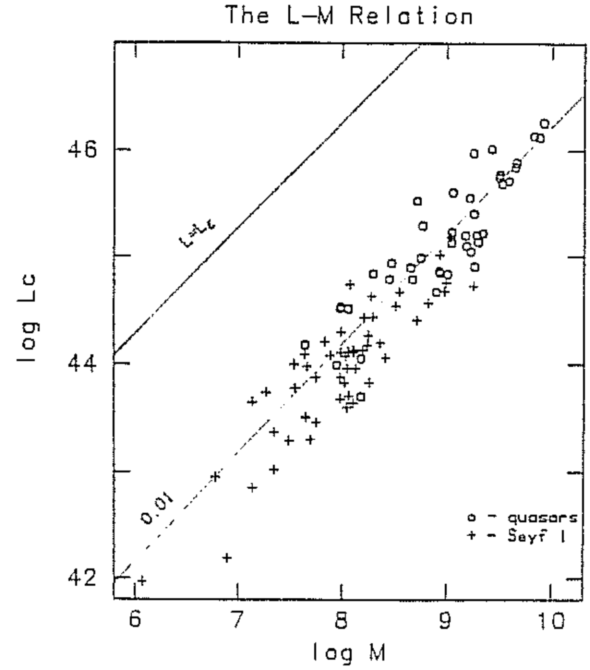

Figure 1: The optical luminosity versus the dynamical (H_β) mass. Crosses mark Seyfert 1 nuclei, while quasars are denoted by circles (Wandel, 1986)

approach for high luminosity quasars, namely the masses involved in the model should be as high as $10^{11}M_\odot$ for $L_0 \approx 10^{47} erg\ s^{-1}$.

Burbridge and Perry 1976 evaluated the central mass by analysis of the interaction between emission line clouds. They found masses between 5×10^7 and $2 \times 10^9 M_\odot$.

The mass of NGC 1566 (Alloin et al 1985), derived from BLR line widths (2000 km/s) and size of BLR (3×10^{16} cm), is about $5 \times 10^6 M_\odot$. Alloin et al.(1988) made a quantitative analysis of the Balmer and C IV line profiles in Akn 120 and found that the broad line region comprise two distinct regions. One of them is an accretion disk with size equal to a few couple of light months, with inclination $i \leq 60^0$, and with the mass of the central black holes $M \geq 7 \times 10^7 M_\odot$. Peacock (1987) obtained for NGC 4151 the mass $5 \times 10^8 - 10^9 M_\odot$. Clavel 1988 derived for the Fairall 9 mass $M = 2 \times 10^8 M_\odot$.

c) Direct estimation from the bolometric luminosity

Estimating the bolometric luminosity of observed quasars and converting this into energy radiated per bright galaxy one is able to deduce the mass of the source. (Soltan 1982 and Phinney 1983). The infalling matter is accumulated in the black hole during the lifetime of the quasar. Soltan

(1982) used this fact to estimate the total mass of the black hole, due to accretion:

$$m = c^{-2}\kappa^{-1}LT$$

L is the luminosity, T the lifetime of the quasar, and κ the efficiency of energy conversion. Only L is known for an individual object. Using quasar counts he calculated the total energy emitted by all quasars in a unit volume and found limits for the total mass of the black hole ($10^8 - 10^9 M_\odot$). It is comparable with upper limits on reported measurements of central mass of galaxies as our own, M31, M87, (Kormedy, 1987). In the case of the largest radio galaxies, the energies in the radio lobes can exceed $10^6 M_\odot c^2$. Adopting an efficiency of 10% this translates into a minimum mass of $10^7 M_\odot$ for the central black hole. The most powerful quasars in the universe require central black hole masses in excess of $3 \times 10^9 M_\odot$, if they radiate at the Eddington limit.

d) Evolution arguments

In the simplest quantitative model for evolution (Blandford, 1986) black holes grow continually from modest initial masses $\approx 100 M_\odot$, with an e-folding time $\approx 10^8$ yr, until the rate of gas supply is insufficient to allow them to grow further. Black holes which are formed early in the Universe are able to grow to masses $\approx 10^9 - 10^{10} M_\odot$ in $\approx 10^9$ yr, and correspond to the brightest high-redshift quasars . They also become the most energetic radio sources after accretion was stopped. Black holes that start to grow somewhat later are only able to achieve masses $\approx 10^8 - 10^9 M_\odot$. They also cease forming at $z \approx 2$ and constitute the majority of the quasars. The last galaxies to form are only able to grow central black holes to masses $\approx 10^6 - 10^7 M_\odot$. These are now actively accreting for about 1-10% of the time and are now called Seyfert galaxies.

d) Gravitational lenses

The gravitational effect was tested on a close pair of quasars, 1548+115 a, b (Paczynski 1974, Gott and Gunn 1974). Lack of the appreciable imagining of the more distant pair member by the nearer one provided an upper limit of $4 - 7 \times 10^{12} M_\odot$ for 1548+115a.

e) Masses from the variability timescales

It is often held that the x-ray emission from active galactic nuclei arises from a region close to the central energy source. Thus x-ray ob-

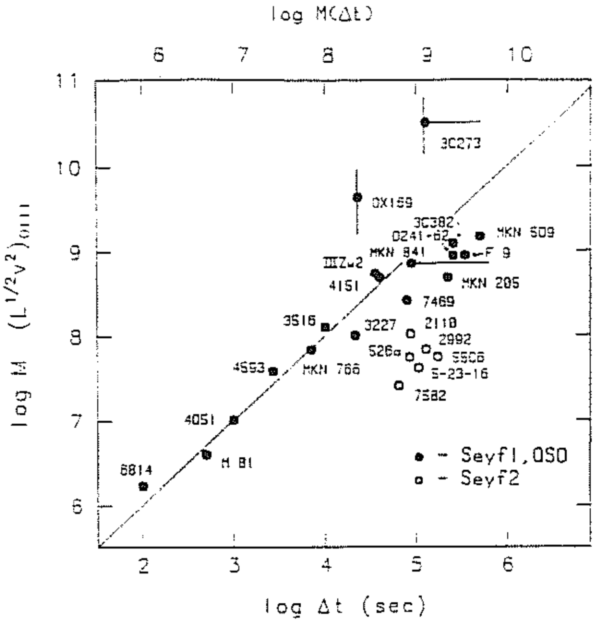

Figure 2: The dynamical mass versus time variability (Wandel and Mushotsky 1986)

servations may provide the best constraints on the central engine. X-ray time variability data can constrain the size and the mass of the continuum source. Assuming that the shortest observed timescales of the variability is equal to dynamical timescale, $t_d \approx 2\pi/\Omega_K$, where $\Omega_K \approx (GM/r^3)^{1/2}$, one can get the mass of the central source. Wandel and Mushotsky (1986) give the dynamical mass - variability time relation for Seyferts and Quasars. It is shown in Figure 2. Pounds and Turner (1987) derived a mass $\approx 1.5\times10^6 M_\odot$ for III Zw 2, from the dynamical timescale of $\approx$ 1500 s.

f) Masses derived from the UV continuum.

Malkan (1983) analyzed the ultraviolet spectra of six quasars. The continua are fitted with spectra predicted for optically thick, steady- state accretion disks, which include the effects of general relativity. The two fitting parameters, the mass of the accreting black hole and accretion rate, are determined by data having accuracy of 20% . The masses range from 2-5 $\times10^8$ for 3C 273 and PKS 0405-123 to 1-3$\times10^9 M_\odot$, for the high redshift quasars. The simplest accretion disk models have difficulties explaining the optical- UV-soft x-ray big bump in quasars. Czerny and Elvis (1987) found that opacity effects can explain the uniform 20,000-30,000 K "maximum disk temperature". The observed spectral turn off would be the result of electron scattering and should not be identified with the hottest part of the disk. The frequency at which this spectral turn off occurs is depending only weakly on the accretion disk parameters. These opacity effects also allow high- frequency EUV and soft x-ray extension of the big bump, without exceeding the Eddington limit by much . They have applied the disk spectrum model to interpret the optical-UV-soft x-ray big bump in the quasar PG 1211+143 (Bechtold et al., 1987). Constraints on the mass of the black hole and the accretion rate gave the values $5 \times 10^7 M_\odot$ and $\approx 5 M_\odot/\mathrm{yr}$, respectively, so luminosity of the disk is only about factor 3 higher than Eddington value.

6.2 Constraints on viscosity in accretion disks.

The optical, UV and soft x-ray continua can be modelled as thermal emission from an accretion disk. The predicted thermal timescales for variability depend strongly on the assumed viscosity parameter. Comparing with the observed timescales one can constrain the values of viscosity. Czerny and Czerny (1986) found that the rather large values of the viscosity parameter is more likely. Their results are presented in Figure 3. In a recent paper Siemiginowska and Czerny (1988) considered the same problem using numerical methods. They concluded that the viscosity parameter in accretion disks in AGN is required to be smaller than 0.1 but greater than 0.01.

6.3 Slim disk models around supermassive black holes

Taking into account all arguments for estimating the mass and viscosity in accretion disks in AGN a possible range of parameters has been chosen to calculate slim disk models (Abramowicz, Czerny, Lasota and Szuszkiewicz 1988).Our parameter space is $(\alpha, \dot{M}, M)$, where $10^6 M_\odot \leq M \leq 10^9 M_\odot$, $10^{-7} \leq \alpha \leq 10^0$, and $\dot{M}$ is constrained by the existence of the transonic solution for the slim model. The upper and middle branches of the resulting S-curve do not depend on the mass of the accreting black hole. This result is a consequence of the thin disk properties in the case of radiation pressure dominance (equation (40), Chapter 3) and nature of the stabilizing mechanism (equation (57), Chapter 3). The comparison between models with $M = 10^6$ and $10^8 M_\odot$ is shown in Figure 4. The agreement between numerical and analytical solutions is even stronger comparing masses for galactic black holes ($(10 M_\odot$ (see Figure 5). In Figure 6 we represented the sequence of S-curves for M $= 10^8 M_\odot$ for different viscosity parameters

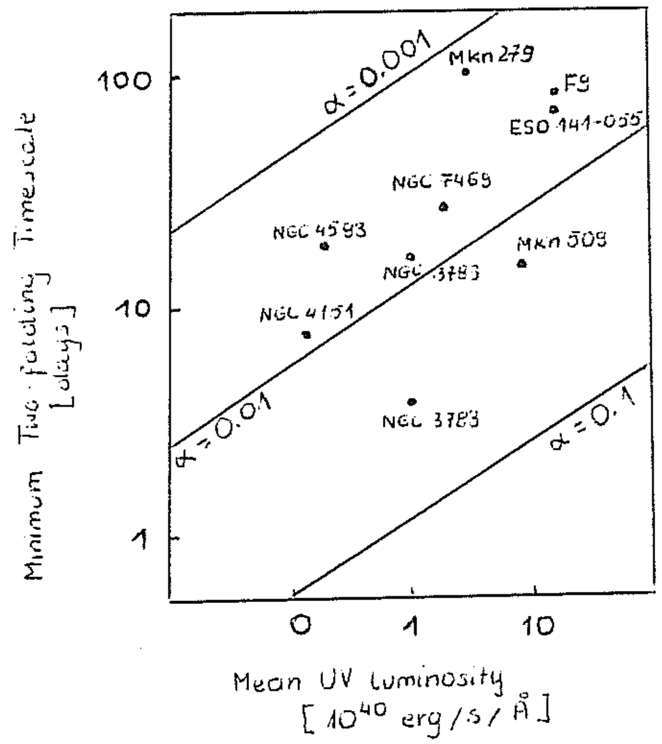

Figure 3: The ultraviolet luminosity as a function of the variability timescale

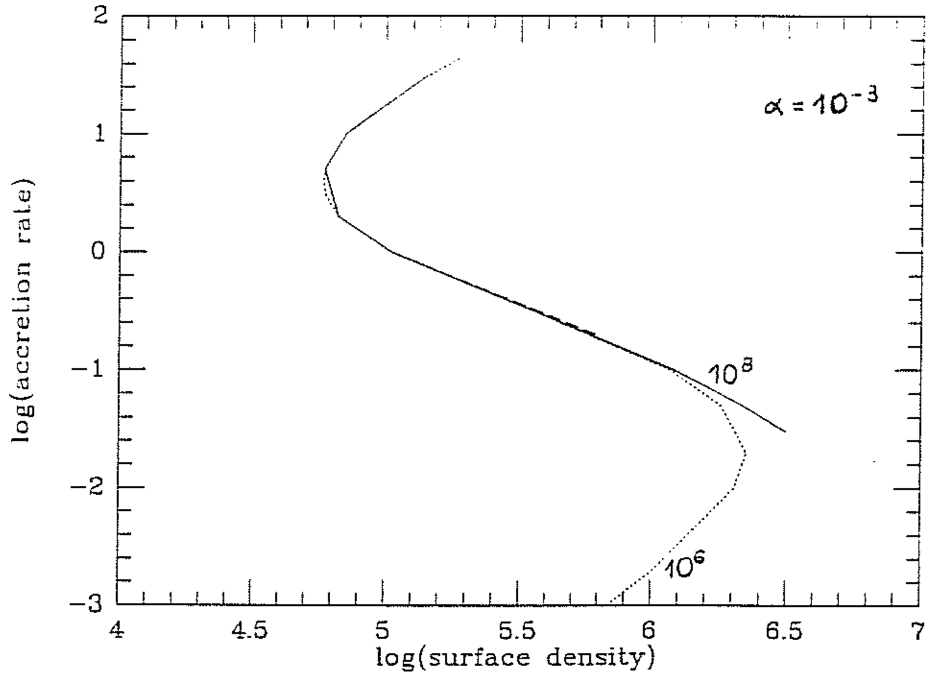

Figure 4: The $\dot{m}(\Sigma)$ relation for $m = 10^6$ and 10^8.

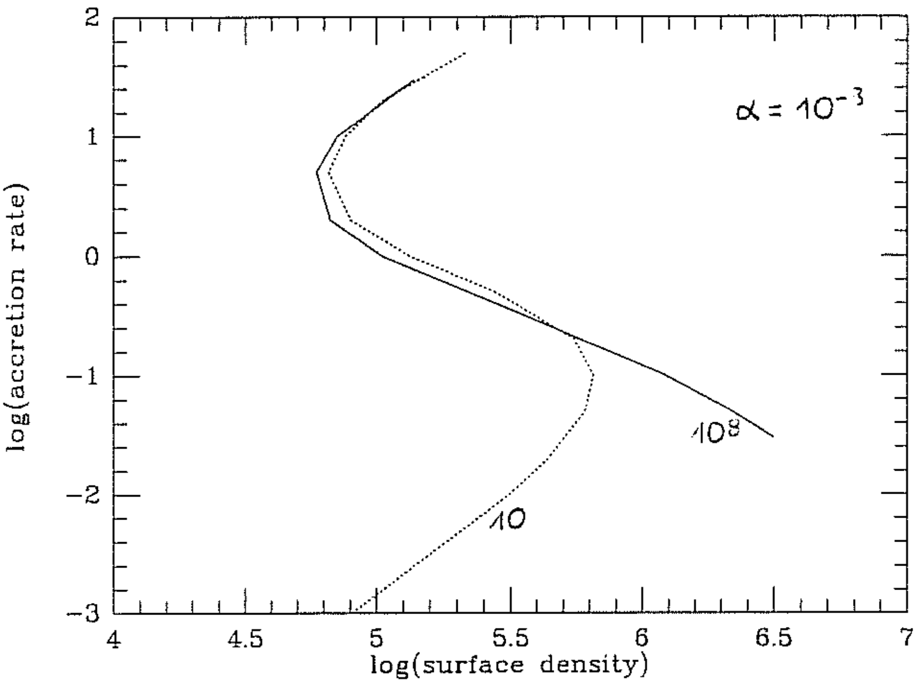

Figure 5: The $\dot{m}(\Sigma)$ relation for $m = 10$ and 10^8.

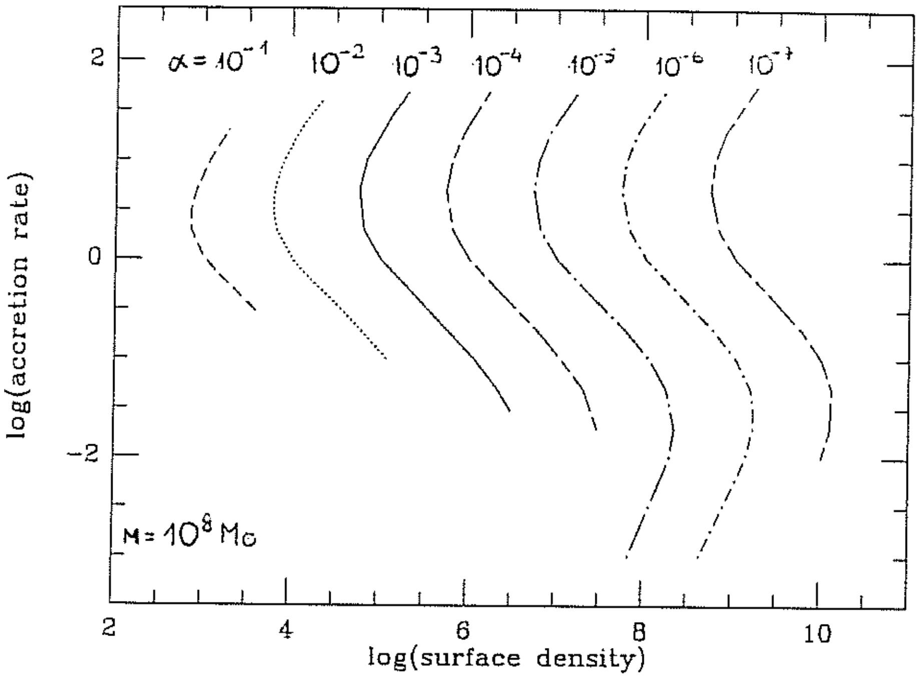

Figure 6: The S-curve relations for the different viscosity parameter

starting from $\alpha = 1$ and going up down 10^{-7}. The lower turning points correspond to $\beta = 2/5$. S-curves for $\alpha \geq 10^{-3}$ are not completed. We cannot obtain the self-consistent transonic models in this case. these accretion rates.

We present here in some detail the structure of the slim disk models with high accretion rate (Figures 7, 8 and 9). The thickness of the disk increases with increasing accretion rate until $\dot{M} = 50\dot{M}_{crit}$ but the shape does not change qualitatively. The model for $50\dot{M}_{crit}$ gets characteristic form of the thick disk. Sonic point position is changing in the range: from close to $3r_g$ for small accretion rates to close to $2r_g$ for the high accretion rates.

A different mode of accretion appeared in the sequence of models for M=$10^8 M_\odot$ and viscosity $10^{-7} - 10^{-5}$ for accretion rates as high as 57 and 58 $\dot{M}_{crit}$. There is no continuous change between modes in the range 56 and 57 $\dot{M}_{crit}$,t since the location of the sonic point jumps to distances about 90

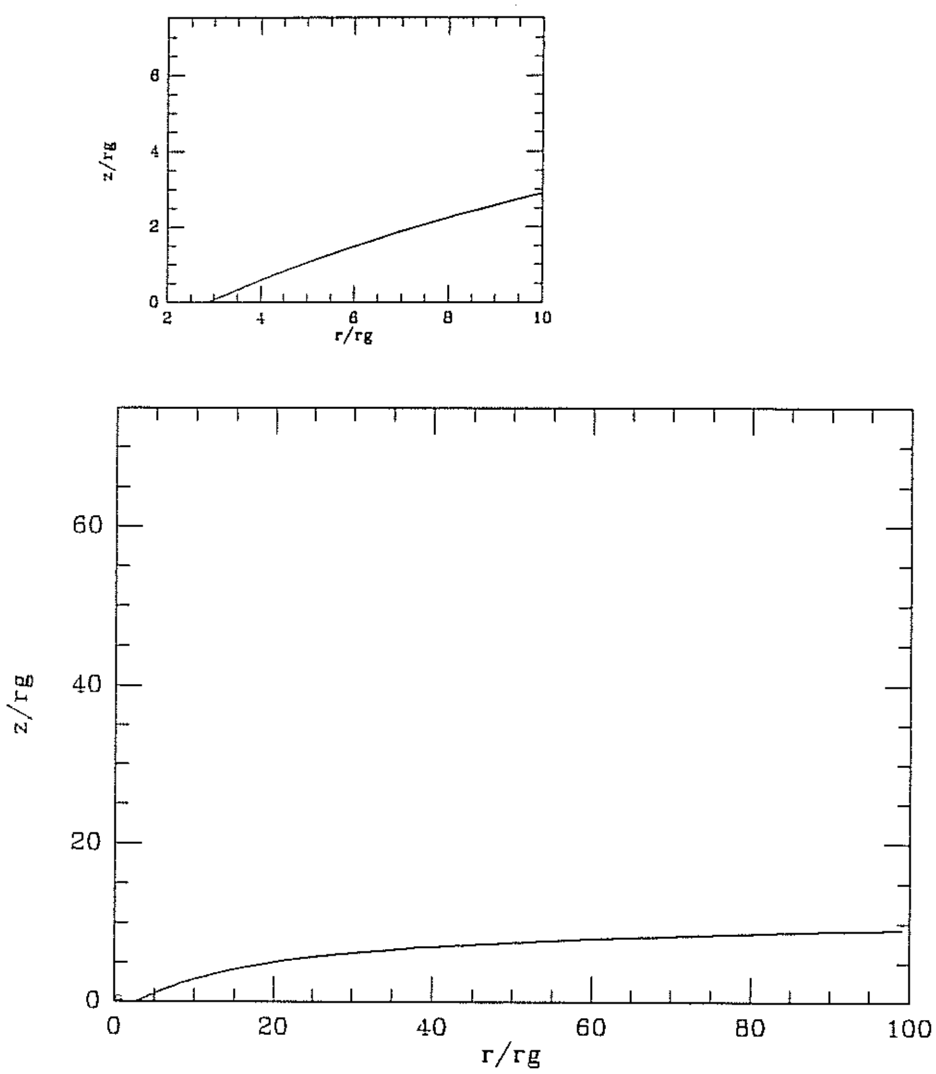

Figure 7: The structure of the slim disk with $\alpha = 10^{-6}$, $m = 10^8$, $\dot{m} = 1$

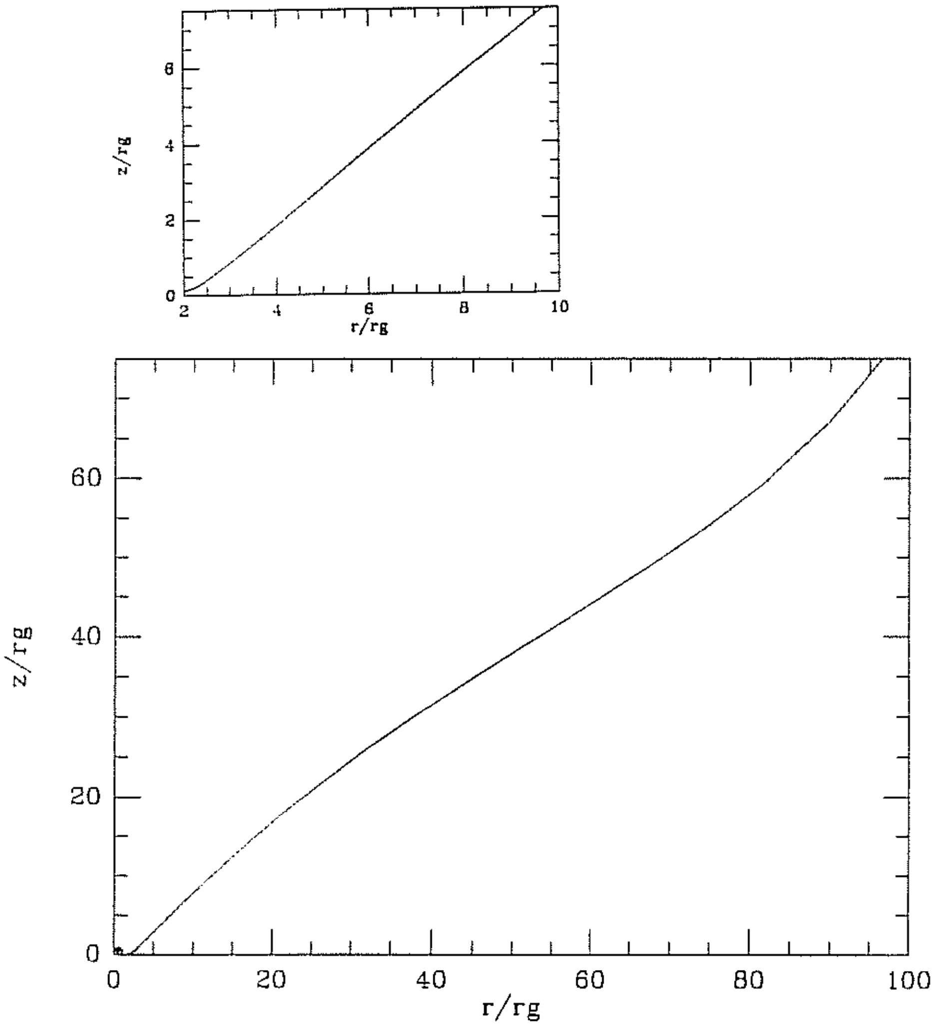

Figure 8: The structure of the slim disk with $\alpha = 10^{-6}$, $m = 10^{8}$, $\dot{m} = 10$

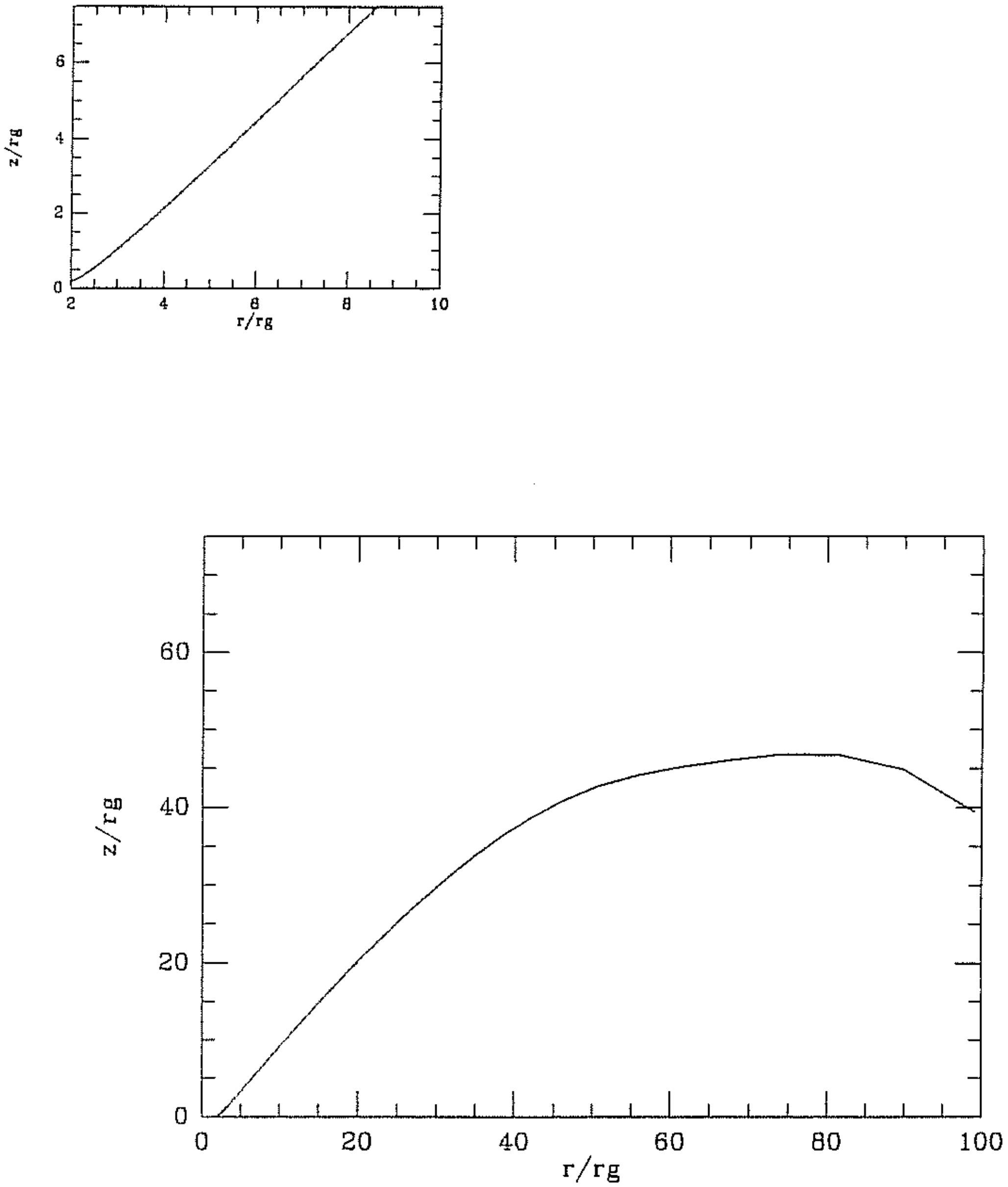

Figure 9: The structure of the slim disk with $\alpha = 10^{-6}$, $m = 10^8$, $\dot{m} = 50$

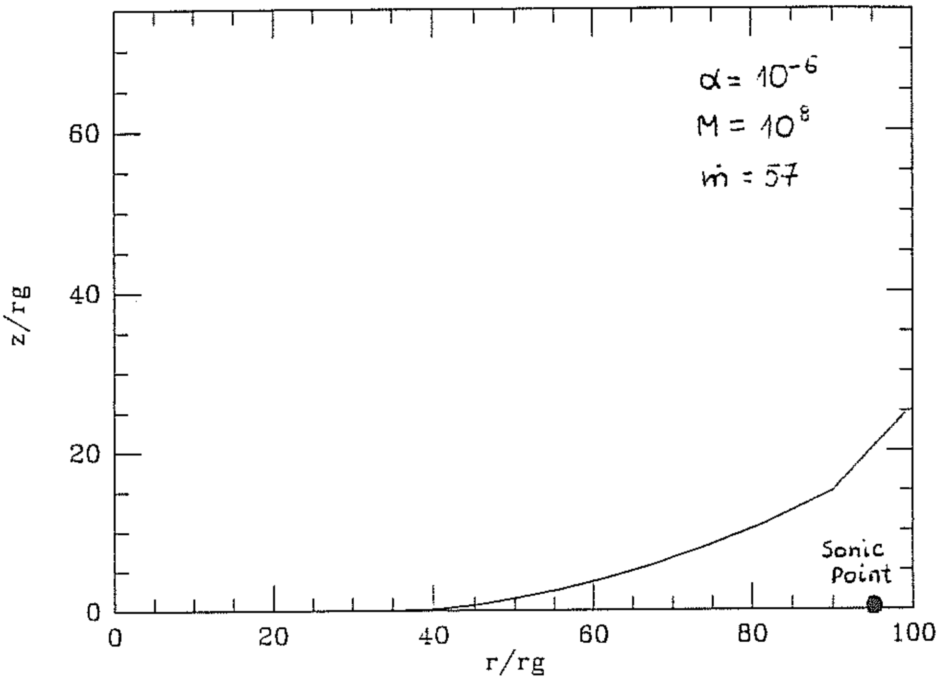

Figure 10: The shape of an accretion flow for $\alpha = 10^{-6}$, $m = 10^8$, $\dot{m} = 57$

r_g from the black hole. The angular momentum is constant. This could be the second mode of accretion suggested by Abramowicz and Zurek (1981). The shape of the accretion flow is shown in the Figure 10.

We assume in our models that the flow is optically thick. The temperature distribution proves that it is a good approximation in the region we considered. The surface and equatorial temperatures shown in Figure 11 are different from each other about one order of magnitude.

6.4 Shape of the optical - UV - soft x-ray continuum.

There are some general trends in the evolution of spectra in AGN. Some of them can be explained using a sequence of equilibrium models of the accretion disk . The spectra for three values of viscosity are presented in Figures 12, 13 and 14.

We calculated also the spectrum for the second mode of accretion, with the sonic point located at big distances. The flux from such disks

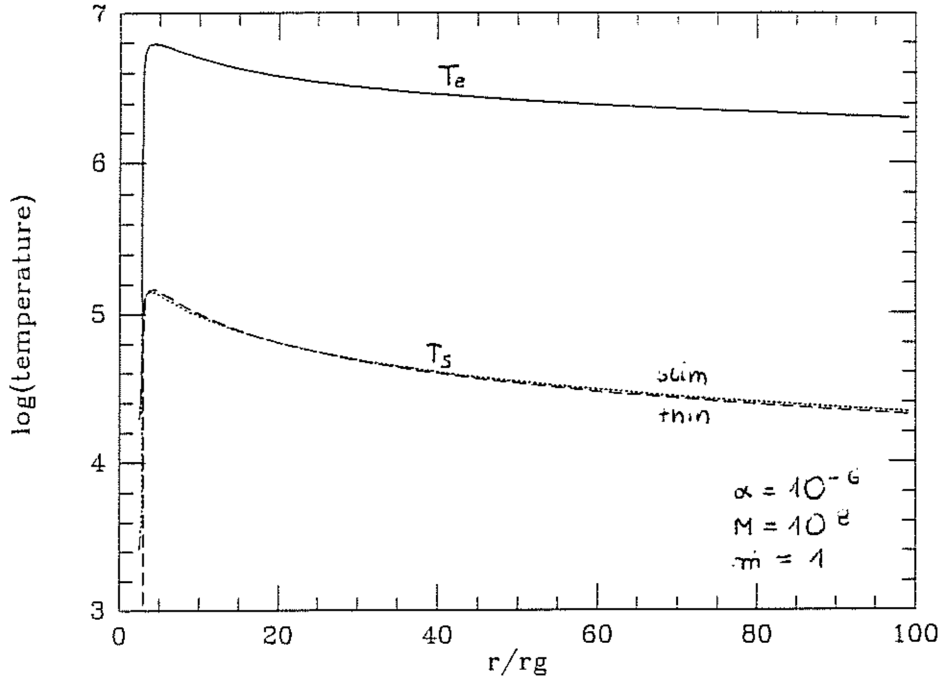

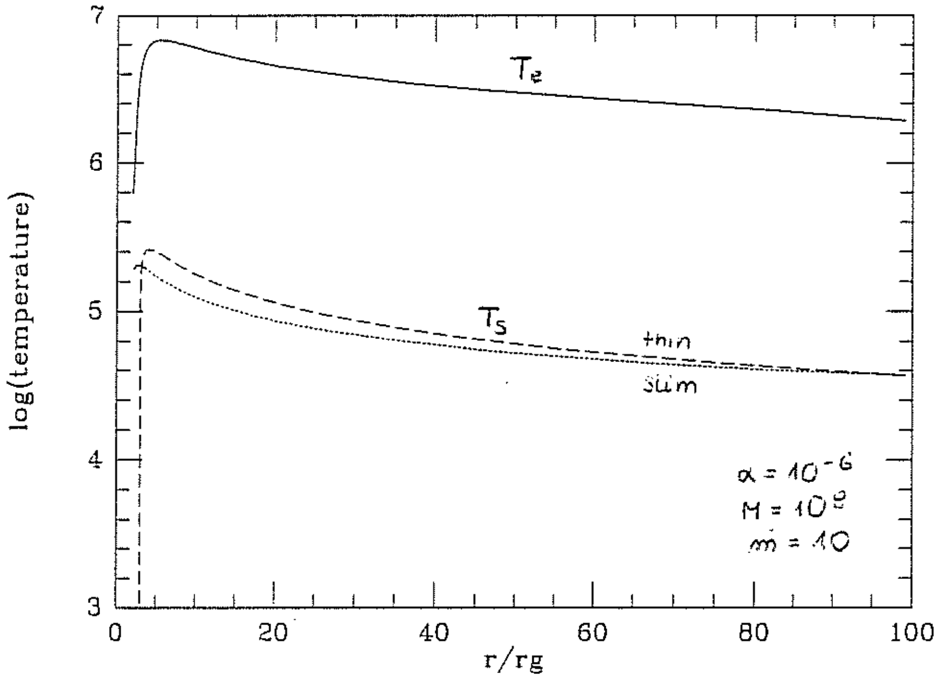

Figure 11: The surface and equatorial temperature for $\alpha = 10^{-6}$, $m = 10^8$ and $\dot{m} = 1, 10$.

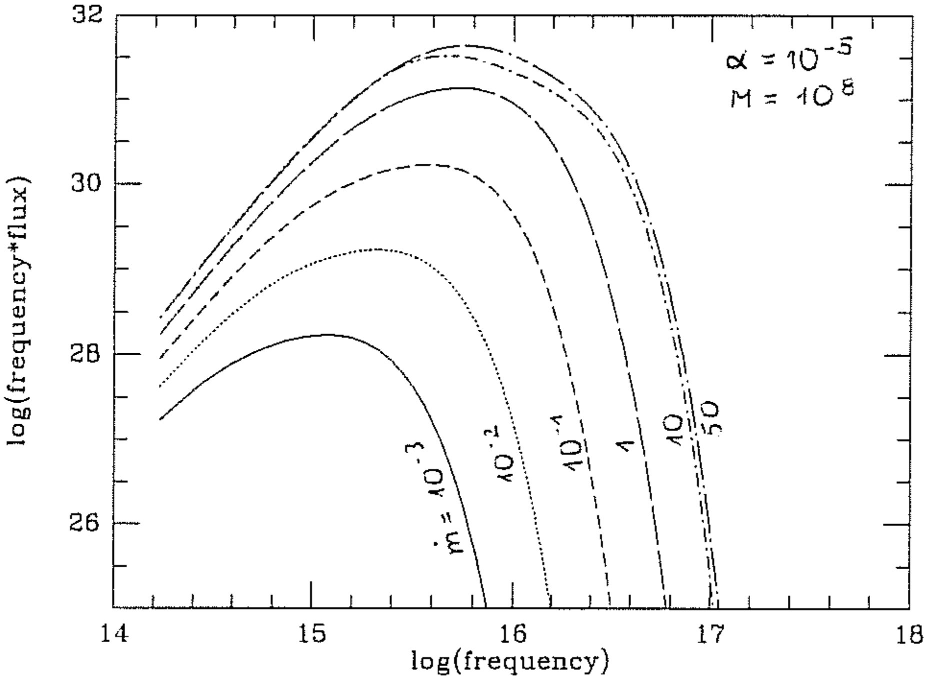

Figure 12: The spectral shapes for a sequence of models with $\alpha = 10^{-5}$ and $M = 10^{8}$.

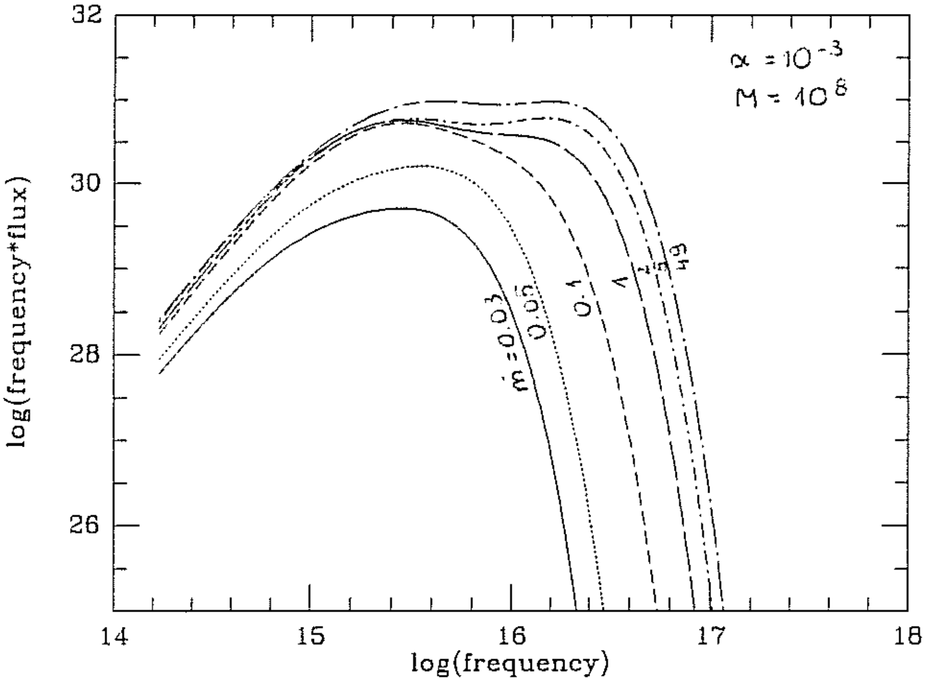

Figure 13: The spectral shapes for a sequence of models with $\alpha = 10^{-3}$ and $M = 10^{8}$.

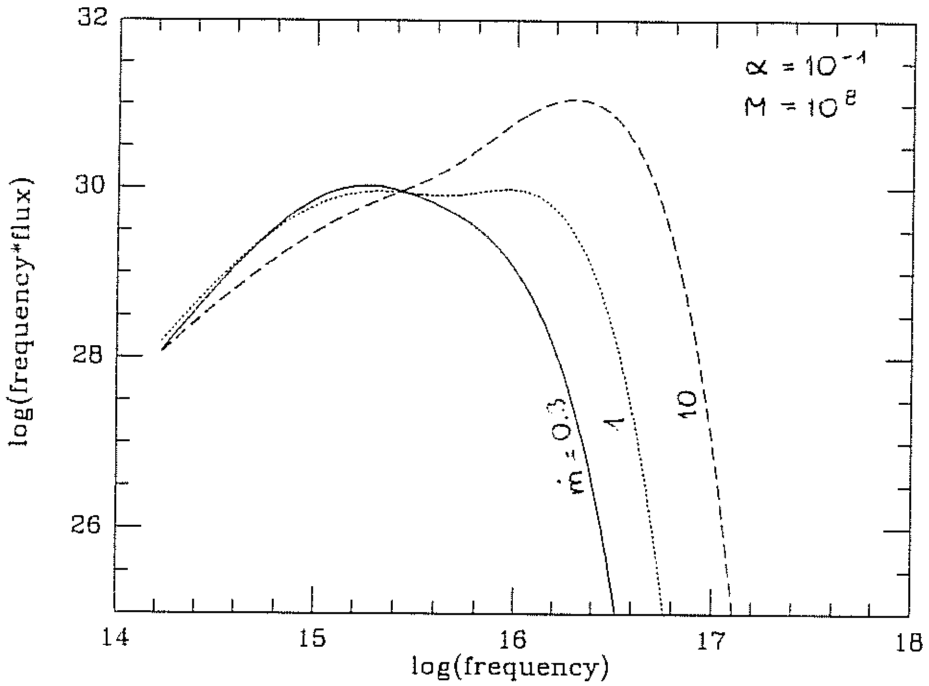

Figure 14: The spectral shapes for a sequence of models with $\alpha = 10^{-1}$ and $M = 10^8$.

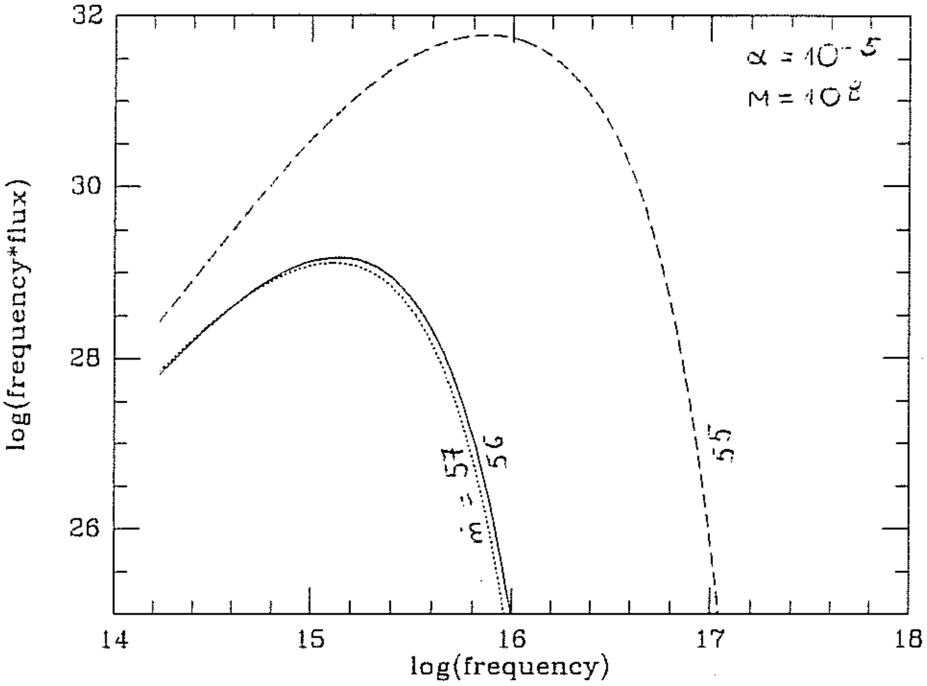

Figure 15: The shape of the slim disk spectra for $\alpha = 10^{-5}$ and $m = 10^8$, for different accretion rates.

is small in comparison with the first mode, and tends to decrease with increasing accretion rate (Figure 15).

6.5 Top Ten List of AGN

I will discuss some of the spectral properties following the variability of the best studied objects in terms of the position on our theoretical tracks.

NUMBER ONE - FAIRALL 9

Without any doubt the number one is Fairall 9, because of the high quality data of simultaneous optical and UV spectral observations. The source is classified as a Seyfert 1. But at the time of its discovery it was so bright that it was thought to represent the overlap between QSO's and Seyfert I galaxies (Danks et al, 1979). The UV continuum showed dramatic variations, its intensity decreasing by a factor of 30 in terms of bolometric

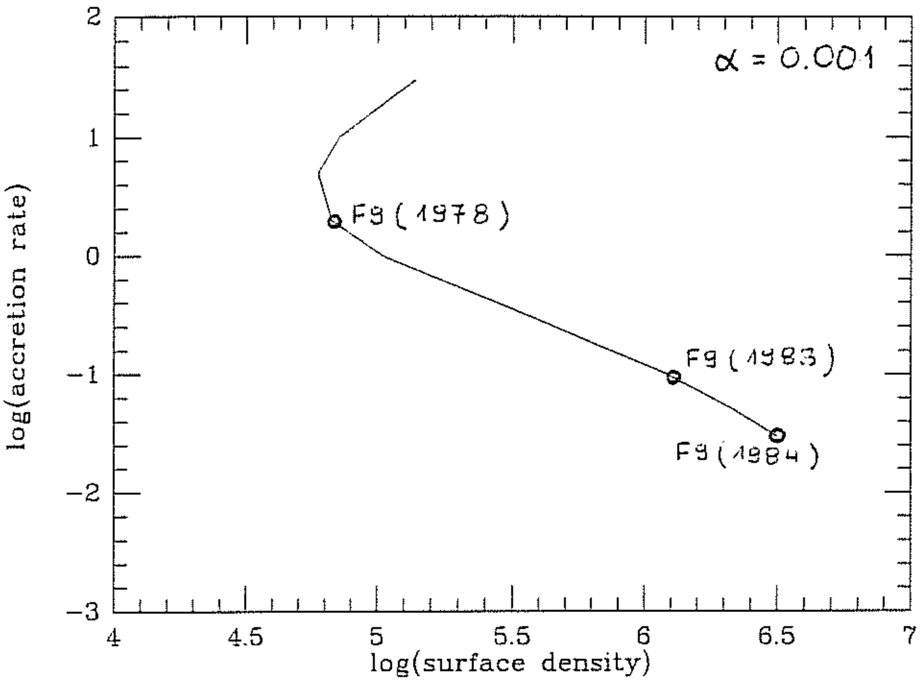

Figure 16: Fairall 9 at the equilibrium sequence

luminosity, from a maximum in 1978 to a deep minimum in mid-1984. The near IR and optical fluxes changed by a factor ≈ 3. Its position on the equilibrium sequence is shown in Figure 17. The high state accretion rate as derived by Clavel et al 1988. The low state is found from the relative changes in intensity. The intermediate state in October 1983 was obtained in the same way. The energy distribution from the disk is shown in the Figure 16 for this particular models. An interesting thing is that quantitative changes of spectral index from these spectra can reproduce the observed one. Morini et al (1986) gave the value of spectral index in the UV for the two periods (October 1983 and October 1984) as 0.40 ±0.11 and 0.86 ±0.11. Our accretion disk models for $M=10^8 M_\odot$ and viscosity 0.001 have the same UV slope, i.e. 0.39 and 0.86, for accretion rates 0.03 and 0.1 $\dot{M}$ respectively. The difference in flux between these models is as the observed one - factor 0.4 in logarithm (table 4 in Morini et al , 1986).

NUMBER TWO - NGC 1566

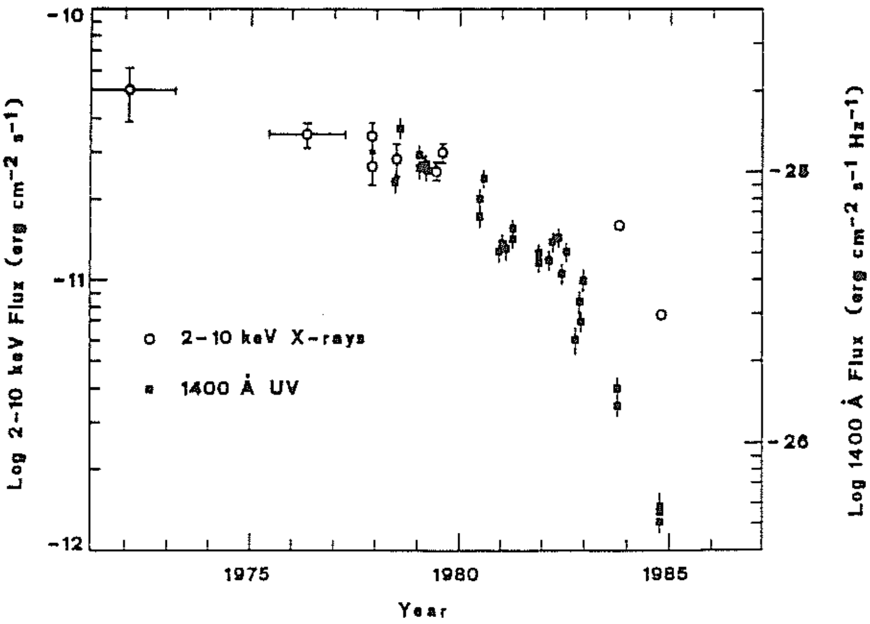

Figure 17: The 2-10 keV and 1400 A fluxes of F9 as a function of time in the period 1970-1984.

The schematic light curve of NGC 1655 is shown in Figure 18. The observed variability of the broad emission lines H_α and H_β is interpreted as a variability of the accretion rate in the accretion disk orbiting the black hole in the center of NGC 1655 (Abramowicz, Lasota and Xu, 1986). The shaded areas are equal. This defines both the characteristic accretion rate $\dot{M}_0 = 3 \times 10^{-1} \dot{M}_E$ and the two timescales of 900 and 400 days. The two regimes occur along the rising branch: first a mild increase on a timescale of 310 days followed by a steep rise on a timescale less than 20 days. The decreasing part of the bursts corresponds to an exponential decay between 390 and 475 days. The three successive sub-bursts observed in the last cycle are separated by 310 days.

Abramowicz, Alloin, Lasota and Pelat (unpublished) have suggested an explanation for this variability: a limit cycle which works due to thermal and viscous instabilities present in the innermost region of an accretion disk orbiting a black hole.

NUMBER THREE - PG 1211+143

Quasar PG 1211+143 has an unusual spectrum. The x-ray spectrum

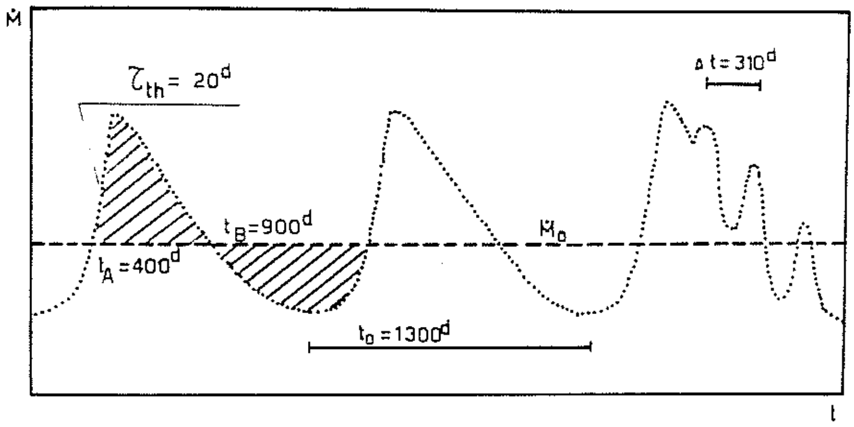

Figure 18: The light curve of NGC 1655 (Abramowicz, Lasota and Xu, 1986)

of this object is very steep, with the best-fit power law $F_E \propto E^{-\alpha_E}$ yielding a spectral index $\alpha_E = 2.2 \pm 0.4$ (Bechtold et al. 1987). One possible explanation for the steepness of these spectra is that we are seeing the soft x-ray excess arising at the hot inner edge of an accretion disk. Czerny and Elvis (1987) have applied the model of disk spectrum to interpret the optical/UV/x-ray big bump in PG 1211+143. The accretion disk in this quasar must be face-on ($cosi > 0.7$), in order to account for the observed soft x-ray excess. Constraints on the mass of the black hole and accretion rate gave the value $\approx 5 \times 10^7 M_\odot$ and $\approx 5M_\odot/year$ respectively, i.e., the luminosity of the disk is only about a factor 3 higher than the Eddington luminosity. Fit to the data for PG 1211+143 by an accretion disk is shown in Figure 19.

NUMBER FOUR - Akn 120

Akn 120 was subsequently reported to vary both in the continuum and in the broad line emission (Lyutij, 1979; Kollatschny et al, 1981; Schulz and Rafanelli, 1981; Peterson et al., 1985). Variability properties offer us a unique opportunity to find the size of the region producing the emission lines and to test the existence of disc accreting massive black holes. For any frequency, light from the surface of the accretion disk should show the

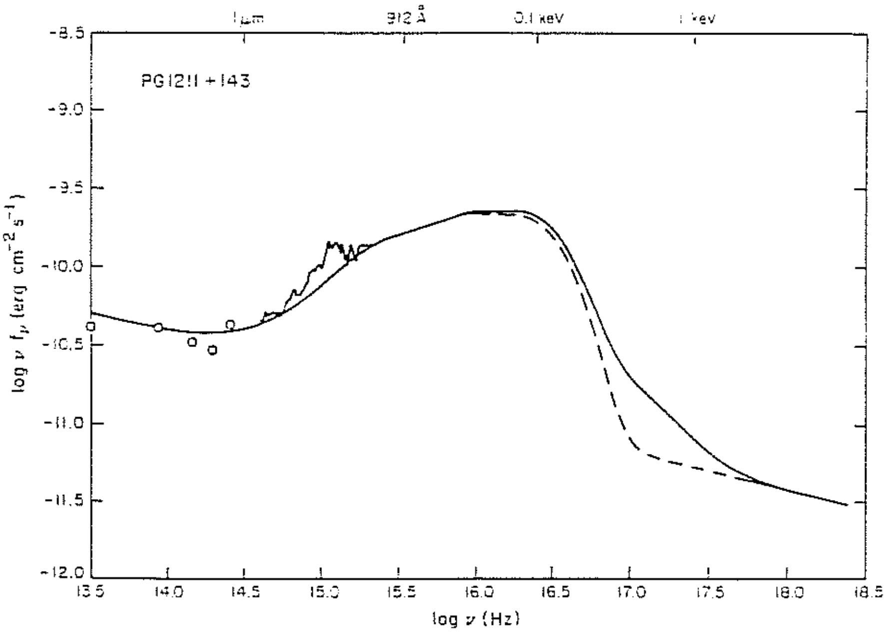

Figure 19: Fit to data for PG 1211+143 by an accretion disk with hot corona (solid line). The same disk model without a corona is shown as a dashed line (Czerny and Elvis, 1987).

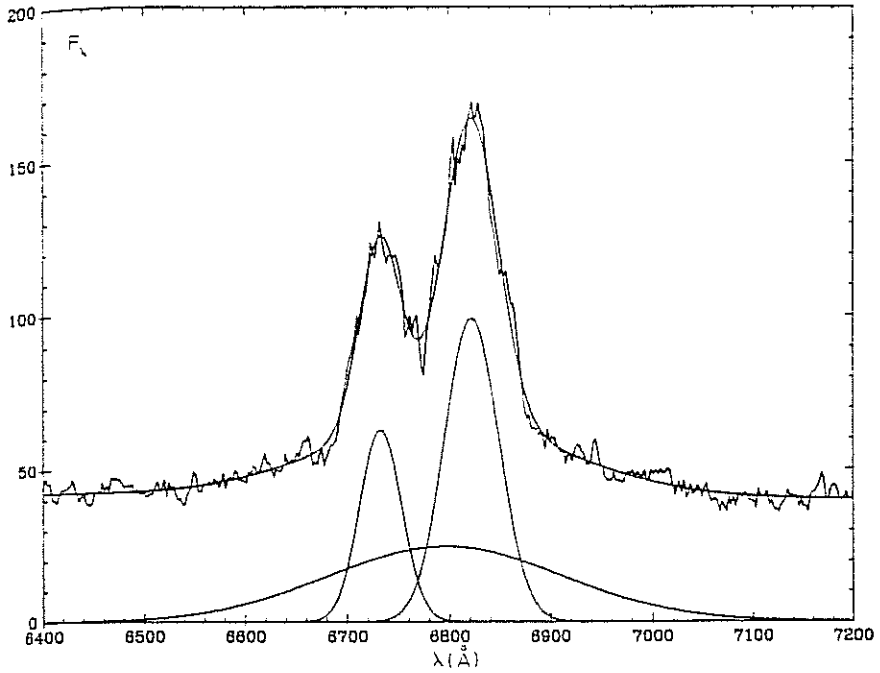

Figure 20: The H_α line profile (alloin, Boisson and Pelat, 1988)

characteristic two-peaked signature of large rotational motions. The two-peaked profiles (Figure 20) have been observed in Akn 120 (Alloin, Boisson and Pelat 1988). From variability studies of the AGN in this source and line profile analysis,it was found that its broad line emitting region contains, within a radius 2 light-months, a disk-structure.

NUMBER FIVE - NGC 4151

This Seyfert galaxy is the one which has been most extensively studied in the UV and x-ray ranges. One of many remarkable aspects of this object is that, based on the UV data alone, it seems to have changed regime or behaviour around 1981, being a "normal" bright active Seyfert nucleus before this date and changing to regime where it is weak to very weak with brighter episodes (Ulrich, 1986).

NUMBER SIX - Mkn 335

This is a galaxy with one of the largest observed UV bumps. IUE observations over several years have yielded little evidence for flux or spectral shape variations larger than 50% . It is therefore interesting to compare UV data with the variations in x-ray observed with EXOSAT. The medium energy component displays unusually strong variability on the timescale of 1 to 2 hours. There is also an intense soft x-ray component whose short term variability is not known. Both x-ray components increased by a factor 6 between November 1983 and December 1984 (Stanger and Pounds, 1986). The reason for the difference in behaviour between the UV and the x-ray ranges is not well understood. One possibility is that both the UV and soft x-ray components are radiated by an accretion disk with the variable soft x-ray component coming from the innermost edge where the luminosity and energy are expected to change more rapidly than near the outer cooler edges emitting the UV radiation. In this picture the similarity of the large decrease of the soft x-ray and medium energy components is not due to a common origin of the two components, but to the fact that 2-6 keV emission is coupled to the rate of accretion occurring near the innermost part of the disk.

NUMBER SEVEN - MGC-6-30-15

MGC-6-30-15 is a typical Seyfert galaxy ($L_{2-10} \approx 10^{43}$erg/s). The relatively short EXOSAT spectral survey observation in June 1984 revealed continuous variability on timescales down to 1 hour (Pounds et al., 1986). To examine this Seyfert galaxy in greater detail, a further EXOSAT observation was carried out in January 1986, extending over 2 days. The source was again bright and strongly variable. Figure 21 shows the ME (2-6 keV) light curve. Two particularly strong 'outbursts' are seen $\approx 9 \times 10^4$s apart, but the variability is essentially continuous. Strong correlation of the short term variability in the soft and hard x-ray components showed that these components have a close physical connection. In this regard the evidence for a lag of hard x-ray variability is especially intriguing. A straightforward explanation may be that the accretion process proceeds through the region of soft x-ray emission (inner, quasi-stable region of an accretion disk?), with the harder x-rays being produced in a chaotic region closer to the hole.

NUMBER EIGHT - 3C 120

The x-ray luminosity of 3C 120 is variable by a factor of 2.5 on

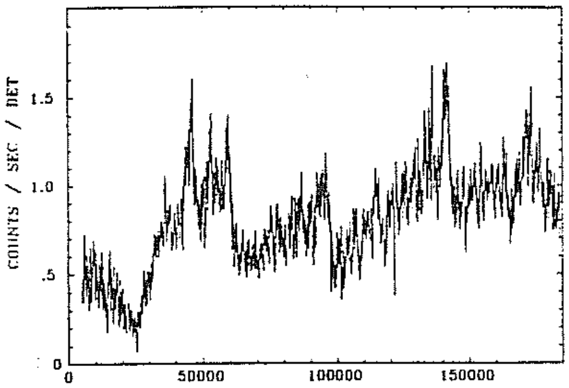

Figure 21: Background subtracted 2-6 keV light curve of MGC-6-30-15 during 29-31 January 1986, Pounds and Turner (1986)

timescales of days to months. The spectral slope of the 2-10 keV x-rays changes systematically in the sense that the higher intensity states are steeper (Halpern, 1985). The optical nucleus is variable almost 2 mag on timescales of years, with smaller changes occurring in ten days (Lyuty, 1979; Pollack et al 1979; Wlerick, Westerlund and Garnier 1979). A similar behaviour is seen in the infrared (Reike and Lebofsky 1979) and radio flux at several frequencies (Epstein et al. 1982). The most interesting observational results are, perhaps the VLBI maps of Walker et al. (1982, 1984) which show structural variations indicative of multiple ejection at apparent superluminal velocities. As the nearest and most rapidly varying superluminal source, 3C 120 is a prime target for monitoring at all wavelengths

NUMBER NINE - NGC 4051

The x-ray luminosity of NGC 4051 is extremely small, L(2-6 keV)$\approx 3 \times 10^{41}$ erg/s (Lawrence et al. 1985). The importance of the x-ray data lies in two qualitatively new features: continuous variability with a characteristic timescale of about 1 hour, and spectral changing during fluctuations.

NUMBER TEN - Mkn 841

The energy distribution for the best determined continuum distribution (PG 1501+106, Mkn 841) is shown in Figure 22. The luminosity

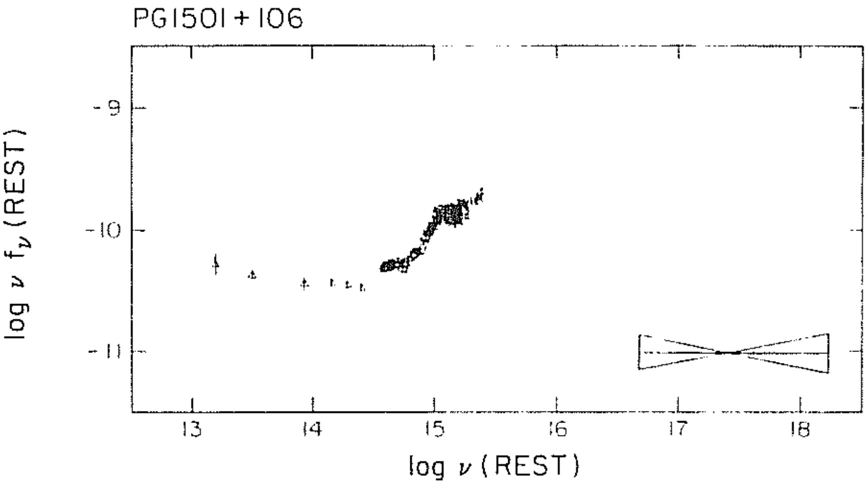

Figure 22: The energy distribution of Mkn 841

distribution across the entire five decade frequency range is remarkably uniform (Elvis, 1986). This continuum could be interpreted in many ways, the simplest, however, is to divide the distribution into just two components: a power low of slope ≈ 1 in the infrared extending, without a break into the soft x-ray region; and a "big bump" in the optical-ultraviolet superimposed on this power-law.

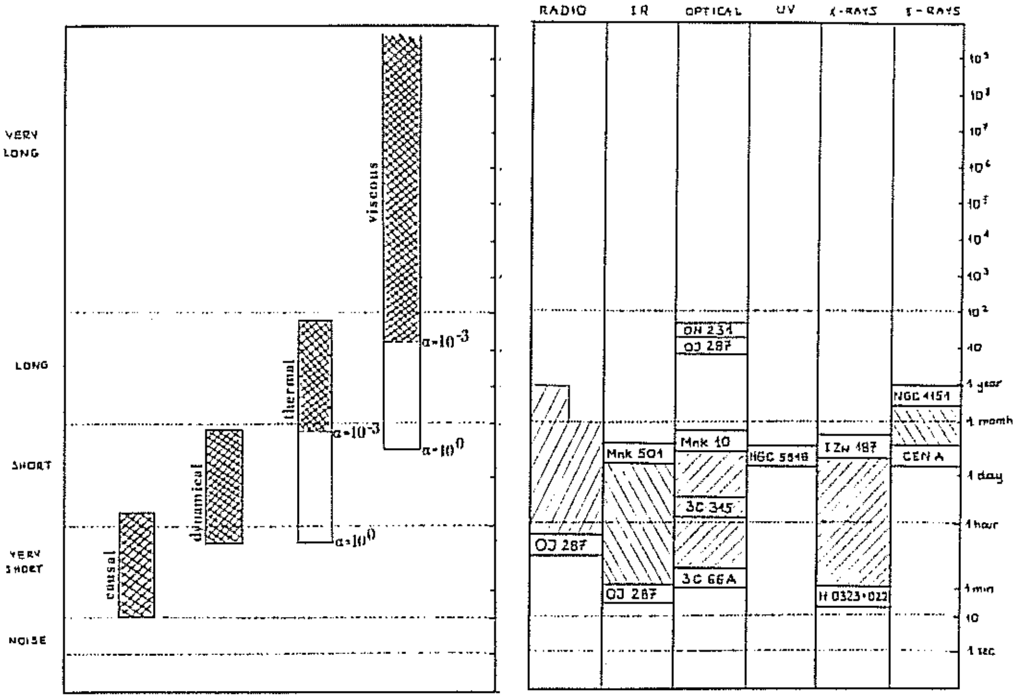

Figure 1: Theoretical timescales (a) and observed timescales (b). Names refer to the objects which are discussed in the text

7. Variability of AGN. Observational data

We start our review of the observational data with a comparison of two Figures: in Figure 1a we show the typical causal, dynamical, thermal and viscous timescales estimated from equation (1), i.e. from *theory*, and in Figure 1b we present the timescales actually *observed* in different objects and at different frequencies. Both theory and the observations cover several orders of magnitudes, but it can be seen that there is a general agreement between them. We shall now describe the observational data in some detail.

7.1 Typical light curves at different frequencies

The new optical catalog of quasi-stellar objects (Hewitt and Burbidge 1987) contains 427 objects. References to variability are made for only 12 percent of quasars in this catalog. In other samples, however, a substantially larger fraction of sources was found to vary: in the Rosemary Hill Observatory sample 50 percent of the objects are variable (Pica et al. 1980), and in the Asiago sample 43 percent of observed objects show variability (Barbieri et al. 1983). When all of the published data is included, then 56 percent of the objects from the Asiago sample are variable. This is contrary to the commonly held opinion, that variability of AGN is rare.

The Rosemary Hill classification (Mc Gimsey et al. 1975) describes the complex morphology of the light curves of AGN in terms of four basic types by using two main characteristics of the time behavior: short-term flickering occurring with time scales of days or weeks and having amplitudes $0.5-1^m$, and long-term variations (*secular trends*) occurring with timescales of months or years. The *first type* contains light curves dominated by rapid short-term flickering. Long-term trends are inconspicuous and, if present, are very gradual. The *second type* is characterized by prominent long-term variations in the mean level. Flickering appears as minor excursions about this changing average. In the *third type*, the light curves are dominated by a mixture of the two components which here have comparable amplitudes. The *fourth type* contains light curves having long periods of quiescence which are interrupted by relatively brief periods of activity (bursts). These four types are generic for AGN variability and are characteristic not only of optical light curves but also (with different timescales and amplitudes) of other variability phenomena. For the real data, they can be recognised in Figure 2, which shows the variability of 3C 345 (Kidger and Beckman 1986), and in other Figures presented in this section. One can also add to this classification a *fifth type* having no variability at all.

In addition to explaining the existence of the five main types of variability and the statistical distribution of AGN among these types, a successful theoretical model must also explain the characteristic *detailed* features which are observed in many of the light curves. Some of them, especially the optical light curves for BL Lac objects, show not only *outbursts* but occasionally also *deep minima*. Often, after a primary maximum of brightness, there is a decline followed by a *secondary maximum*. The secondary maximum can be delayed after the primary one a few days (e.g., 17 days for AO 0235+164, Dent and Balonek 1980, a month for ON325, Pica et

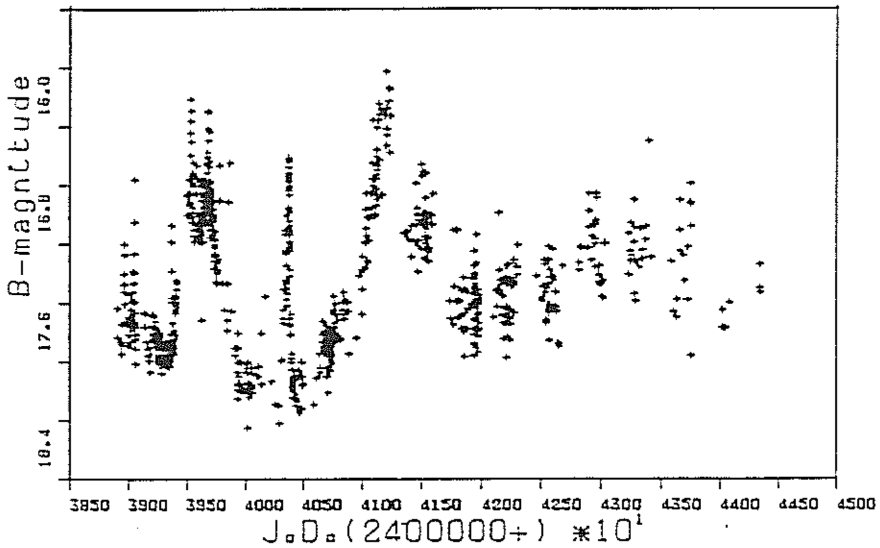

Figure 2: The optical variability of 3C 345

al. 1980), some months (e.g., 3 months for OJ 287, Sillanpää et al. 1985) or even several years (Barbieri et al. 1988, University of Padova preprint). Such a behavior suggests that the mechanism of the outburst may be a sort of damped oscillation. Outbursts appear also at other frequencies, and events occuring at different wavelengths are often correlated (e.g. Bregman et al. 1986 for 3C 345).

To illustrate mentioned characteristic of optical light curve of BL Lac objects we will use detail long term observations of three objects from this class performed in Asiago Observatory (Barbieri et al 1988). For three sources: ON 231, ON 325 and RS4 we have rich observational data, sufficient for constructing the historical light curves. The light curve of ON 231 is shown in the Figure 3. It consists of a set of outbursts. Neglecting the oldest (1898-1916) quite uncertain observations (Wolf, 1916), two major outbursts were observed., one in 1940, and second in 1968 (Pollock et al., 1974), while another possible active period in 1952 was not completely covered by observations. It is very interesting to note the similar structure of these two outbursts (one magnitude pulse of halfwidth about 3 years). The complicated behaviour of the intensity of the source after 1960 is presented

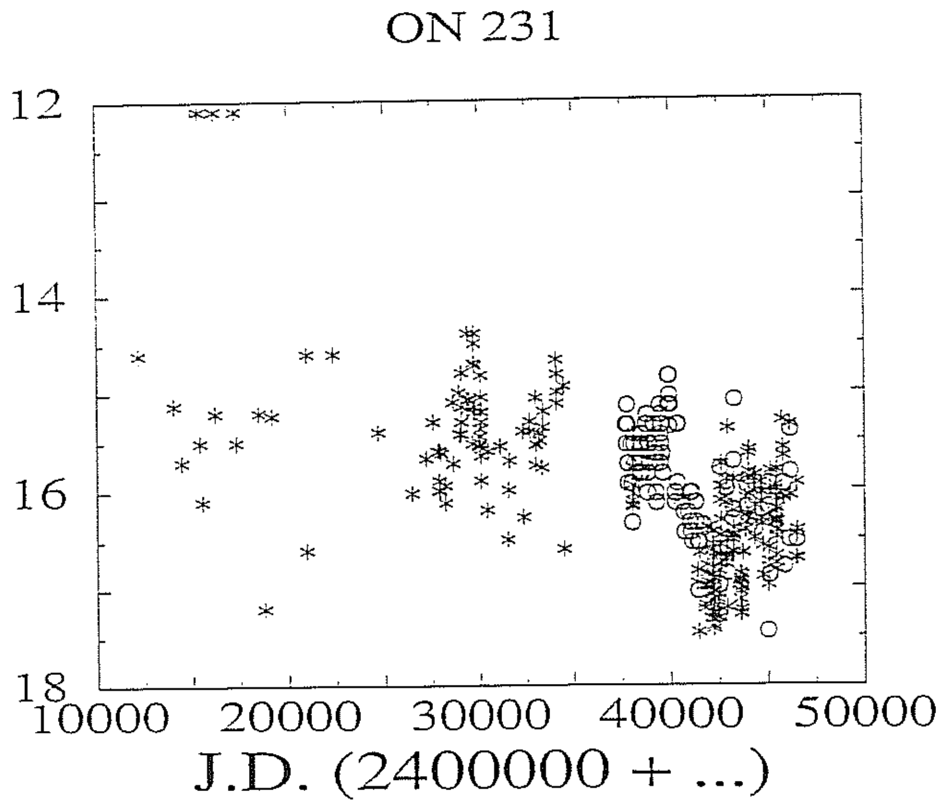

Figure 3: The historical light curve of ON 231.

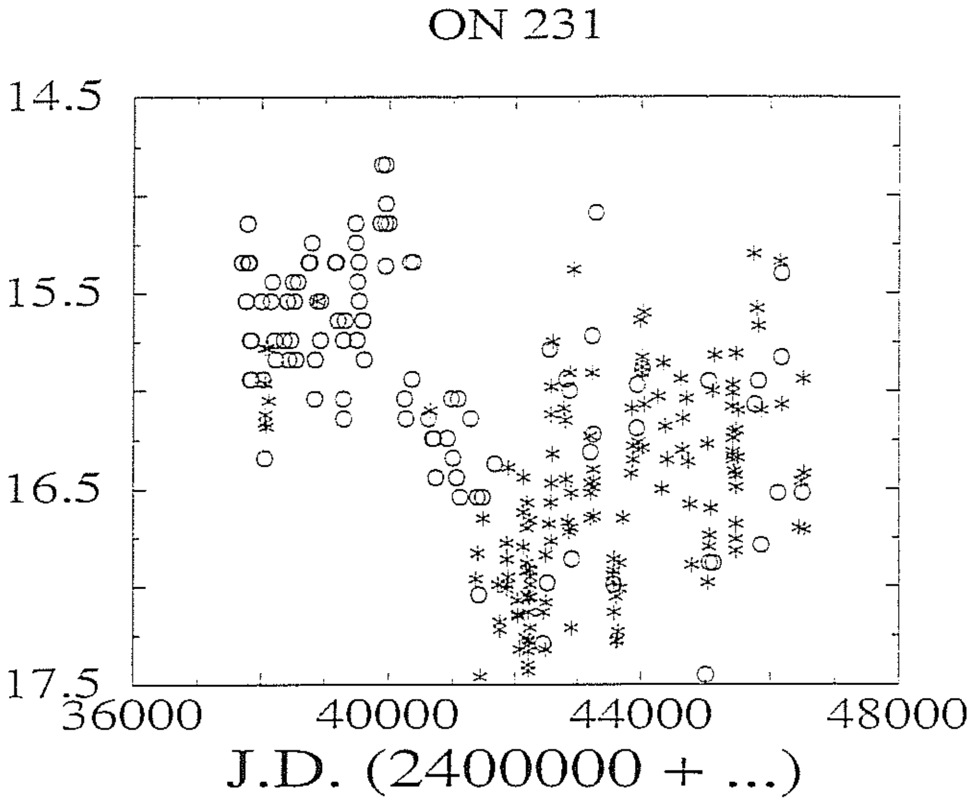

Figure 4: The optical light curve of ON 231 after 1960.

on the larger scale in Figure 4. After peaking in 1968, the light decreases forming a deep minimum. Other two smaller pulses are observed at the distance of 9 years and 16 years from the 1968 major event. The Fourier analysis does not reveal any clear periodicity; it is possible to interpret the light curve as a slow secular decrease of the intensity and sporadic outbursts overlapping on it (see also Webb et al., 1988).

The historical light curve for ON 325 is reported in Figure 5. The variation of the optical luminosity of this object is irregular. The amplitude of pulses is around one magnitude. A deep minimum appears around JD=2442000.

Figure 6 presents the light curve of RS4. Data are mainly Asiago observations (open circles). In 1941 a one magnitude outburst took place (Schwartz et al., 1979). No other clear feature is present in the light curve given by this author. From our measurements is evident the existence of the peak around 1975. The source appears to be less variable than the two

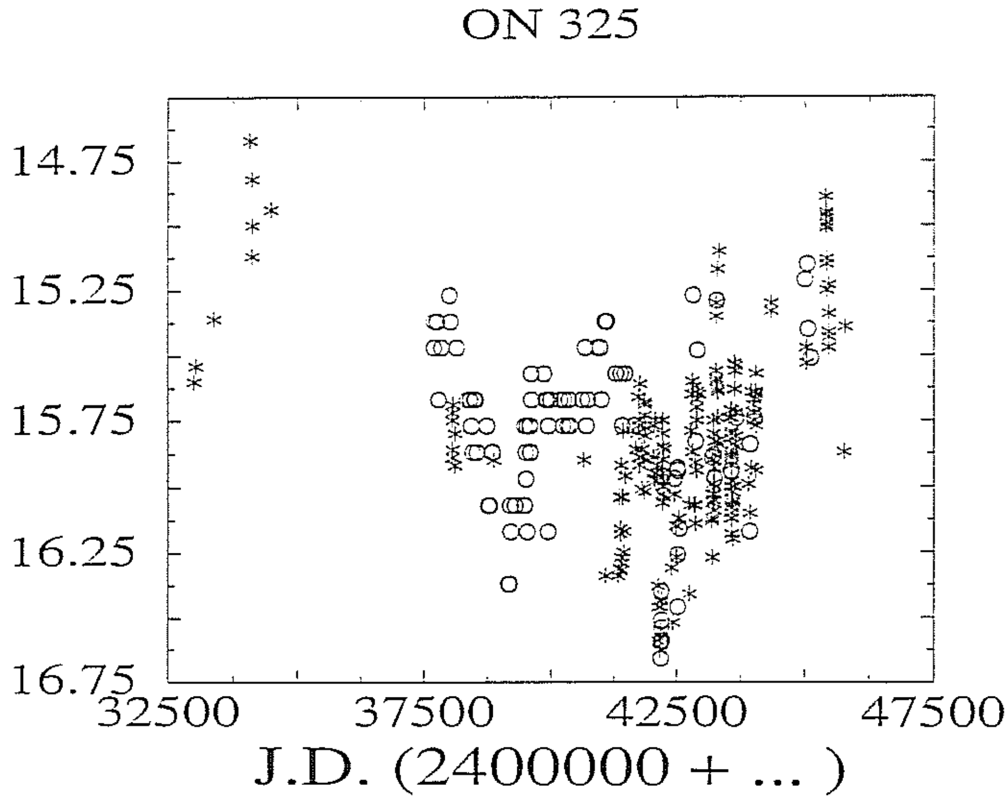

Figure 5: The historical light curve for ON 325.

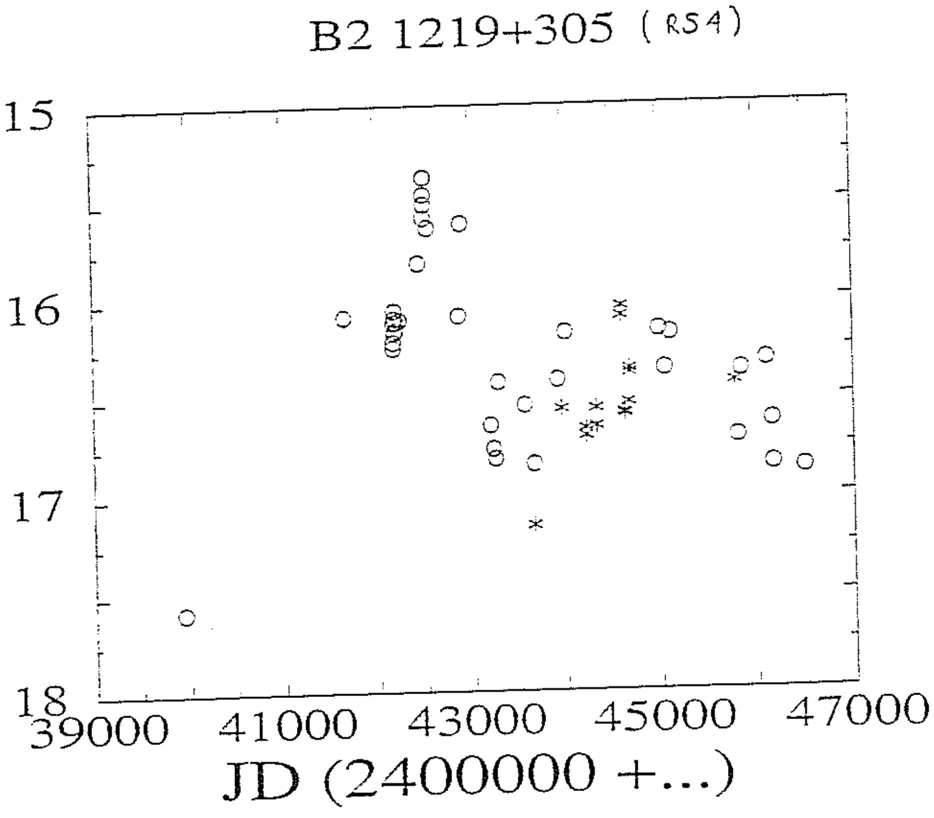

Figure 6: The light curve of RS4.

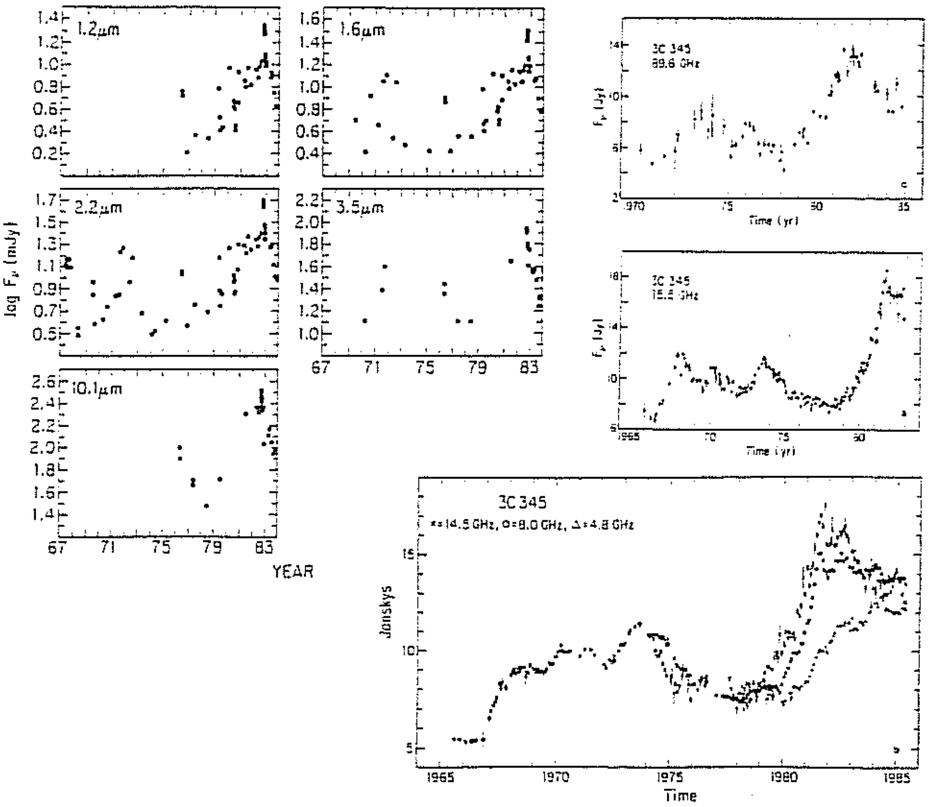

Figure 7: The infrared and radio observations of 3C 345

others examples of the BL Lac class in our sample (ON 231 and ON 325). The history oi the optical variability can be summarized as two outbursts at a distance of 34 years.

In the infrared, both flickering and secular trends have been observed (with the shortest timescale for flickering being about 40 days in the case of 3C 345). In general there is a close correspondence between the brightness changes in all of the infrared bands. Outbursts are more pronounced at shorter wavelengths. The October 1982 infrared outburst of 3C 345 is shown in Figure 7. Salonen et al. (1987) have reviewed long term monitoring (over a few years) of AGN at radio frequencies. The same variability features are usually observed at several frequencies, but typically the outbursts at lower frequencies begin later and have smaller amplitudes. Flickering is not observed. Although the three largest infrared-optical outbursts of 3C 345 preceded the three largest radio outbursts by roughly 1-2

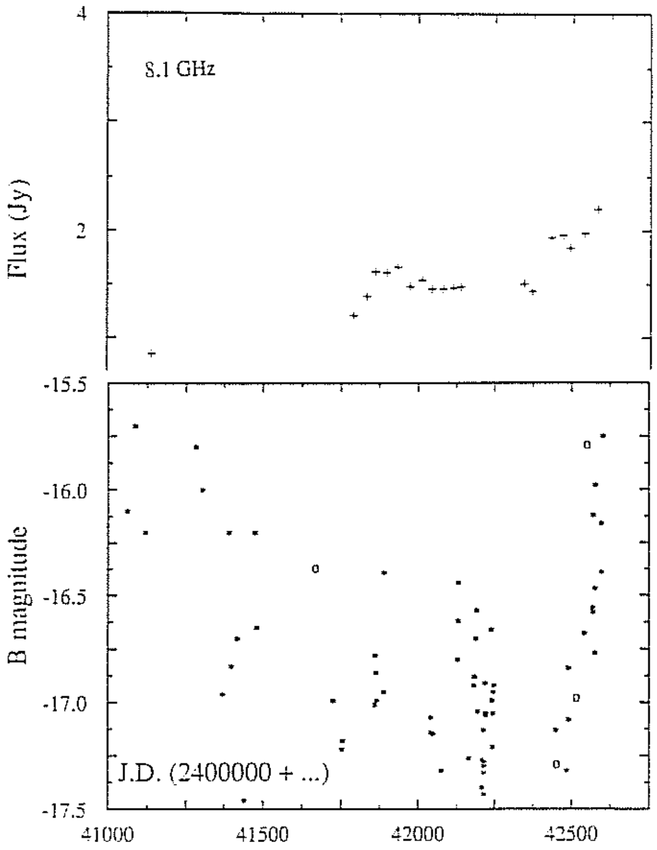

Figure 8: The correlation between radio and optical observations of ON 231.

years, the correlation between these events is doubtful. Another example of the possibility of optical-radio correlation in intensity we found in the BL Lac type object, ON 231 (Barbieri et al., 1988). We compare our optical light curve with the radio observations by Altschuler and Wardle (1976). We found that the begining of the active period in radio (at 8.1 GHz and 2.7 GHz) occurs around JD =2442500 so at the same time as the optical outburst (Figure 8). In general, there is no obvious correlation between variability in the optical-infrared and radio frequencies.

Before going to the next range of frequencies few words are needed about polarization which seems to be the bank of informations for variability and their interpretations. The linear polarization of the radio sources has been observed to vary in the rapid and complicated way (Altschuler and Wardle, 1976). We found that the changes in radio polarization of ON 231 have clear similarities to changes in intensity in the optical range. The

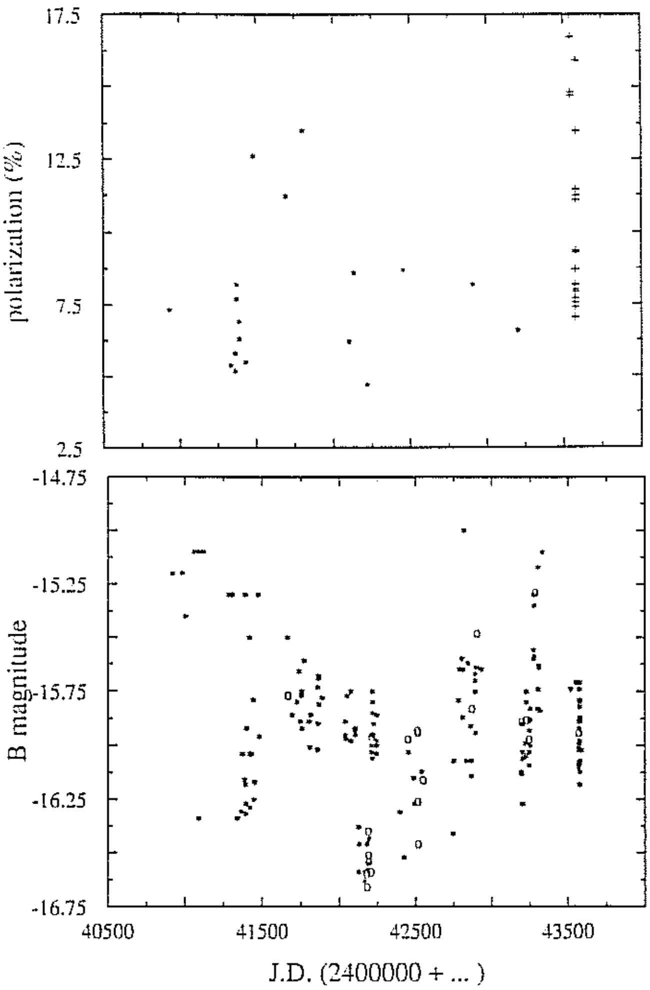

Figure 9: The correlation between optical polarization and intensity of ON 325

changes of optical polarization in ON 325 (Angel et al., 1978) are extremely well correlated with the optical light curve (Figure 9). From the comparison with the optical light curve we can then better derive the minima of the degree of polarization. As noticed by Kikuchi et al.(1988), two interpretations of rapid flux and polarization in blazars, i.e. relativistic beaming and simple two component model, predict that the minimum degree of polarization is always associated with the maximum rate of variation of the polarization angles. They have found consistency with their observations of OJ 287. In our case the position angle does not show large amplitude changes, remaining in the range 135-175 degrees. However two fast changes appear correlated with the polarization minima. Optical polarimetry of RS4 is extremely poor. We found only four points in the V band and in the B band (Wills et al., 1980, Sanduleak and Pesch, 1984). The four points in the V band show tendency to increase starting from 4.6% in 1980 and reaching 8.4% in 1982. The position angle in this period is changing in the range of

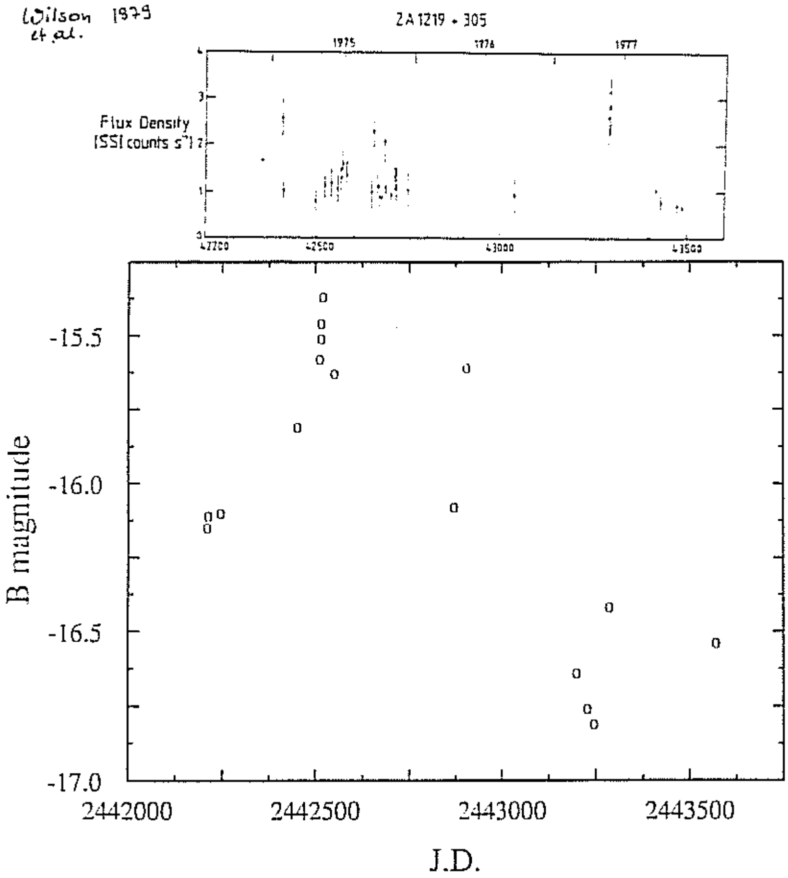

Figure 10: The correlation between optical and x-rays observations of RS4.

48-58 degrees. No clear correlation with light curve can be found.

Long-term monitoring of AGN at X-ray wavelengths has been carried out for omy a few objects. One of the best cases (B2 1218+305, reported by Wilson et al., 1979) consists of a light curve which spans four years and show some possible outbursts. In most of the other studies, the X-ray light curves are based on only a few points (e.g., 3 points for 3C 345, Bregman et al. 1986). Comparing optical data for B2 1218+305 obtained in Asiago with the X-ray measurements by Wilson et al. (1979) one can find a correlation between active periods for this source at these two wavebands. The X-ray outburst took place at the beginning of 1974 while the optical one was a hundred days later (Figure 10). Bregman et al. (1986) discussed the results of comparing X-ray, optical-infrared and radio variability data for 3C 345. The beginning of the radio outburst coincides with the X-ray measurements and the increase in the X-ray flux is about the same as the increase in the 15 GHz radio flux. They did not find any apparent correlation between the X-ray and optical-infrared fluxes. Unless variations occur much more rapidly at X-ray frequencies than at optical and infrared frequencies, the X-ray emission is probably associated with the radio emitting region rather than with those regions emitting in the infrared or optical.

The short-term X-ray variability usually occurs on all of the relevant timescales. Pounds et al. (1987) have illustrated this by discussing three generic types of X-ray variability, similar to the Rosemary Hill types (but omitting the third). The example of the first Rosemary Hill type is the rapid variability of NGC 4051 (Lawrence et al. 1985). The source varies with a timescale ≤ 1 h and with large amplitude. The variability is essentially continuous. Some "outbursts" can be seen. The same type of behavior is shown by MCG-6-30-15. McHardy and Czerny (1986) concluded from their analysis of the light curve of the Seyfert galaxy NGC 5506 (obtained by continuous 3-day observations with EXOSAT in medium X-ray energies) that the observed variations which have amplitudes of up to 30 percent and timescales of hours, can be explained as a random distribution of events with random amplitudes. The example of the second Rosemary Hill type is the variability of NGC 4151 which shows secular trends, rather than rapid fluctuations. The fourth Rosemary Hill type is represented by the variability of III Zw 2, where a large flare was found in the X-ray light curve: the flux increased by a factor of 3 in about 1500 sec and then decreased again to nearly the initial level in a further 4000 sec. Most recently Turner and Pounds (1988) reported distinctive short term variability in the soft X-ray excess of the Seyfert galaxy Mkn 335. This is the first observation of this kind and it strengthens the proposed identification of the soft X-ray excess as being of thermal origin and coming from an accretion disk.

7.2 Line variations

The intensity of the broad emission lines (BEL) observed in many active galactic nuclei is proportional to the flux of ionizing radiation (Kwan and Krolik 1979, 1981) which is believed to come directly from the accretion disk. Therefore, variation of the intensity of BEL may be an indicator of non-stationary accretion processes occurring directly inside the disk. However, it is not possible at present to make a direct quantitative link, as the kinematics and internal physics of the so called "broad emission line clouds", where the emission lines originate, is still a matter of dispute among experts. Even the very existence of such clouds is sometimes questioned and it has been suggested that the emission lines might instead originate at the surface of the accretion disk itself (Shields 1977), at some high velocity stars passing nearby (Paczyński, unpublished suggestion), or due to action of "duelling" winds (Mardaljevic et al. 1988). The most convincing and well established theoretical discussion of the broad emission line emitting region is that given in a series of articles by Collin-Souffrin (1986) and her collaborators (e.g. Joly et al. 1985). Observations of variability of BEL have recently been reviewed by Peterson (1988).

Alloin et al. (1986) reported variability of BEL in the Seyfert galaxy NGC 1566. Their data covers 15 years and suggests the occurrence of four almost periodic active events (bursts), each lasting for about 1300 days, in which the intensity of the H_α and H_β lines first increased sharply (in about 20 days) and then decreased again (in a much longer time of about 900 days). The total energy involved in each burst was 10^{51} ergs. The peaks in the intensity of the lines coincided with increased intensity of near UV continuum. Another well-known example of a correlation between variability of lines and continua was given by Peterson and Ferland (1986), who observed that the optically variable Seyfert galaxy NGC 5548 experienced an increase in optical luminosity accompanied by the appearance of a strong and abnormally broad He II [4686 A] emission line. Krolik (1988) has discussed further examples of such correlations. However, in our opinion the presently available data do not provide a clear, quantitative, case for there being a universal correlation between variability of emission lines and of the continuum.

Abramowicz and Lasota (1985, unpublished) studied the case of NGC 1566 using the (then unpublished) data of Alloin et al. (1986). Taking the mass to be $5 \times 10^7 M_\odot$ (in accordance with an earlier estimate by Alloin et al. 1985) and the efficiency to be $\eta = 0.06$ they concluded that the accretion rate averaged over the whole cycle was about $0.3\dot{M}_E$ and that the amount of matter accreted during one burst was about $10^{-2} M_\odot$. This suggests that the variability was not caused by a change in the supply rate due to the capture of a single star during each outburst (random capture of four unusually low mass stars in an almost periodic fashion has a small probability). They argued that the most natural explanation of the periodic outbursts of NGC 1566 is the existence of a limit cycle produced by accretion disk instabilities. Figure 11 shows the 1982 outburst of NGC 1566.

7.3 Search for periodicities

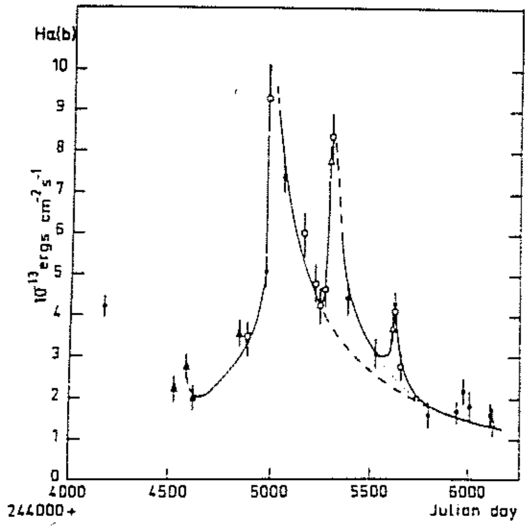

Figure 11: The 1982 outburst of NGC 1566

Some QSOs are believed to have periodic light variations. The first indication of the possible existence of nearly periodical brightness variations was found, for quasar 3C 273, by Smith (1965) but was immediately questioned by Ozernoy and Chertorpud (1966). Nearly periodic variation in the optical luminosity of the quasar 3C 345 was suggested by Kinman et al. (1968) and later confirmed by Smith and Wolstencroft (1970). The existence of periodicity in the brightness variations of 3C 446 and 3C 454.3 was suggested by Lü and Hunter (1969) and later by Kinman (1970). Jurkevich et al. (1971) reported a periodic component with $P = 350^d$ for 3C 120. Visvanathan and Elliot (1973) discovered, using Fourier analysis, that the brightness of OJ 287 varies with a surprisingly short period P =39.4 minutes. This was confirmed by Frohlich (1973) but questioned by Kiplinger (1974). Other examples are NGC 4151 (Pacholczyk 1972), 3C 371 (Babadzanjanz and Belokon 1975), NGC 1275 (Lutyi and Pronik 1975), BL Lac in optical (Ozernoy and Usov 1977), BL Lac in radio (Gorshkov and Popov 1972) and OJ 278 in radio (Hagen-Thorn et al. 1977). This long list of successes in finding periodicities may be too optimistic. The recent analysis of all existing data for 3C 345 by Kidger and Beckman (1986) shows that there is no periodicity which is free from doubt. In particular they exclude the long periods of 1000-2000 days obtained by Barbieri et al. (1985). A recent paper by the Rosemary Hill group (Webb et al. 1988) used only the data gathered by the same instruments and reduced by the same procedures. It discussed three objects in detail: 3C 120, 3C 345 and 3C 446. The sinusoidal component found for 3C 120 with a period of 12.45 yr and the components for 3C 345 with periods of 11.4 and 5.6 years did not agree with any periodic components suggested by other authors. The conclusion of the paper was that identification of periodic components in a finite data set does not prove the existence of "real" periods in the source. Barbieri et al. (University of Padova preprint 1988) carried out a similar study with the Asiago data and reached a similar conclusion. They then discussed the Rosemary Hill data for ON231 (Webb et al. 1988) and performed a Fourier analysis using the program of Deeming (1975). They found the same periods as the Rosemary Hill group. However, when they repeated the procedure with the Asiago data for the same source (which is as extensive as the the Rosemary Hill data) none of the periods which they found agreed with those found by Webb et al. As a last step they took all of the data reported in the literature. All periods disappeared except a 27 year period - the interval between two almost identical outbursts found for this source a long time ago (Pollock et al. 1974).

The nature of the optical observations is not very convenient for making periodicity searches: there are unequal intervals of time between observations and annual gaps in the data, together with the normal observational uncertainties and the relatively short baseline of the data set. For a recent discussion of this point, see Krolik (1988).

The same difficulties may explain the conflict between the results obtained by the EXOSAT and *Einstein Observatory* X-ray satelites. Zamorani et. al (1984), using the *Einstein Observatory* data, concluded that for roughly half of their sample of bright quasars they should have been able to detect variations of the order of 30 per cent in amplitude and with timescales shorter than 10^4 seconds but, in fact, did not see any such variations. A similar conclusion, that short-term variability in optically selected Seyfert galaxies is rare, has been reached by Urry et al. (1987), who also used the *Einstein Observatory* data. On longer timescales (months, years) Urry et al. found that variability is more common. However, recent EXOSAT results have called these conclusions into question. These results do not indicate long-term variability and suggest that short term-variability is common at X-ray frequencies (Pounds 1985, Warwick 1986).

The best example of the short-term X-ray variability is provided by NGC 5506 which was observed continuously for 3 days by EXOSAT (Cz-

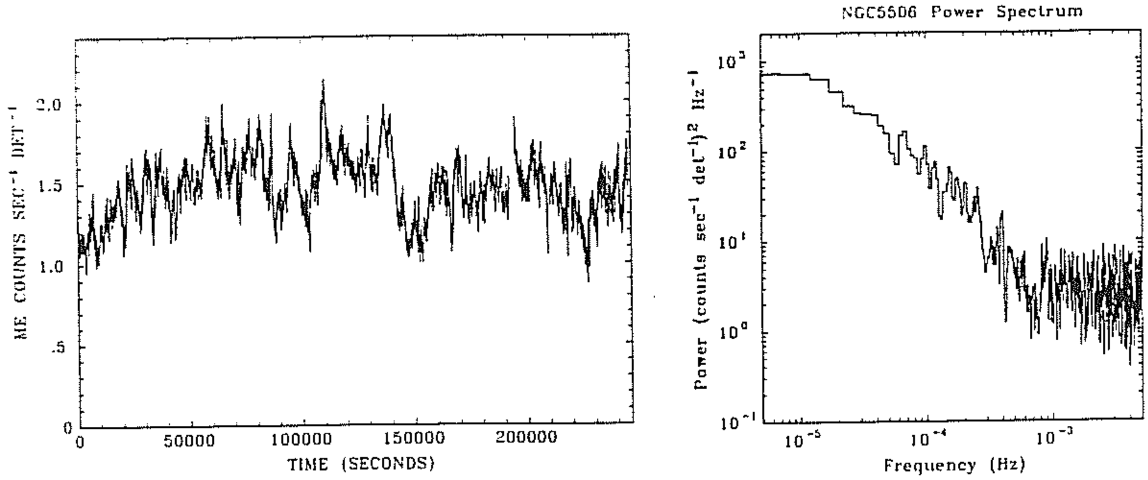

Figure 12: The X-ray light curve for NGC 5506 and its power spectrum

erny and McHardy 1987). The light curve (Figure 12) shows variability on all timescales. The power spectrum has a slope of -1 in the frequency range $10^{-4.8} - 10^{-3.5}$ Hz, similar to that found for the galactic X-ray source Cyg X-1, which is believed to be a $10 M_{\odot}$ accreting black hole (McClintock 1986, Ilovaisky 1987). Czerny and McHardy did not find any obvious strong feature in the power spectrum and concluded that there are no preferred timescales - variability occurs in a perfectly scale-invariant manner. They reached the same conclusion using fractal analysis, showing that the X-ray variability of NGC 5506 is well described by a fractal dimension 0.6 over at least 2.5 decades of frequency so that the variability is self-similar. The comparison with the fractal dimension of Brownian motion (0.5) suggested to them that random processes might be responsible for the irregular shape of the X-ray light curves. They also investigated the variation of the medium energy spectrum as a function of intensity and found no evidence for any changes.

The different results obtained using *Einstein Observatory* and EXOSAT may reflect inherent differences between the sources observed , as the selection criteria were different: The EXOSAT survey used well-studied, X-ray bright, historically variable X-ray sources, while the *Einstein Observatory* survey was based on complete, optically selected samples. However, the differences may be of a purely technical nature connected with the fact that EXOSAT was capable of much longer observing times (for each observation) than the *Einstein Observatory* but had a shorter total life time. This stresses the importance of good selection criteria and frequent sampling in future space missions which plan to study variability of AGN (see e.g. Broadfoot, Duran and Stalio 1988 in the case of the *Santa Maria* satelite).

7.4 The shortest observed timescales

Short term variations in luminosity provide the best upper limits for the size of AGN active regions. The causality argument implies that a timescale of variation cannot be shorter than $t_c \approx 10^{-2} m$ days. Assuming also that the luminosity L cannot be greater than the Eddington value, Elliot and Shapiro (1974) derived from these two constraints the simple condition $log \Delta t_{min} > log L - 43.1$ where the observed minimum variation timescale Δt_{min} is measured in seconds and the observed luminosity L is in ergs per second. According to the Elliot-Shapiro condition, all observational points should be *above* the corresponding diagonal line in Figure 13a (adopted from Bassani et al. 1983). However, even for sources which are not affected by relativistic beaming (discussed in Section 1.2), one should take into account the super-Eddington luminosities of radiation pressure supported tori (Abramowicz and Nobili 1982). The corresponding line in the Figure assumes that the limiting luminosity is $100 L_E$, in agreement with Sikora (1981) who calculated (using a precise numerical code) the radiation field of several thick accretion disk models. We have added a radial scale to this Figure which shows the *minimum* possible radii consistent with the observational data and with the Elliot-Shapiro condition. This scale is diagonal in a direction orthogonal to the line representing the E-S condition and is marked by numbers giving the radii in terms of r_G. Barr (1986) constructed a similar diagram for the X-ray data which is shown in Figure 13b. The scatter of the observational points is smaller for the X-ray data, which suggests that the X-ray emitting regions are responsible for the shortest variability timescales. The two lines marked by E-S and A-N (which have the same meaning as in the previous Figure) have been added by us.

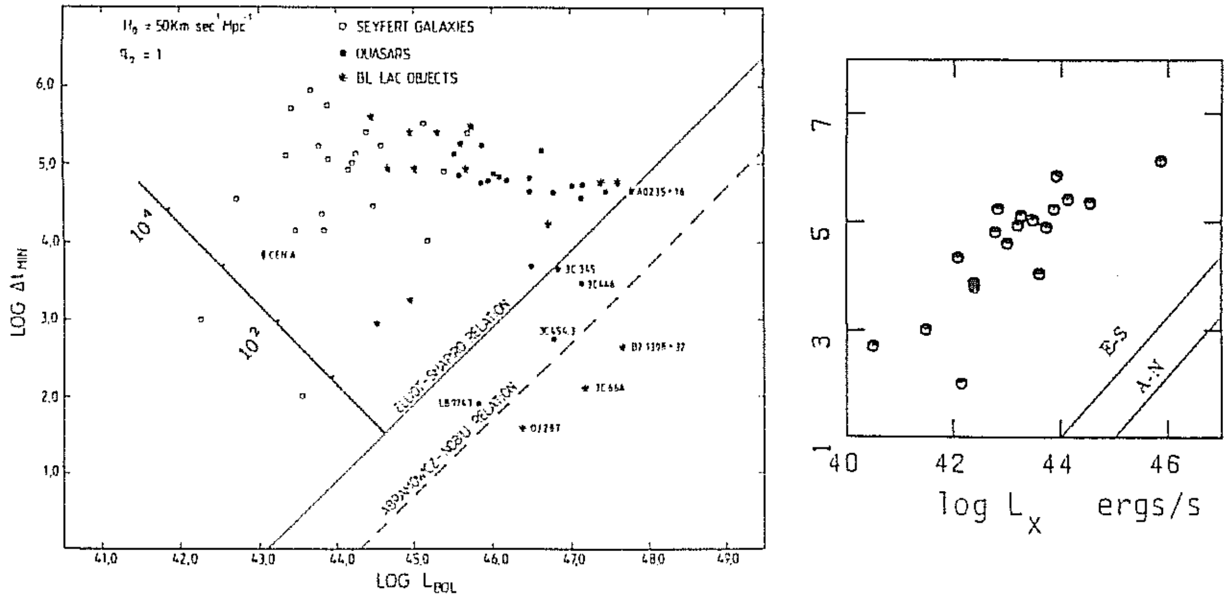

Figure 13: The shortest timescale as a function of bolometric luminosity and X-ray luminosity respectively

8. Variability of AGN. Accretion disk instabilities

We now turn to the theoretical side of the problem. Most of the computed stationary accretion disk models assume axial symmetry. To check whether these models can describe real physical flows one must discuss their stability with respect to small non-stationary and non-axially symmetric perturbations. Discussion of the stability and pulsation properties also gives information on non-stationary behavior which is crucial in understanding the variability data.

In a linear perturbation analysis, one expresses the perturbations of the five independent physical quantities Q_i =(density, pressure, and the three components of velocity) in a form which reflects the time and axial symmetries of the unperturbed flow: $\delta Q_i = \tilde{Q}_i(r, z)\exp[i(\omega t + m\varphi)]$. Here $\tilde{Q}_i(r, z)$ is a real function which determines the amplitude of the perturbation, ω is in general a complex number and denotes the frequency, while m is an integer which denotes the azimuthal wavenumber. A perturbation is stable if and only if its frequency has non-negative imaginary part: $Im(\omega) > 0$. When $m = 0$ the perturbation is axially symmetric. The behavior of perturbations is given by the linearized version of the non-stationary, non-axially symmetric Navier-Stokes equations, which describe the hydrodynamics of dissipative flows in terms of mass, momentum and energy conservation (see e.g. Tassoul 1974). Together with suitable boundary conditions, the linearized equations provide, for fixed wavenumber m, an eigenvalue problem for the *modes of pulsation*. The n-th mode is described by eigenfrequency ω_n and eigenfunction $\tilde{Q}_{in}(r, z)$. Knowledge of all of the modes gives a *global*, complete picture of the pulsation properties and stability in the linear regime (i.e. for infinitesimally small amplitudes). However, it is very difficult, in general, to compute these global modes of pulsation for accretion flows. The main difficulty is usually connected with the boundary conditions. To get some approximate information on stability one often uses a *local stability analysis* where the influence of the boundary conditions is neglected and the perturbations are described by *local* plane waves, which means that the amplitude $\tilde{Q}_i(r, z) = \tilde{Q}_i \exp[i(k_r + k_z)]$. Now the $\tilde{Q}_i$ are five a priori unknown *constants* and $(k_r, k_z) = \vec{k}$ is the wave vector whose length will be denoted by k. Linearization of the Navier-Stokes equations produces an equation of the form $A_{ij}\tilde{Q}_j = 0$, $(i = 1, ...5)$ which has a non trivial solution for $\tilde{Q}_j$ if and only if the determinant of the matrix A_{ij} vanishes. This produces a fifth order dispersion relation for ω. Let H_r and H_z denote the scaleheights in the r and z directions. For thin accretion disks one has $H_z \ll H_r$, while for the thick accretion disks $H_r \approx H_z \approx H$. In the case of peturbed thin disks, one considers perturbations with wavelength $\lambda = 1/k$ much shorter than the radial scaleheight, but longer than the vertical scaleheight $H_z < \lambda \ll H_r$. For thick disks, on the other hand, one demands that $\lambda \ll H$. Different physical situations may suggest different ordering of these or other terms.

Abramowicz, Livio, Piran and Wiita (1986) proposed a method for studying the linear, local stability of general hydrodynamical flows, which guarantees that all physical possibilities (corresponding to different relative magnitudes of terms in the dispersion relation) are accounted for. They then used this to give a complete picture of stability of non-dissipative flows. In a follow-up paper by Abramowicz, Livio, Soker and Szuszkiewicz (to be published), the same was done for accretion flows with viscosity and thermal heat diffusion. We shall now describe some of the results found in these two papers.

The basic assumption of the local analysis provides us with a natural small parameter $\epsilon = \lambda/H_r \ll 1$. It is then helpful to introduce the "magnitude parameters" $(\bar{k}, \tilde{m}, \tilde{n}, \bar{l}, \tilde{q})$ which denote the powers of ϵ to which terms in the dispersion relation are proportional. In particular, the terms $H_z/H_r \approx k_z/k_r \approx v_z/v_r$ have magnitude $\bar{k}$, the term ω/Ω has magnitude $\tilde{m}$, the term v_r/v_φ has magnitude $\tilde{n}$, the viscosity parameter α has magnitude $\bar{l}$, and the terms connected with heat diffusion (and therefore containing the coefficient of radiative diffusivity, χ_{rad}) have magnitude $\tilde{q}$. The parameters $\tilde{m}, \tilde{n}$, and $\tilde{q}$ vary from $-\infty$ to $+\infty$ and the parameters $\bar{k}, \bar{l}$ vary from 0 to $+\infty$ (assuming $\alpha < 1$). The problem is then to find all of the regions of the five dimensional parameter space $(\bar{k}, \tilde{m}, \tilde{n}, \bar{l}, \tilde{q})$, corresponding to different dispersion relations in which only the lowest order terms in ϵ have been kept, write down these relations and then check whether they admit unstable modes.

8.1 Local stability analysis for thick accretion disks ($\bar{k} = 0$) with respect

to axisymmetric perturbations ($m = 0$)

We start with the non-dissipative case ($\bar{l} = \bar{q} = \infty$). Here, the parameter space is two dimensional ($\bar{m}, \bar{n}$) but in addition there is a "diagonal fold symmetry" with respect to the line $\bar{n} = \bar{m} + 1$ and this makes the problem effectively one dimensional. The diagonal symmetry line corresponds to perturbations propagating with velocity equal to the unperturbed accretion velocity. Three types of modes are present:

neutral stable mode, $\omega^* = 0$

stable acoustic mode, $\omega^* = \pm v_S k$

Hoiland mode, $\omega^* = \pm \Omega_H$

where $\omega^* = \omega + \vec{k} \cdot \vec{v}$ and the characteristic frequency Ω_H is defined by

$$\Omega_H^2(k_r, k_z) = -\rho^{-1}(\frac{\partial S}{\partial \rho})_P^{-1} k^{-2}(\vec{k} \times \vec{g}) \cdot (\vec{k} \times \nabla S) + k_z r^{-3} k^{-2}(\vec{k} \times \nabla l^2) \cdot \vec{e} \quad (1)$$

with $\vec{g}$ being the effective gravity, $\vec{e}$ the unit vector in the azimuthal direction, S the specific entropy and $l = \Omega r^2$ the specific angular momentum. The Hoiland mode is stable when the quadratic form $\Omega_H^2(k_r, k_z)$ is positive definte, which is equivalent to the well known *Hoiland stability criterion.* This requires that on the surfaces of constant entropy the specific angular momentum should increase with increasing distance from the axis of rotation:

$$r^{-3}(\frac{\partial l^2}{\partial r}) - (\frac{\partial T}{\partial p})_S(\nabla p \cdot \nabla S) > 0$$

$$-(\frac{\partial p}{\partial z})[(\frac{\partial l^2}{\partial r})(\frac{\partial S}{\partial z}) - (\frac{\partial l^2}{\partial z})(\frac{\partial S}{\partial r})] > 0$$

When $l = 0$ this reduces to the Schwarzschild stability criterion, and when $S = const$ it reduces to the Solberg criterion, which generalizes the Rayleigh criterion to the case of compressible fluids. All of these criteria are independent of the wave vector $\vec{k}$. This is important, because it implies that stability is a property of the unperturbed flow and not of the perturbation itself.

When dissipation is present, the situation is remarkably different. The parameter space ($\bar{m}, \bar{n}, \bar{l}, \bar{q}$) is four dimensional, (although the diagonal fold symmetry again effectively removes one dimension, so that the problem has only three independent physical degrees of freedom). However, the characteristic frequencies for dissipative fluids consist not only of the Hoiland, Schwarzschild and Solberg ones (which are the same as for the non-dissipative case) and a few frequencies which correspond to unconditionally stable viscous and thermal perturbations, but also include some frequencies of the general type:

$$\Omega_D^2(k_r, k_z) = f(\rho, T)[k^2(\nabla\Omega)^2 - 2(\vec{k}\cdot\nabla\Omega)^2] \tag{2}$$

It is obvious that now the quadratic form Ω_D^2 is *indeterminate*, which implies that there is no general stability criterion independent of the wave vector. Formally a local, linear analysis always indicates the existence of unstable modes. This does not mean that thick accretion disks are viscously or thermally unstable, but only points to the need for nonlinear, global methods. Because an analytic approach may be possible only in rather simple idealized situations (e.g. isothermal flows) future progress in understanding the stability and pulsation properties of dissipative thick accretion disks depends on developments in numerical hydrodynamics: a two dimensional, time dependent, dissipative, relativistic hydrodynamical code is needed which is able to handle shocks. (See Abramowicz, Henderson and Ghosh 1983 for a quasi-stationary approach to the problem.)

Analytic work by Blandford, Jaroszyński and Kumar (1985) suggests that some of the axially symmetric, viscous instabilities of thick accretion disks will lead to redistribution of entropy in such a way that the resulting configuration is either barotropic (surfaces of constant pressure and density coincide) or gyrotropic (surfaces of constant entropy and specific angular momentum coincide). The gyrotropic configurations have been introduced on general grounds by Bardeen (1973) and Abramowicz (1974) and then studied in the context of thick accretion disks by Paczyński and Abramowicz (1982) and Różyczka and Czerny (1982). They are characterized by strong energy transport which is convective rather than radiative.

8.2 Local stability analysis of thin and slim accretion disks ($\tilde{k} = \infty$) with respect to axially symmetric perturbation ($m = 0$)

The stability of thin accretion disks is a classical subject, discussed in many text books and review articles. The short summary below describes the subject in a way (see Abramowicz, Lasota and Xu 1986, Abramowicz 1987) rarely used by other authors. It relates the stability of the thin (and slim) accretion disks to the slope of the $\dot{M}(\Sigma)$ curve, and starts with an

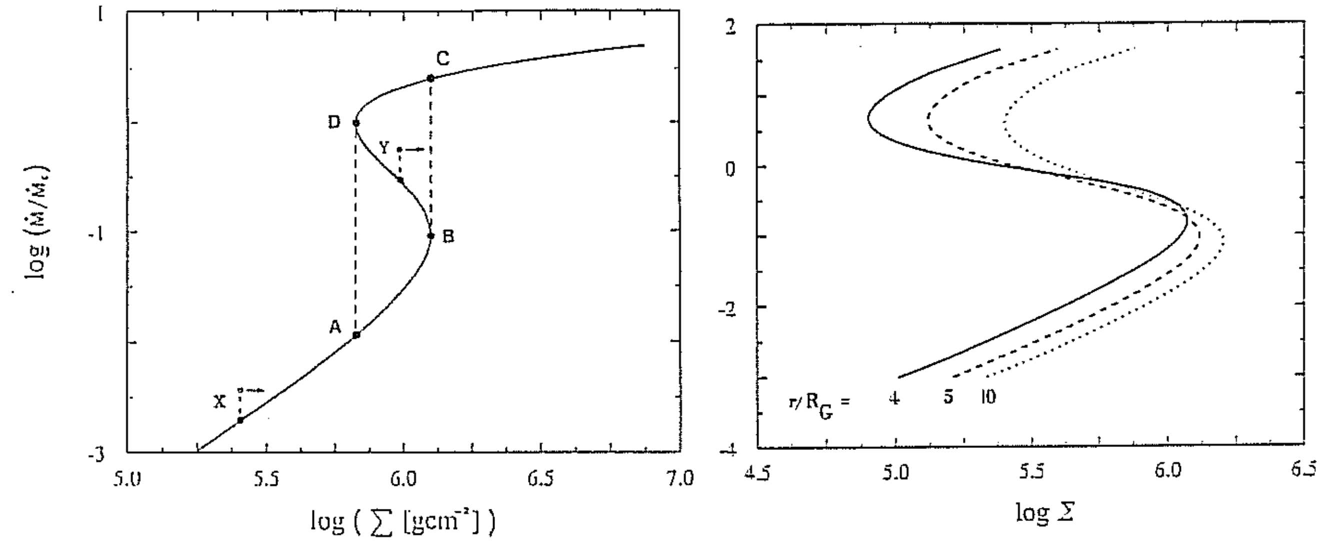

Figure 1: The function $\dot{M}(\Sigma)$ for equilibrium sequences

argument which, although not quite formal, gives a quick insight into the nature of the problem (c.f. Bath and Pringle 1982). Consider a sequence of equilibrium thin accretion disk models with fixed radius, mass of the central object and microphysical properties (equation of state, opacity, α viscosity). Such a sequence depends on only one parameter, $\dot{M}$ (accretion rate): all of the physical properties of the disk, including the surface density Σ, are functions of $\dot{M}$ only. Figure 8a shows the $\dot{M}(\Sigma)$ curve for a particular equilibrium sequence. The points X and Y (open circles) which lie above the equilibrium sequence represent perturbations of the equilibrium models indicated by the black dots. Thus, in both cases, the perturbed models have accretion rates which are too high, $\dot{M}$ (perturbed)$>$ $\dot{M}$ (equilibrium). They are oversupplied with matter and so their surface densities must increase shifting them to the right in the diagram as indicated by the arrows. This brings model X, (which is connected with a positive slope of the $\dot{M}(\Sigma)$ curve) back towards equilibrium, indicating that it is stable. However, model Y goes further away from the equilibrium curve and so is unstable. Thus, models on the positive slopes of the $\dot{M}(\Sigma)$ curve are stable, while those on negative slopes are unstable. It is convenient to introduce (Piran 1978) the phenomenological parameters $\mathcal{K}$, $\mathcal{L}$, $\mathcal{M}$, $\mathcal{N}$ which describe dissipative processes:

$$\begin{aligned} \mathcal{K} &= (\frac{\partial ln Q^-}{\partial ln h})_\Sigma \qquad & \mathcal{L} &= (\frac{\partial ln Q^-}{\partial ln \Sigma})_h \\ \mathcal{M} &= (\frac{\partial ln Q^+}{\partial ln h})_\Sigma \qquad & \mathcal{N} &= (\frac{\partial ln Q^+}{\partial ln \Sigma})_h \end{aligned} \tag{3}$$

Here Q^+ and Q^- are the total heating and cooling rates respectively. It is assumed in most of the literature that Q^+ is due to viscous processes only. Chakrabarti et al. (1987) have discussed how the thermonuclear heating might affect the stability of accretion disks.

Quite generally, one can prove (Abramowicz, Lasota and Xu 1986) that the slope of the $\dot{M}(\Sigma)$ curve is related to Piran's coefficients by

$$\frac{d \log \Sigma}{d \log \dot{M}} = \frac{1}{2} \frac{\mathcal{K} - \mathcal{M}}{\mathcal{K}\mathcal{N} - \mathcal{M}\mathcal{L}} \tag{4}$$

The general criteria for thermal and viscous stability found by Piran (1978) are also related to these coefficients:

$$\mathcal{K} - \mathcal{M} > 0 \qquad\qquad \frac{\mathcal{K}\mathcal{N} - \mathcal{M}\mathcal{L}}{\mathcal{K} - \mathcal{M}} > 0 \tag{5}$$

Thus, the stability of the models is connected with the slope of the $\dot{M}(\Sigma)$ curve and the turning points of this curve correspond to changes in stability. One can show that the existence of the turning points is always connected with strong non-linearities in the physical functions which (implicitly) describe Piran's coefficients (Abramowicz, Lasota and Xu 1986). This typically happens when a small change in some parameters of the flow causes a change in the physical mechanism of cooling or heating. For example, the very strong dependence of opacity on temperature close to hydrogen ionization ($T \approx 10^4 K$) causes the $\dot{M}(\Sigma)$ curves (at all relevant radii) to bend twice, forming characteristic S-curves, similar to those shown in Figure 8b (taken from Abramowicz, Czerny, Lasota and Szuszkiewicz 1988).

Bath and Pringle (1982) were the first to notice the similarity between this situation and the one familiar in non-linear dynamics, where an S-shaped phase portrait of a system indicates a possibility of a limit cycle behavior. If the accretion rate fixed by some external conditions lies in the unstable range (the middle branch of the S-curve with negative slope), then stationary accretion is impossible. Consider point A in

Figure 8a. The accretion rate there is smaller than the supply rate causing local oversupply and an increase of surface density. The disk (at this fixed radius) therefore evolves in the direction indicated by the arrow up to point B from which further evolution is only possible after a jump to C. Here, however, the accretion rate is higher than the supply rate. The surface density now decreases and the disk evolves down to point D where another jump (to A) must take place, closing the cycle. Recently many authors (e.g. Meyer and Meyer-Hofmeister 1981, Papaloizou, Faulkner and Lin 1983, Smak 1984) have studied how this *local* behavior can translate into a global disk response, in connection with theoretical modelling of dwarf nova outbursts. (A review of both observations and theory has been given in an excellent, short article by Smak 1984). These studies today constitute the best check of accretion disk theory, which agrees quite well *quantitatively* with observations of dwarf novae whereas, for AGN, the agreement is mostly *qualitative*. Several authors have proposed that the dwarf nova mechanism might be relevant for AGN variability (e.g. Lin and Shields 1986), but Clarke in her unpublished 1986 Oxford Ph.D. thesis has shown that modulation of the accretion rate due to operation of this mechanism in outer parts of accretion disks, relevant for AGN, will be completely smeared out by the slow viscous response of the material located closer to the hole and no luminosity variation will result. This is because the ratio t_t/t_v is typically three orders of magnitude smaller for AGN than for dwarf novae.

In the case of the standard disk model (opacity due to electron scattering, viscosity given by the Shakura-Sunyaev α) Piran's coefficients are given in terms of β, (the ratio of the gas pressure to total pressure) by $\mathcal{K} = 4(1+\beta)/(4-3\beta)$, $\mathcal{L} = -\beta/(4-3\beta)$, $\mathcal{M} = 2$, $\mathcal{N} = 1$. Together with the criteria (6), this implies that there will be thermal and viscous instabilities when $\beta < 2/5$,(i.e. for the radiation pressure supported standard thin accretion disks). In the limit $\lambda/h \gg 1$, the growth time of the unstable thermal modes is independent of wavelength: $\tau = (t_t/30)(56 - 57\beta - 3\beta^2)/(2/5 - \beta)$. This type of instability was discovered and studied by Pringle, Rees and Pacholczyk (1973), and Shakura and Sunyaev (1976). In the same limit, the growth time for the unstable viscous mode is: $\tau = t_v(\lambda/r)^2(3/10)(2-3\beta)/(2/5-\beta)$. This type of instability was found by Lightman and Eardley (1974) and Lightman (1974).

Abramowicz and Lasota suggested in 1985 in connection with the cyclic outbursts in NGC 1566 observed by Alloin et al., that these $\beta < 2/5$ instabilities, together with the advective heat loss induced by Roche lobe overflow, would cause the $\dot{M}(\Sigma)$ curve to bend twice, for all small radii and for accretion rates typical of slim disks. They suggested also that the resulting S-shaped relation between $\dot{M}$ and Σ would cause quasi-periodic luminosity changes, as in the case of dwarf novae, but with a period of a few years. The first suggestion was formally demonstrated to be true by Abramowicz, Czerny, Lasota and Szuszkiewicz (1988). In Figure 8b we show the S-shaped $\dot{M}(\Sigma)$ curves calculated numerically in this work (which used a physically realistic slim disk approach). It is still unknown whether the nonlinear, non-stationary response of a disk with an accretion rate corresponding to the unstable regime (middle branch) will be quasi-periodic. Preliminary unpublished results of Lasota and Pellat indicate that this is indeed the case.

Unfortunately, many of the results presented in this section depend on the viscosity prescription. For example, if viscous stress is proportional not to the total pressure (as assumed in the standard Shakura- Sunyaev model) but to the gas pressure, the $\beta < 2/5$ intability disappears. The shape of the S-curves also depends on the viscosity prescription, as many authors have noticed (see e.g. Meyer and Meyer- Hofmeister 1983). Abramowicz, Czerny, Lasota and Szuszkiewicz (1988) gave, perhaps, the most dramatic example of this by considering the viscosity law $\alpha = \alpha_0 \exp(-k\dot{M}/\dot{M}_E)$ with $k = const.$ The Shakura-Sunyaev model ($k = 0$) and its modifications ($k = 0.1,\ 1$) are shown in Figure 9. Such a law is not purely phenomenological, but may be caused, for example, by the Papaloizou and Pringle instability, which is strong for small accretion rates (thus producing strong turbulence and viscosity) but switches off at high rates. This instability will be discussed later (in Section 3.4).

3.3 Linear and non-linear stability analysis of the transonic part of thin accretion disks

The most important physical effects in the transonic part of accretion disks are the existence of forbidden regions in the parameter space (connected with the regularity condition at the critical points), the change of angular momentum distribution from almost Keplerian to almost constant, and the advective cooling connected with Roche lobe overflow.

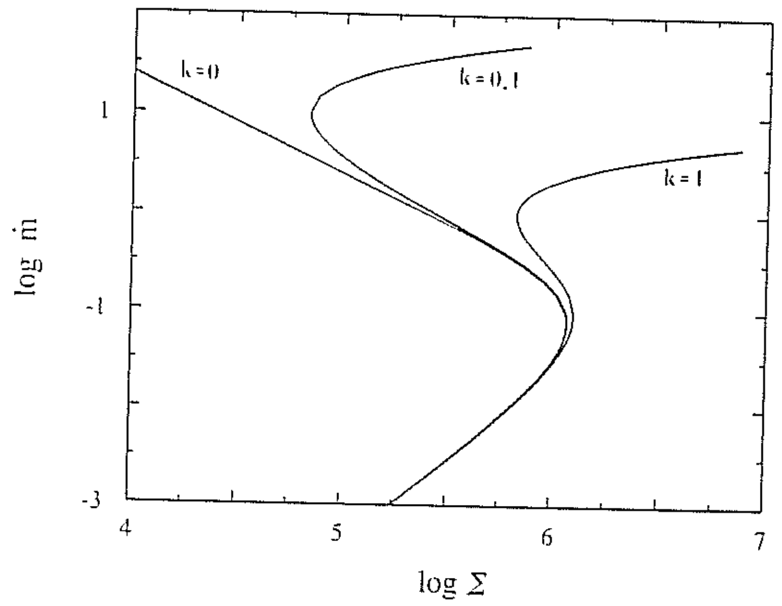

Figure 2: The influence of viscosity on the S-curves

Abramowicz and Zurek (1981) found that in the case of dissipation-free black hole accretion, the forbidden regions separate two physically different regimes. The first one, *Bondi accretion*, contains solutions in which the sonic point is far away from the hole. These solutions resemble spherical accretion of non-rotating matter. The second regime, *disk accretion*, contains solutions with the sonic point close to the hole. This type of flow is similar to that in the innermost parts of thick accretion disks and has no Newtonian analogy. In both the Bondi and disk regimes, the topology of the critical point is of the saddle type. Another acceptable topology for the critical point would be the nodal type; spiral or center topologies are excluded - see Ferrari, Trussoni, Rosner and Tsinganos (1985) for an excellent discussion of this point.

Abramowicz and Zurek suggested that when an astrophysical situation locates a flow in the forbidden region, the non-stationary response of the flow will be *bistable*, oscillating between the Bondi and disk regimes. If true, this suggestion would have an impact on our understanding of the fact that many active galactic nuclei (and their scaled down versions in our Galaxy) indeed show bistable behavior, oscillating between high and low states. Although the suggestion was later supported by other analytic arguments (Abramowicz, Livio and Lu, 1986), numerical methods would be needed in order to give any really firm conclusion. The problem is difficult, because it involves shock formation. Although the existing numerical codes can cope with this, all of the attempts to model bistability have failed because of physical misunderstandings concerning boundary and shock conditions. For example, Hawley (1986) constructed various non-stationary numerical models of transonic flows with shocks, none of which showed the bistability. However, his models covered only a very limited region of the parameter space and they always started from supersonic flow at the outer boundary, while the correct boundary conditions are only consistent with asymptotically subsonic flows.

Muchotrzeb (1983) continued studies of *dissipative*, transonic accretion flows started by Paczyński and Bisnovatyi-Kogan (1981) and herself and Paczyński (1982). She worked in a particular sub-set of the parameter space consistent with the assumption that far away from the central accreting black hole the flow is identical with that given by the Shakura-Sunyaev solution (*Keplerian boundary conditions*) and she found a part of the boundary of the region where globally acceptable transonic solutions of the saddle type exist. She interpreted the existence of such a boundary as an upper limit $\alpha_* \approx 10^{-2}$ for the Shakura-Sunyaev viscosity parameter and suggested that when $\alpha > \alpha_*$ no stationary solution is possible. Matsumoto, Kato, Fukue and Okazaki (1984) cleared up this point by showing that *unstable* nodal type transonic solutions exist beyond the boundary found by Muchotrzeb. In a recent work by Abramowicz and Kato (1988, preprint) an explicit example was given to show that instability is *not* in general connected with nodal topology of the critical point when different viscosity prescriptions are considered. In the same paper, it was shown that stable solutions, in the sense of criterion (7), may be found for any value of α if high accretion rates (which were not considered by previous authors) are allowed in addition to low ones. The fact that the situations at low and high accretion rates are quite different is clearly illustrated in Figure 10 (taken from Abramowicz, Czerny, Lasota and Szuszkiewicz 1988) in which the location of the sonic point is shown for different accretion rates. For small accretion rates any increase in the rate causes the sonic point to move either towards the hole or away from it depending on the value of α, and there is clearly a critical value of α separating the two regimes. However, for high accretion rates there is no obvious reason to define any "critical

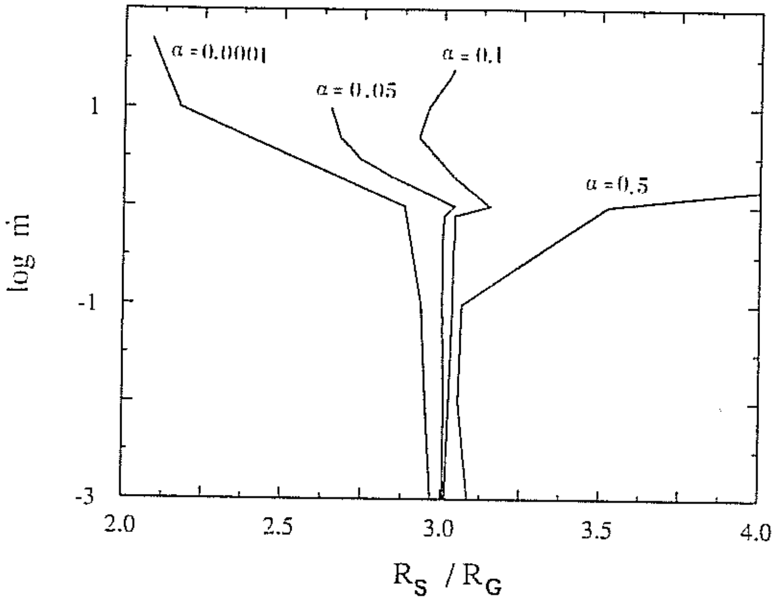

Figure 3: The sonic point position as a function of accretion rate for different α

α".

An instability specific to the transonic part of the accretion flow was first suggested by Muchotrzeb-Czerny (1986) and then studied analytically by Kato, Honma and Matsumoto (1988) and numerically by Matsumoto, Kato and Honma (1988, preprint). They found local instabilities for an isothermal disk when

$$\alpha\Omega(r_c) > \left|\frac{dv}{dr}\right|_c \tag{6}$$

Here the subscript c refers to the critical point. The instability arises when oscillations of the azimuthal component of the viscous force are in phase with the variations of azimuthal velocity, so that the viscous force does positive work on the oscillations. The local oscillations (either stable or unstable) may develop into global trapped ones in the transonic region due to the fact that the epicyclic frequency $\chi^2 = (2\Omega/r)(dl/dr)$ has a maximum close to the transonic region. This is because, as we have already stressed, $l \approx const$ for $r < r_c$, while $\Omega \approx (GM/r^3)^{1/2}$ for $r \gg r_c$. Thus, for both $r < r_c$ and $r \gg r_c$ one has $\chi \approx 0$. A positive continuous function which equals zero at both ends of a region must have a maximum somewhere in this region. Okazaki, Kato and Fukue (1987) considered a perturbation of an isothermal accretion disk with n nodes in the vertical direction. They found that the radial wave vector component k can be written as $k^2 = (\omega^2 - \chi^2)(\omega^2 - n\Omega^2)/\omega^2 v_s^2$. Because $k^2 > 0$ for radially propagating modes, the above expression shows that local waves with $n = 0$ can propagate in regions where $\omega > \chi$. Knowing that $\Omega > \chi$ and denoting by χ_{max} the maximum of the epicyclic frequency and by r_1 and r_2 the smaller and larger roots of the equation $\omega = \chi$, one concludes that waves with $n \neq 0$ can propagate in the region between r_1 and r_2 when $\omega < \chi_{max}$. This suggests that there will be global oscillation modes trapped in the region between r_1 and r_2. The pulsation periods for these modes cover some range close to about one day for disks around a $10^8 M_\odot$ black hole.

There is also a non-propagating mode located exactly at the sonic point. When criterion (7) predicts instability, this mode also becomes unstable. However, in the non-linear regime, the amplitude of the unstable mode saturates as shown in Figure 11, taken from a poster presentation by Kato and Matsumoto at the 20^{th} Yamada Conference. After initial exponential growth in the linear regime, the mode saturates and its further evolution is determined by non-linear interaction with another mode, which

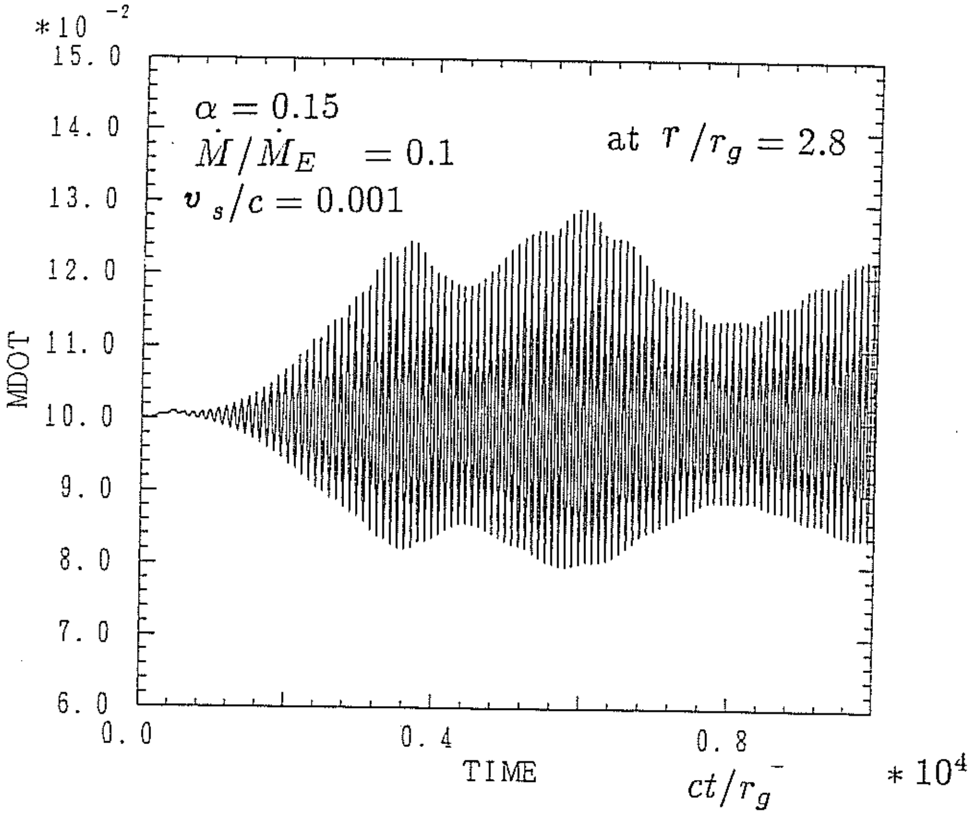

Figure 4: Non-linear evolution of the unstable mode located at the sonic point

is trapped in the region of the epicyclic frequency maximum.

In the above mentioned work it was assumed that no shocks are present. One might think that the presence of shocks would permit stationary solutions to exist in at least some parts of the forbidden regions. This is not true, however. Abramowicz and Chakrabarti (1988, preprint) have recently found all of the possible solutions corresponding to rotating, stationary, axially symmetric, polytropic, dissipation-free accretion flows which could have shocks with efficient cooling. Solutions with or without shocks have exactly the same forbidden regions. The same conclusion holds for all types of shock and for all accretion flows with small dissipation. The very important conclusion from this work is that in all astrophysical situations in which the flow properties are fixed far away from the black hole by some outside conditions, the accretion process *cannot be* stationary if the dissipation is small.

8.4 Global, non axially symmetric, linear and non-linear stability analysis for thick disks with no dissipation

Papaloizou and Pringle (1984) demonstrated that non self-gravitating fluid rings or tori in which all of the fluid flowlines are perfect circles around a spherically symmetric center of gravitation are unstable with respect to global, linear, adiabatic, non-axially symmetric perturbations. When the ratio of the ring cross-sectional radius r_0 to its orbital radius R_0 is not large, this instability grows on the dynamical timescale appropriate for the ring's physical center (pressure maximum). The original Papaloizou and Pringle's arguments are complicated and are not easy to follow. We shall describe them here using results of Blaes (1985) who found a simple and elegant analytic solution for the normal modes of pulsation in the case of a slender ring ($r_0/R_0 = \beta \ll 1$) with constant specific angular momentum. The solution is based on the fact that in the limit $\beta = 0$ there is an additational symmetry in the problem: all of the geometrical and physical properties of the slender ring depend only on distance from the circle of pressure maximum $r = r_0$, $z = 0$. This distance is denoted by η and normalized so that $\eta = 1$ corresponds to the surface of the ring. The angular coordinate θ is orthogonal to the η coordinate. For a polytropic ring the isobaric surfaces are perfect circles, $p(r, z) = p(r_0, 0)(1-\eta^2)^{n+1}$, and there is no shear since the angular velocity is constant, $\Omega(r, z) = \Omega(r_0, 0) + O(\beta^2)$. The unperturbed slender ring structure does not depend on the time t, the azimuthal coordinate φ, or the angular coordinate θ. The normal mode solution to the perturbation equation (with the appropriate boundary conditions at $\eta = 0$ and $\eta = 1$) can be thus written as $\bar{Q}_i(\eta)\exp(i\omega + im\varphi + ik\theta)$, where the integer k gives the number of nodes in the θ direction. Blaes (1985) found that the amplitude of the perturbation $\bar{Q}_i(\eta)$ can be expressed in terms of Jacobi polynomials. The frequency of a special mode which corotates with the flow (i.e. which has pattern speed $Im(\omega)/m$ equal to the rotation speed of unperturbed flow Ω) and which has no nodes in either the θ or η direction, is given by

$$\omega = -\Omega_0 m \pm i\beta\Omega_0 m[3/2(n+1)]^{1/2} + O(\beta^2) \qquad (7)$$

where $\Omega_0 = \Omega(r_0, 0)$. This corotating mode is obviously unstable, as the solution with the minus sign has $Im(\omega) < 0$. All other (non-corotating) modes remain stable for small β. The growth time of the unstable mode is of the order of the dynamical time $\tau = 1/|Im(\omega)| \approx (1/\Omega_0)(1/m\beta)$. For any nonzero β one can find m large enough to make $\tau < (1/\Omega_0)$, i.e. to give dynamical growth of the unstable mode. This is precisely the *principal* mode connected with the Papaloizou and Pringle (PP) instability. A physical explanation for it (suggested by Goldreich, Goodman and Narayan 1986, and independently by Blaes and Glatzel, 1986) points out that the surface gravity waves at the inner and outer edges of the ring couple across corotation and, since they have energy and angular momentum with opposite signs, the waves grow by exchanging these conserved quantities. Abramowicz, Blaes and Ghosh (1987) constructed an example of a pulsating cylinder which admits no surface gravity waves, but is nevertheless PP unstable. The PP instability in this case is similar to the classical Kelvin-Hemholtz instability of a shear layer (see e.g. Chandrasekhar 1961). Goldreich and Narayan (1985) gave another useful interpretation of the PP instability using the WKB approximation. A wave incident on the corotation region from the inner parts will be partially reflected and partially transmited. The incident and reflected waves have negative angular momenta (relative to the equilibrium flow) since their pattern speeds are lower than Ω but the transmited wave has positive angular momentum. Because of angular momentum conservation, the outward angular momentum transfer to the transmitted wave causes a reduction in the angular momentum of the reflected wave, which is therefore amplified. A reflecting boundary on either side of corotation is needed to provide a feedback so that the amplitude of the wave grows. This picture stresses the rôles of the corotation amplifier and reflecting boundary conditions, and is thus similar to the spiral density wave theory (Mark 1976). It has, however, only a limited validity because in real situations perturbations cannot always be treated as waves. (For more details see Drury 1985, Blaes unpublished 1986 SISSA Ph.D. thesis, and Kato 1988, preprint.)

The principal mode stabilizes (for slender tori) when the angular momentum profile is steep enough. Assuming $l = l_0 r^{2-q}$, stabilization occurs, as Goldreich, Goodman and Narayan (1986) have shown, for $q > \sqrt{3}$. As the torus become thicker, the surface interaction modes progressively stabilize, with the low m modes remaining unstable longest, but in addition to these modes there are also (slower) unstable acoustic modes (Glatzel 1987). Very recently Sekiya and Miyama from Kyoto found that for flows with finite radial thickness, the principal unstable mode (due to edge waves) actually does not stabilize for $q > \sqrt{3}$, but instead extends all the way down to Keplerian flows, albeit with smaller growth rates (Blaes, private communication).

Although there are important topological differences between non-accreting slender rings and thick accretion tori (as stressed by Abramowicz, Blaes and Lu 1986) the general opinion was, until recently, that the instability of rings implies instability of thick disks. This opinion has changed because of several important recent developments in studies of the PP instability. First of all Blaes (1987) has demonstrated (for two dimensional models of tori around black holes), that even a small amount of accretion may stabilize the PP modes, essentially because the perturbations are advected inside the *sound horizon* by the transonic accretion flow before they have a chance to grow. In the context of spherical, isentropic black hole accretion, the stabilizing effect of the sound horizon was known a long time ago (Moncrief 1980). Goodman and Narayan (1988) found that moderate self-gravity also eliminates the PP instability in two dimensional cylinders and slender tori. In a very interesting recent paper, Boss (1988) has discussed the non-linear evolution of PP modes with low m in three dimensional tori with $\beta \gg 1$ and found that such tori are PP stable. Although this result was not totally unexpected, as it agrees with an extrapolation of earlier results obtained by Frank and Robertson (1987), Kojima (1986) and Zurek and Benz (1986), some of the technical (numerical) details of Boss's paper are not clear enough to justify the definite conclusion that very fat tori are PP stable. (Of course, only such very fat tori are astrophysically relevant). In our opinion the final proof of this point should be based on analytic rather than numerical methods. It is, perhaps, worth noticing that infinitely fat, constant angular momentum tori are spherically symmetric, except for a singularity on the rotation axis. This asymptotic symmetry may help for separating the variables in the pulsation equation, in a similar way as the asymptotic symmetry helped in the case of the infinitely slender torus. Numerical methods are not sufficiently advanced for studying another astrophysically important problem - the nonlinear response of the torus to instability and to the development of turbulence. Preliminary results have been obtained (for very simple configurations and evolutions covering just a few dynamical timescales) by Zurek and Benz (1986), Hawley (1987), Blaes and Hawley (1988), and Boss (1988). A semi-analytic approach by Glatzel (unpublished) shows that viscosity triggered by turbulence may seriously weaken the PP instability. The simple analytic method of Hanawa (1988, Max-Planck- Institut preprint), who investigated PP instabilties of Keplerian disks taking into account quadratic terms in the perturbation, shows (not surprisingly) that interaction of *some* modes enchances the instability. Radically new approaches, both analytic and numerical, are needed in order to treat the problem of turbulence and convection in connection with the PP instability. (See e.g. Rieutord 1988, preprint, submitted to *Journal of Fluid Mechanics*). The stability of thick, ion-pressure supported tori needs to be examined with methods different from the purely hydrodynamical ones relevant for studying the PP instability of tori supported by radiation pressure (or ideal gas pressure). For ion tori, electrons and ions are decoupled (they have different temperatures, $T_i \gg T_e$), and therefore plasma effects are important. Begelman and Chiueh (1988, preprint) discovered a plasma instability which may lead to thermal coupling between ions and electrons with the growth being on a timescale shorter than the Coulomb coupling time. The unstable modes are "electron-acoustic" waves, which propagate in a direction orthogonal to the magnetic field lines. It could be that there is a relation between this (or similar) plasma instabilities and the PP instability. Antonuccio (unpublished) noticed a few years ago that in PP unstable tori the fluid flowlines close on themselves. Flowlines which close on themselves induce *phase coherence* for perturbations, and this is a factor which is relevant for instabilities of toroidal plasma configurations in tokamaks. It is known that these instabilities may be cured by forcing the flowlines to be open. This may be done by introducing an additional rotation, in direction orthogonal to the general circular flow, and with the additional angular velocity being an irrational multiple of the angular velocity of the circular flow. Antonuccio argues that the flowlines in radiation pressure supported tori may be made open by, for example, meridional circulation or by the influence of magnetic fields, and that this could be very important for stability.

Sophisticated mathematics and advanced numerical methods are not the only important techniques for understanding the PP instability. The most crucial information may, ironically, be provided by very classical astronomical observations: accurate spectrophotometry and photometry of the galactic object SS433, systematically collected over many years by a few independently working groups (Antokhina and Cherepashchuk 1985, Kemp et al. 1986, Wagner 1986), suggest very strongly that this object consists of a $10M_\odot$ black hole with an associated thick accretion disk. This suggestion arises from the use of standard techniques which astronomers have been using for years for eclipsing binaries to determine from spectral and luminosity changes during eclipses, the masses, shapes and luminosities of the components of the system. It is *not*, therefore, model dependent. Abramowicz, Calvani and Madau (1987) have argued that this conclusion agrees with all other observational data on SS433, which was previously interpreted only in a *model dependent way* by theoreticians, who had a particular model in mind. (See also Zwitter and Calvani 1988, SISSA preprint). Thus, it seems that there is *an observational proof* that astrophysically relevant thick accretion tori are PP stable.

8.5 Some other intrinsic accretion disk instabilities (connected with self-gravity)

Abramowicz, Calvani and Nobili (1983) noticed that, since the mass and angular momentum of the central black hole increase as a result of accretion, the location of the Roche lobe must change and this changes the amount of the Roche lobe overflow. In the case of an increase there will be a runaway instability, as growth of the hole increases the overflow and the overflow will speed up the growth of the hole. This happens when the ratio of the mass of the torus to the mass of the hole is greater than ≈ 0.01. Wilson (1984) rediscussed the problem and found no such runaway instability. However, neither Abramowicz et al. nor Wilson have taken proper account of the self-gravity of the torus which is crucial to the problem, but is difficult to calculate. Lanza (unpublished 1986 SISSA Ph.D. thesis) and Brandt and Lanza (1988) report preliminary results in developing a general relativistic hydrodynamical code which will be able to compute self-gravitating tori around rotating black holes. If the runaway instability exists, it may cause a typical AGN to go through a sequence of long quiescent states interrupted by accretion bursts. Timescales depend strongly on the dimensions of the torus and of the accretion rate but for some reasonable choices may be astrophysically relevant. Self-gravity also plays an important role in the model suggested by Paczyński (1978) in which the disk cools and increases its density until, when $\rho \approx M/r^3$, local instabilities develop which are similar to the Jeans instability. If the optical depth is large enough so that the cooling time is much longer than the orbital one, the instabilities will increase the velocity dispersion in the gas, and this will produce turbulence, thereby enchancing viscous stresses, which in turn produce heat. This heating will cause expansion and a decrease in the disk density. The disk will either oscillate between a hot expanded state in which self-gravity is not important and a cool, collapsed state in which it is dominant, or it will settle down at the marginally stable state (as indeed Paczyński assumed) in which the cooling and heating rates are exactly equal. Oscillations may occur on the local thermal scale t_t. Alternatively, for small optical depth, condensations would form and this might trigger star formation. In this picture, elaborated by Bailey (1982), the lifetimes of AGN consist of long, quiet periods interrupted by short active ones, with timescales being difficult to estimate (see Abramowicz 1982 for a short discussion of this paper).

The paper by Goodman and Narayan (1988), which we have already discussed in connection with the PP instability, also contains other results and other useful references concerning self-gravity of accretion disks.

3.6 Other possibilities (midway, supply and atmospheric variability)

In this section we discuss possible mechanisms of variability which are not intrinsic to the accretion processes. We start from a really disturbing one - that variability might not be a signature of the physics of AGN at all, but might originate "midway" due to influence of matter between us and the source. We know that, at radio frequencies, only about 10 percent of the observed variability of AGN is intrinsic, and that the rest should be attributed to midway inhomogeneities of the intergalactic and galactic medium, and of magnetic fields. This is not very disturbing, as radio data are not a good probe of the innermost parts of accretion disks anyway. However, it has been suggested recently that a large fraction of quasars may be gravitationally microlensed and that the resulting time dependent amplification may explain a large part (or, at least, some part) of the variability of active galactic nuclei also at frequencies higher than the radio ones (Ostriker and Vietri 1985, Schneider and Weiss 1985, Paczyński 1986). The microlensing is provided by individual stars in an intervening galaxy. For a moderate number of microlenses, typical theoretical light curves show sudden, *double peaked* outbursts in which the rise and decay times are quite symmetric. The bursts have very characteristic U-shapes between the peaks, and are separated by long quiescent periods. A quasi-periodic bursting may easily occur by chance. The predicted timescales for variation due to microlensing range from weeks to centuries, depending on the impact parameter and the relative velocities of the lens and source on the sky. In theoretical models dense star fields in the lensing galaxy are found to produce irregular flickering without much change in apparent magnitude and without periodicities. This agrees, very nicely, one might think, with the fourth and first types in the Rosemary Hill classification. There are, however, some important detailed differences (cf. Abramowicz 1987): (a) Variability of the intensity of the spectral lines cannot be explained by lensing, especially when some other lines do not change or when, as somethimes happens, there is a correlation between variability in lines and in the continuum. (b) Gravitational lensing cannot explain *secondary maxima* or the fact that many outbursts have a much shorter rise time than decay time. These features are characteristic of damped oscillations caused by an instability. Double peaked outbursts are not common. (c) Variability of active galactic nuclei and X-ray sources within our Galaxy show many similarities when the necessary scaling factors are introduced. Sources in our Galaxy are obviously not lensed. (d) The light curve of 3C 345, shown in Figure 3, was considered as a particularly good example of possible lensing by Schneider (Max-Planck-Institut Seminar, 1986). It indeed shows a succession of strong bursts, which could be interpreted (although not uniquely) as double peaked, U-shaped and symmetric. This would point to a moderate number of microlenses. After 1975, however, there have been no bursts, but only an irregular flickering with large amplitude (Kidger and Beckman, 1986). This rules out lensing as the mechanism since that would imply a sudden change of the number of stars in the lensing galaxy in 1975. If the angular size of the source is much larger than the scale of deflection then microlensing is unimportant. If the UV bump emitting region (see Section 1.4) has a size of $\approx 10^{16}$ cm or smaller, microlensing can occur, but cannot explain variability on the scale of months or years which would imply a size of $\approx 10^{17}$ cm. Therefore, although gravitational lensing of quasars by individual galaxies, reviewed in a very complete and scholarly series of lectures by Blandford and Kochanek (1987, Caltech preprint), or even by *clusters* of galaxies (there is a fascinating new discovery of a "luminous arc", see e.g. Paczyński 1987, or the lecture by Fort 1988 at the ESO/CERN Conference in Bologna) is well established, the rôle of microlensing in AGN variability is unknown. The same conclusion has been reached by Schneider (1988, Max-Planck-Institut preprint) in his recent review of the subject.

Variability might be caused by variation in the mass supply to the disk. Abramowicz, Blaes and Turolla (unpublished) used a numerical, quasi-stationary model of AGN evolution to show that matter stored in a large torus around a supermassive black hole is not sufficient to support quasar-like activity. Continuous supply from the hosting galaxy is needed. The galaxy can supply fuel to its active nucleus either through mass loss from stars, or by processes of stellar collisions, captures and disruptions, which may be very effective if the central black hole is surrounded by a dense star cluster. Tidal interaction with a nearby galaxy may also trigger mass supply (Lin, Pringle and Rees 1988) and the same is true for hypothetical close pairs of supermassive black holes. Hills (1975), Frank (1979) and others have studied the tidal capture and disruption of stars by a black hole. The main result is that a star with density ρ will be broken apart by a black hole with mass M if it passes within a distance $r \approx (6M/\pi\rho)^{1/3}$. Once all of the stars whose orbits pass close to the hole have been destroyed, further capture can only occur when dynamical interaction between the stars in the cluster can repopulate the close orbits, and this happens on a time scale longer than 10^{10} years. Direct collisions between stars in a dense cluster are also important. The capture processes can be an efficient supply mechanism only for a low mass central hole with $M < 10^{6} M_{\odot}$. Carter and Luminet (1982) argued that a star in a very close orbit will experience tidal compression and subsequent thermonuclear detonation (see also Luminet and Carter 1986, and Luminet (1987) for a review). Very recently, tidal thermonuclear detonation has also been discussed by Hills (1988) and Rees (1988). Beckman and Kidger (1986) studied statistically the resulting variation in AGN luminosity due to this process, but no *quantitative* analysis of *individual* cases has been performed. Thus, a varying supply rate is still an important theoretical possibility but has only very limited observational support. Sillanpää et al. (1988) argued that quasi-periodic bursts in the light curve of OJ 287 may be explained if the object is a binary black hole. They constructed a model consisting of two supermassive black holes, with masses $2 \times 10^7 M_\odot$ and $5 \times 10^9 M_\odot$, closely orbiting each other on an elliptic orbit and each having its own accretion disk. At each of the close encounters (which happen at about 11 year intervals) enchanced accretion is triggered producing the observed burst. However, the amplitudes calculated from the model are much smaller than those observed, and also the observed bursts are similar to those of many other BL Lac objects (Barbieri et al. 1988, preprint) so that, on purely statistical grounds, the binary explanation for OJ 287 seems unlikely to be correct.

Variability of AGN might be connected not with unsteady accretion processes, but with some "atmospheric" phenomena, occurring at much greater distances from the central black hole and being governed by radiation transfer instabilities. An important example of this possibility was discussed in a series of papers by Begelman, McKee and Shields (1983a, b). The main ingredient of the idea is that the X- ray radiation from the hot, innermost region of the disk may be absorbed by the much cooler outer parts which heat up, forming a tenuous corona and giving rise to a strong wind. The authors assume the disk to be geometrically thin and consider cooling and heating of the wind and corona by Compton scattering. The wind takes with it some of the matter at large radii, so that the amount of matter arriving at smaller radii, where the X-rays are produced, decreases. This then decreases the X-ray luminosity providing a feedback mechanism. Depending on the parameters, the feedback may cause either stable, or unstable, oscillations with a typical timescale of 10^4 years which is much too long to explain any of the AGN variabilities discussed in this review.

Radiation transfer instabilities with much shorter timescales can occur due to the existence of e^+e^- pairs in AGN "atmospheres" (Svensson 1987, Fabian et al. 1986, Sikora and Zbyszewska 1985, Zdziarski and Lightman 1987, Ghisellini 1988, and others). Pair creation is possible, because the energy per accreted particle exceeds the rest mass of the electron. The dominant mechanism for pair creation is likely to be photon-photon collisions in which γ-rays of energy $\epsilon > m_e c^2$ (produced by energetic particles) collide with X-rays of energy $\approx \epsilon/2$. This happens when the compactness (luminosity/size) parameter, $l_* = L\sigma_T / R m_e c^3$, is larger than about 20π (Guilbert, Fabian and Rees, 1983). Here σ_T is the Thomson cross section. The compactness parameter for super-Eddington sources is greater than

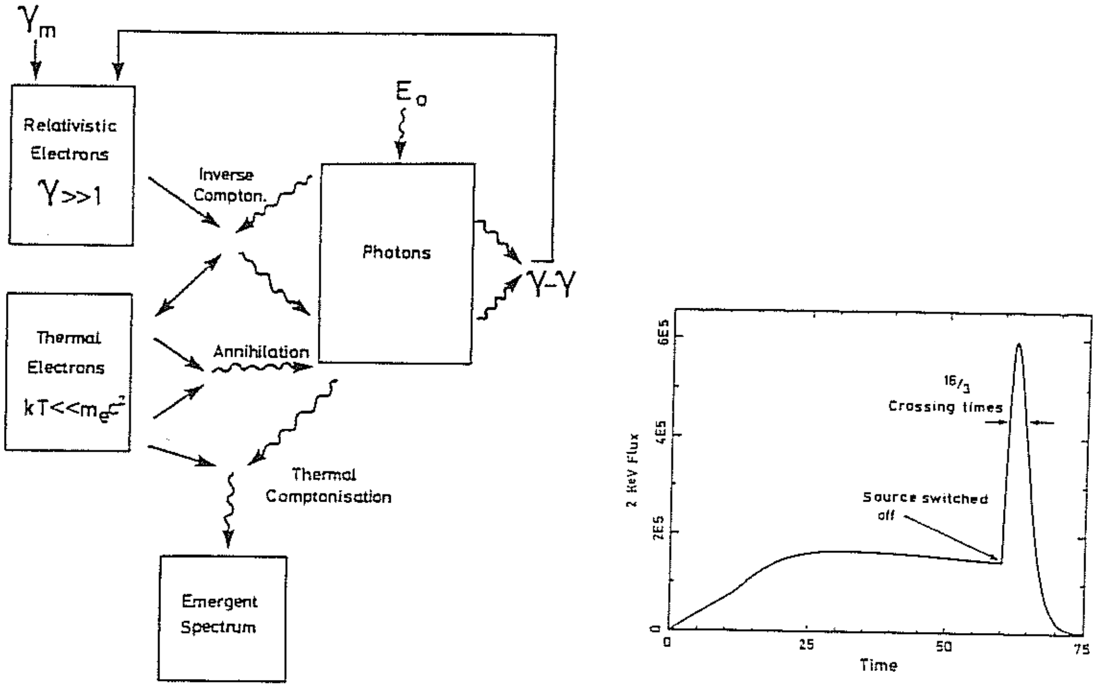

Figure 5: Illustration of Fabian's arguments

4000 and thus many AGN are compact in the above sense (Cavaliere and Morrison, 1980). Fabian (1987) proposed a variability mechanism, based on a chain of processes schematically shown in Figure 12, which is taken from his article. The shortest variability timescale potentially visible to an observer is the cooling time for an electron, which may be much less than the light travel time across the source region R/c. However electron scattering in a cooled pair plasma of Thomson optical depth τ_T will damp all variations up to the timescale $\tau_T R/c$. Large changes in input power can cause large changes in τ_T through increased pair production or annihilation and this has important consequences for the luminosity and for the variability timescale. When the source is ”switched on” electron scattering in cooled pairs impedes the outflow of X-rays so that the spectrum builds up over a time $\tau_T R/c$. At ”switch off”, pair anihilation controls the process, which can then proceed on a much shorter timescale. A large variation in input power can thus produce a slow X-ray increase and rapid X-ray decrease, which can be preceded by a brief burst of emission (Figure

12). This model (and other similar ones) depend critically on unknown theoretical parameters, and direct comparison with observations is not yet possible.

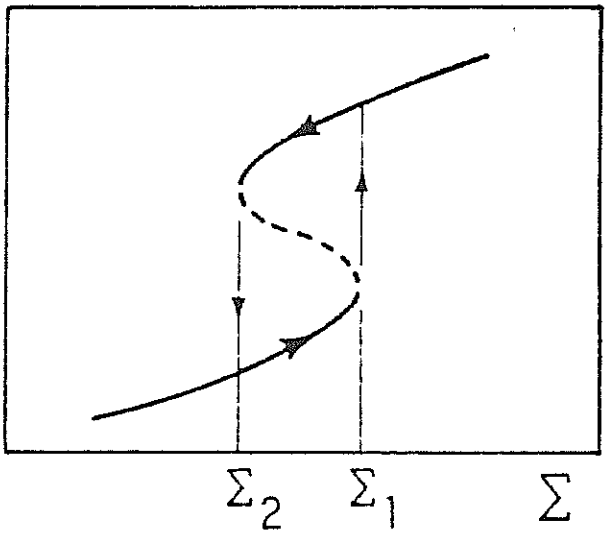

Figure 1: The limit cycle operating in dwarf novae

9. Discussion, conclusions and ... crazy thoughts

I would like to finish my thesis not giving the general conclusions but telling few thoughts, single thoughts which help us to understand better the results I have got.

We have discussed in Chapter 7 that Bath and Pringle (1982) have noticed the similarity between the S-curves obtained in dwarf nova case and the ones known in non-linear dynamics.

Figure 1 shows how an S-shaped relationship between flux and surface density can give rise to the observed behaviour of dwarf novae.

9.1 Examples of S-curves not necessarily connected with astrophysical objects.

a) The Hamilton-Jacobi equation and a typical singularity of its solution

$$\frac{\partial S}{\partial t} + H(\frac{\partial S}{\partial \mathbf{q}},\ \mathbf{q},\ t) = 0. \tag{1}$$

This non-linear first-order partial differential equation is called the Hamiltonian-Jacobi equation. The Cauchy problem for this equation is

$$S(\mathbf{q},\ t_0) = S_0(\mathbf{q}) \qquad \frac{\partial S}{\partial t} + H(\frac{\partial S}{\partial \mathbf{q}},\ \mathbf{q},\ t) = 0. \tag{2}$$

In order to construct a solution to this problem, we look at the hamiltonian system

$$\dot{\mathbf{p}} = -\frac{\partial H}{\partial \mathbf{q}} \quad \dot{\mathbf{q}} = \frac{\partial H}{\partial \mathbf{p}} \tag{3}$$

We consider the initial conditions (see Figure 2):

$$\mathbf{q}(t_0) = \mathbf{q}_0 \quad \mathbf{p}(t_0) = \frac{\partial S_0}{\partial \mathbf{q}}|_{\mathbf{q}_0} \tag{4}$$

The solution corresponding to these equations is represented in $(\mathbf{q},\ \mathrm{t})$ -space by the curve $\mathbf{q} = \mathbf{q}(t)$, which is extremal of the principle $\delta \int Ldt = 0$ (where the lagrangian $L(\mathbf{q},\ \dot{\mathbf{q}},\ t)$ is the Legendre transformation with respect to $\mathbf{p}$ of the hamiltonian function $\mathrm{H}(\mathbf{p},\ \mathbf{q},\ \mathrm{t})$). This extremal is called the characteristic of the problem, emanating from the point $\mathbf{q}_0$

If the value t_1 is sufficiently close to t_0, then the characteristics emanating from points close to $\mathbf{q}_0$ do not intersect for $t_0 \leq t \leq t_1$, $|\mathbf{q} - \mathbf{q}_0| < R$. The action function S_0:

$$S(A) = S_0(\mathbf{q}_0) + \int_{\mathbf{q}_0,t_0}^{A} L(\mathbf{q},\ \dot{\mathbf{q}},\ t)dt \tag{5}$$

is a solution of Cauchy problem (2)

A typical singularity of a solution of the Hamiltonian-Jacobi equation is presented in Figure 3. This Figure shows the multiple-valued "functions" S(q) and p(q) for $t = t_3$.

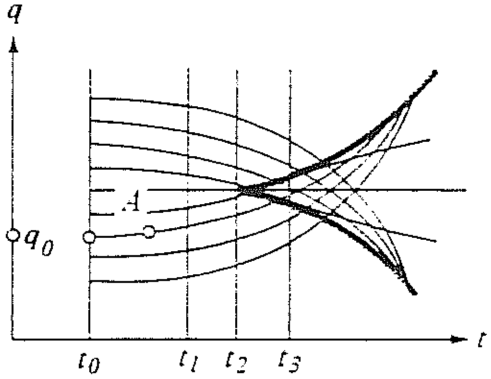

Figure 2: Characteristics for a solution of Cauchy's problem for the Hamilton-Jacobi equation.

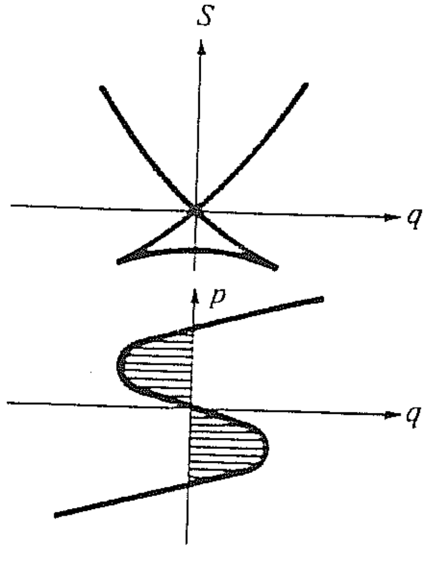

Figure 3: A typical singularity of a solution of the Hamiltonian-Jacobi equation.

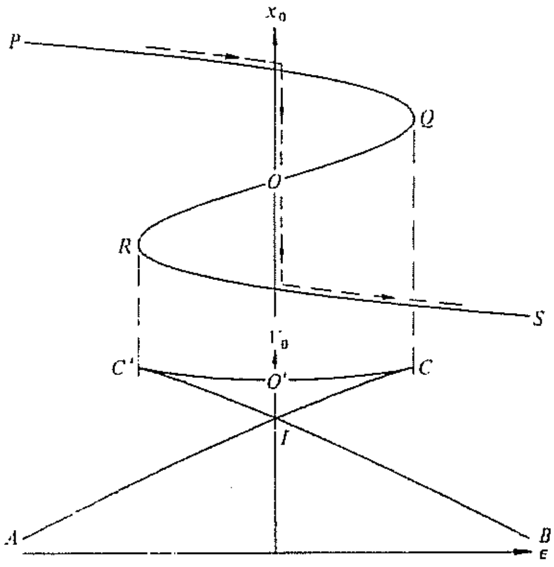

Figure 4: The illustration of the Maxwell convention.

b). The construction of the equilibrium values of potential $V_0(\epsilon)$, and the Maxwell convention.

To illustrate the Maxwell convention we will use the following form of the potential:

$$V(\epsilon) = \epsilon x - ax^2 + cx^4; \quad c > 0. \tag{6}$$

The values of V at the equilibrium positions, $V_0(x_0)$, depend on $\epsilon$and a. If we were to solve the cubic equation, $(\partial V/\partial x)_\epsilon = 0$ for x_0, and substitute back in V, we should learn little more about the form of V. To compute the cusp curve it is easy to choose x_0 and evaluate $\epsilon = 2ax_0 - 4cx_0^3$, and then to evaluate $V(x_0)$ directly to give $V_0(\epsilon)$; but to understand why it has this shape a simple trick is helpful. Consider $\int x_0 d\epsilon$, taken at the constant a; integration by parts reduces it to $\epsilon x_0 - \int \epsilon dx_0$, which is immediately integrable to yield the result apart from an insignificant constant;

$$V_0 = V(x_0) = \int x_0 d\epsilon. \tag{7}$$

Figure 4 shows how the integration of the many-valued upper curve yields the cusped lower curve.

The stretch PQ yields AC in the lower curve, and OQ yields O'C.

Since $\partial V_0/\partial \epsilon = x_0$, the two branches must have the same gradient at C, which is therefore a cusp of zero angle. A similar argument accounts for the rest of the curve. The cusp are present only if $a > 0$; when $a < 0$, V_0 is a single-valued function peaked at $\epsilon = 0$, but with no crossover.

The range QR describes points of unstable equilibrium, and hence CC' is not stably realizable, but only AC and BC'. The limit point instabilities are at C and C'; on climbing AC (ϵ increasing) the only thing to do at C is to fall back to the branch BC'. If it is possible to switch from branch to branch there is a continuous path available from A to B, with branch switching in I. This is indicated by the arrowed path on the top curve, and clearly involves switching the system from one minimum of V to the other at the point ($\epsilon = 0$) when they are equal. The two ways going from A to B, the irreversible path through the limit point C, or the reversible path involving a switch at I are possible. One must examine the physical system to discover which course it will take. If it is a ball rolling on a curve it will proceed to the limit point and then roll over to the other side. But a fluid obeying van der Waals' equation has the possibility of proceeding reversibly, through of a mixture of phases, from liquid to vapor, a process that the same as the reversible path we have just described.

c). Van der Waals's equation.

We introduce van der Waals' equation as an example of a cusp catastrophe, not as a contribution to the theory of phase transitions. Historically the equation played a central role in elucidating the transition between liquid and vapour; almost inevitably it came to be accepted as a valid model of critical behaviour, which it is not: It still has its uses, but must be treated with great caution, as discussed Pippard (1985). The details of what really happens at the critical point of a phase transition, are much more complicated than anything described by the theory of the cusp catastrophe. Superficially they may look alike, but to stop at the point reached by van der Waals is to accept a most unphysical description of one of the really important problems. Let us then take van der Waals' equation as a mathematical model showing interesting features in its own right.

Except that they are turned through 90°, the isotherms of van der Waals' equation, $(P + A/v^2)(v - b) = RT$, in the vicinity of the critical point are very similar curves of that shown in Figure 3. They can be approximated by cubic curves (Figure 5).

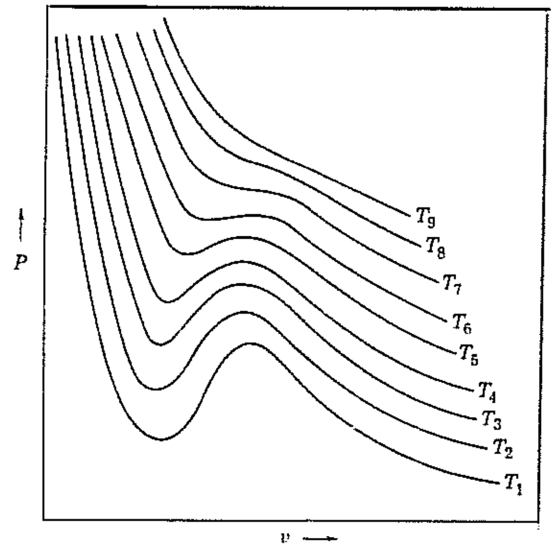

Figure 5: The isotherms of van der Waals' equation.

Before discussing the analogy further let us look critically at the isothermal transition between liquid and vapour, at any temperature below the critical one., which proceeds inhomogeneously along horizontal line of constant pressure, line LV in Figure 5.

According to Maxwell (1875) the areas between this line and the isotherm, one area above and one below, should be equal. This prescription is the same as is involved in the branch switch at I in Figure 4. To see this one must appreciate that in the thermodynamic system in equilibrium the role of V_0 is played by the Gibbs function per unit mass, $g = u - Ts + Pv$. A phase transition can take plays reversibly if the value of g for each phase is the same. The horizontal line must therefore be drawn so that $g_L = g_V$. Now $(\partial g/\partial P)_T = v$ so that $g = \int v dP$, the integral being evaluated along the isotherm. This integral generates a cusped curve for g, and intersection gives the value of P that must be chosen to make the integral from L to V vanish. This is the Maxwell's condition of equal areas.

This argument, however, suffers from a fundamental difficulty which is absent from a simple dynamical system, or one to which previous procedure can be applied. In the latter case V exists at all x and one can imagine the system traversing the whole curve; thus a ball rolling on a strip can be held at the point of unstable equilibrium by a gentle lateral constraint that does not alter V. By contrast the thermodynamic properties of the gas can be defined only in states of stable equilibrium, and the region of van der Waals' equation between maximum and minimum is totally unrealizable.

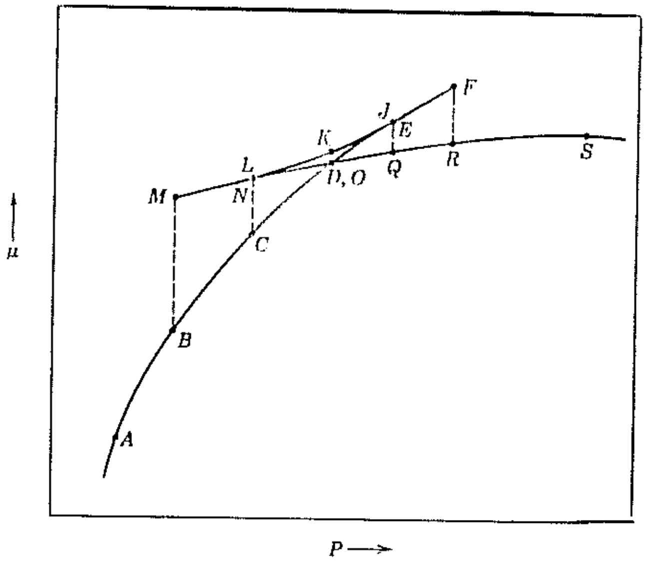

Figure 6: The electrochemical potential ,μ of the single component system versus pressure, P

9.2 Critical S-curves in the non-dissipative disk accretion case

Figure 3 in Chapter 5C shows the relationship between angular momentum in the critical point and location of the critical point. Notice that for $0 \leq T_c \leq T_*$ there are three critical points, as was also shown by Abramowicz and Zurek (1981) for conical flows. For the $T > T_*$ the flow has only the innermost critical point. The outermost and innermost critical points are saddle types and the middle one in a nodal type. Two saddle type critical points can, in principle allow two local stationary transonic solutions, however, only one of them can join the black hole horizon to the large distance (Lu and Abramowicz, 1988, Anderson, 1988, Abramowicz and Chakrabarti, 1988).

The cusp curve $\dot{M}$ versus E represented in Figure 7 was used by Abramowicz and Chakrabarti (1988) to discuss the nature of the various shock transitions.

9.3 S-curves - what can they tell us about the time dependent behaviour of the system.

By solving stationary equations describing transonic accretion flow, we get the S-shape relation for $\dot{M}(\Sigma)$. In the qualitative analysis of dynamical systems, such a solution is known as a relaxation oscillation. The time

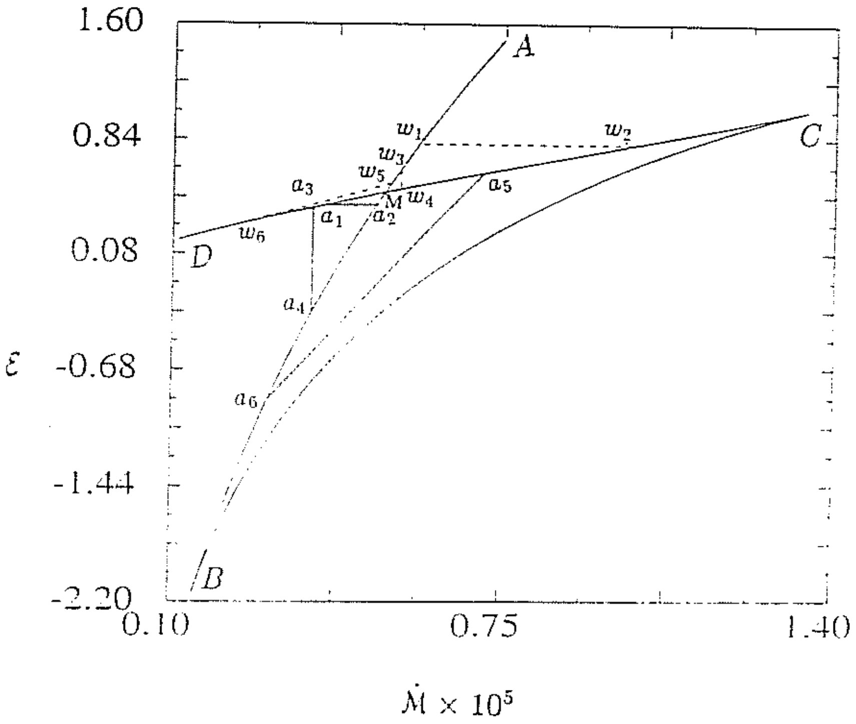

Figure 7: Variation of energy of the transonic flow with the accretion rate for a given angular momoentum

dependent equations for this oscillations are as follows (nonlinear oscillator, e.g. van der Pol oscillator):

$$\frac{dz}{dt} = \gamma(x - F(z)) \tag{8}$$

$$\frac{dx}{dt} = -\gamma^{-1}z \tag{9}$$

where γ is a damping constant, which should be in this case very large and F(z) is a known function of z.

Eliminating t we can get

$$\frac{z}{x} = -\gamma^2(x - F(z))\frac{1}{z} \tag{10}$$

$$\frac{x}{z}(x - F(z)) = -\frac{z^2}{\gamma} \approx 0 \tag{11}$$

It means

$$x = F(z).$$

Without solving these equations we know what is the phase portrait in (z,x) space.

Looking at the time dependent equations for accreting flow we can derive the local (for a fixed r) equations which are very similar to the nonlinear oscillator equations. This is straightforward for the dwarf novae case. The equations govern their structure are as follows (Meyer and Meyer-Hofmeister, 1984):

$$\frac{\partial\Sigma}{\partial t} = \frac{3}{r}(r^{1/2}\frac{\partial}{\partial r}[r^{1/2}f]) \tag{12}$$

where

$$f = \int_{-\infty}^{\infty} \mu dz \tag{13}$$

is the integral of the viscosity,

$$\frac{\partial f}{\partial t} + v_r\frac{\partial f}{\partial r} - \nu_{th}\frac{\partial^2 f}{\partial r^2} = -\frac{f}{\tau}[log\Sigma^*(f,r) - log\Sigma] \tag{14}$$

where $\Sigma = \Sigma^*(f,r)$ is the relation between surface density and viscosity in thermal equilibrium and ν_{th} is the thermal diffusivity. This equilibrium function has the characteristic S-shape in the region of partial ionization and convection which allows three different values of viscosity integral f

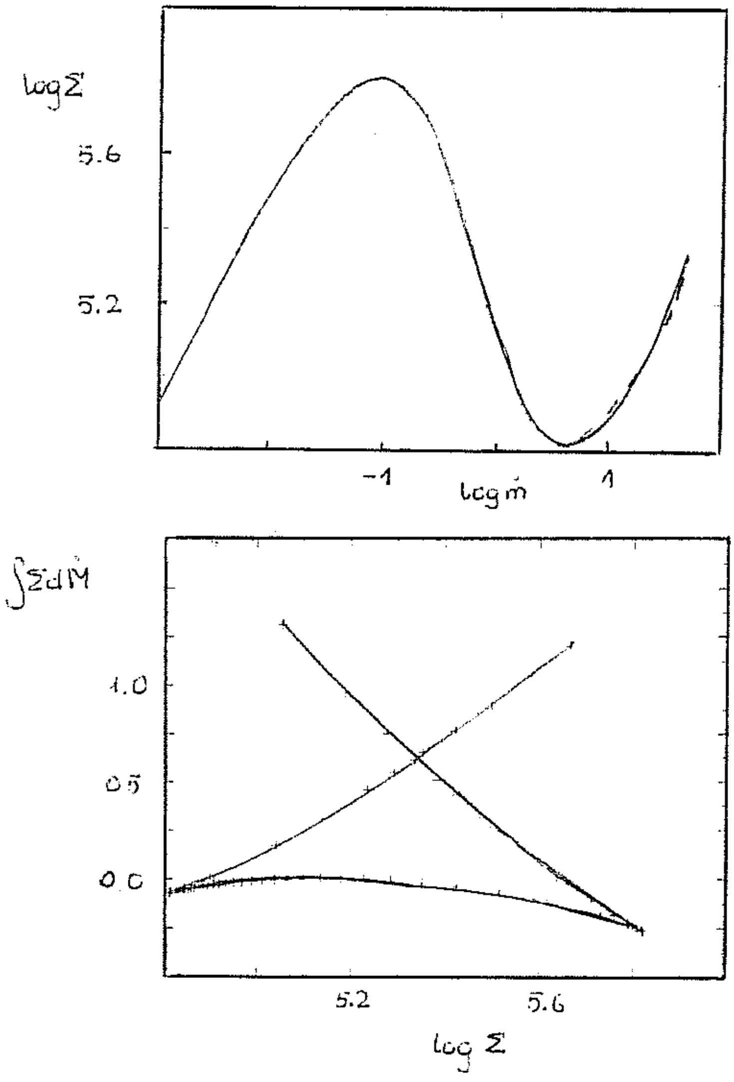

Figure 8: The $\dot{m}(\Sigma)$ relation and the cusp curve for the sequence of slim disks

for the same value of the surface density. In that case $1/\gamma$ from the equations (8) and (9) correspond to the thermal timescale, and γ to the viscous timescale. It must be stressed that it is crude approximation, we use the fact that these two timescales are not of the same order of magnitude.

Since we do not have strong arguments, but only intuition to guide we assume that the non-linear oscillator can work also in the case of slim disk (equation of mass conservation correspond directly to equation (9) with the γ^{-1} playing rôle of viscous timescale). The first step in the procedure is to fit the equilibrium solution by polynomial . Figure 8 shows the agreement for the fitting. The solid line represents the original results, the dashed line represents the polynomial approximation. We obtain the best

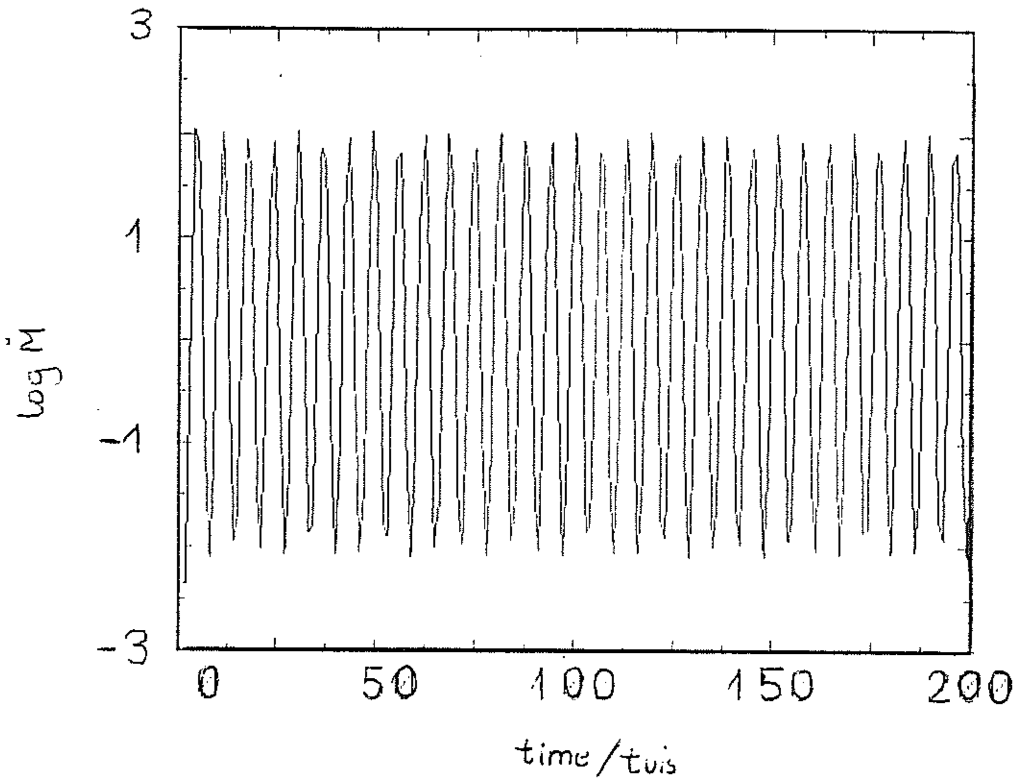

Figure 9: The time dependent behaviour of accretion rate in the non-linear oscillator approximation

(satisfactorily) numerical fit for polynomial of order 7.

The next step is to solve equations (1) and (2). We do it numerically for different values of γ. The results are shown in Figure 9.

The time scale involved are of order $1/\gamma$ for the fast jumps and of order γ for the slow traverses. The period can be evaluated by:

$$T \approx \int_E^B (-\frac{\gamma}{z} dx) = -2\gamma \int_E^B \frac{dz}{x} = -2\gamma \int_E^B -\frac{dz}{\gamma^2(x - F(z))} \tag{15}$$

The amplitudes of variability can be seen directly from S-curves when the cycle occur along ABDE. There is also irreversible path for the system to go from A to C.

9.4 Time dependent case

One can write the time dependent equation in the following way:

$$\frac{\partial\Sigma}{\partial t} = -\frac{1}{R}\frac{\partial}{\partial R}(R\Sigma v_R) \tag{16}$$

$$\frac{\partial l}{\partial t} = -v_R\frac{\partial l}{\partial R} + \frac{1}{R\Sigma}\frac{\partial}{\partial R}[R^3\nu\Sigma\frac{\partial}{\partial R}(\frac{l}{R^2})] \tag{17}$$

$$\frac{\partial v_R}{\partial t} = -v_R\frac{\partial v_R}{\partial R} + \frac{l^2}{R^3} - \frac{1}{\rho}\frac{\partial P}{\partial R} - \frac{GM}{(R-R_G)^2} \tag{18}$$

$$\begin{aligned}\frac{\partial T}{\partial t} = -v_R\frac{\partial T}{\partial R} - \frac{4-3\beta}{12-10.5\beta}\frac{T}{R}\frac{\partial}{\partial R}(Rv_R) + \\ \frac{T}{RP(12-10.5\beta)}\frac{\partial}{\partial R}(R\chi\frac{\partial T}{\partial R}) - \\ \frac{TF_z}{HP(12-10.5\beta)} + \\ \frac{T\Sigma\nu R^2}{2HP(12-10.5\beta)}[\frac{\partial}{\partial R}(\frac{l}{R^2})]^2\end{aligned} \tag{19}$$

This set of four partial differential equations with following algebraical relations give the full description of the behaviour in time of the disk:

$$P = \frac{a}{6} + [(\frac{a}{6}T^4)^2 + (\frac{\mathcal{R}}{4\mu B_4})\frac{\Sigma^2 T v_K^2}{R^2}]^{1/2} \tag{20}$$

$$H = \frac{2B_4R^2}{\Sigma v_K^2}P \tag{21}$$

$$\rho = \frac{\Sigma^2 v_K^2}{4B_4R^2P} \tag{22}$$

$$c_s = \frac{2B_4^{1/2}R}{\Sigma v_K}P \tag{23}$$

$$\nu = \alpha\frac{4B_4^{3/2}R^3}{\Sigma^2 v_K^3}P^2 \tag{24}$$

$$\beta = (\frac{\mathcal{R}}{4\mu B_4})\frac{\Sigma^2 T v_K^2}{R^2}P^{-2} \tag{25}$$

$$F_z = B_3\frac{2acT^4}{3\kappa\Sigma} \tag{26}$$

$$\chi = \frac{4acT^3}{3\kappa\rho} = \frac{16B_4R^2ac}{3\kappa\Sigma^2 v_K^2}T^3P \tag{27}$$

$$v_K = \frac{c}{\sqrt{2}}\frac{r^{1/2}}{(r-1)} \tag{28}$$

$$R = \frac{r}{R_G} \tag{29}$$

The meaning of all the quantities has been already given (e.g. Chapter 3).

The problem to find the solution of the time dependent equations of the slim disk structure is still open. However the first, necessary and not trivial step seems to be done. We have got the stationary solutions and now ... it is time for the next step.

References

Note: The frequently quoted book "Variability of Galactic and Extragalactic X-ray Sources", edited by A. Treves, Milano 1987, is referred to here as *Variability...*, ed. A. Treves.

Abramowicz, M.A., 1974, *Acta Astron.* **24**, 45.

Abramowicz, M.A., 1981, *Nature* **294**, 235.

Abramowicz, M.A., 1982, *Nature* **298**, 789.

Abramowicz, M.A., 1986, *Publ. Astron Soc. Japan* **37**, 727.

Abramowicz, M.A., 1987, in *Variability...*, ed. A. Treves., p. 137.

Abramowicz, M.A., 1987, in *General Relativity and Gravitation*, ed. M.A.H.MacCallum, Cambridge University Press.

Abramowicz, M.A., Blaes, O.M., and Ghosh, P., 1987, *Ap. J.* **323**, 629.

Abramowicz, M.A., Blaes, O.M., Lu, J., 1986, in *Structure and Evolution of Active Galactic Nuclei*, eds. G.Giuricin, et al., (Reidel, Dordrecht), p. 113.

Abramowicz, M.A., Calvani, M., and Madau, P., 1987, *Comments Astrophys.* **12**, 67.

Abramowicz, M.A., Calvani, M., and Nobili, L., 1980, *Ap. J.*, **242**, 772.

Abramowicz M.A., Calvani, M., and Nobili, L., 1983, *Nature*, **302**, 597.

Abramowicz, M.A., and Chakrabarti, S.K., 1988, preprint.

Abramowicz, M.A., Czerny, B., Lasota, J.P., and Szuszkiewicz, E., 1988 *Ap. J.* **332** , in press.

Abramowicz, M.A, Henderson, P.F., and Ghosh, P., 1983, *M.N.R.A.S.* **203**, 323.

Abramowicz, M.A., Jaroszyński, M., Sikora, M., 1978, *Astron. Astrophys.* **63**, 221.

Abramowicz M.A., and Kato, S., 1988, accepted to *Ap. J.*

Abramowicz, M.A., Lasota, J.P., and Xu, C., 1986, in *Quasars*, eds. G. Swarup and V.K. Kapahi, (Reidel, Dordrecht), p. 371.

Abramowicz, M.A., Livio, and Lu, J., 1986, in *Marcel Grossmann Meeting on General Relativity*, ed. R. Ruffini, (Elsevier, B.V.) p. 1467.

Abramowicz, M.A., Livio, M., Piran, T., and Wiita, P.J., 1986, *Ap. J.* **279**, 383 Abramowicz, M.A., Livio, M., Soker, N., and Szuszkiewicz, E., 1988,

in preparation.

Abramowicz, M.A., and Nobili, L., 1982, *Nature* **300**, 506.

Abramowicz, M.A., and Piran, T., 1980, *Ap. J. Lett.* **241**, L7.

Abramowicz, M.A., and Szuszkiewicz, E., 1988, in Proc.of *Big Bang, Active Galactic Nuclei and Supernovae*, eds Hayakawa, S., and Sato, K.Tokyo:Universal Academy Press, Inc.

Abramowicz, M.A., and Zurek, W.H., 1981, *Ap. J.* **246**, 314.

Antokhina, E.A., and Cherepaschuk, A.M., 1985, *Soviet Astron.* **29**, 654.

Antonucci, R.R., 1983, *Nature* **303**, 158.

Alloin, D., et al., 1985, *Ap. J.* **288**, 205.

Alloin, D., et al., 1986, *Ap. J.* **308**, 23.

Alloin, D., Boisson, C., Pelat, D., 1988, *Astron. Astrophys.* **200**, 17.

Altshuler, D.R., and Wardle, J.F.C., 1976, *M.N.R.A.S.* **82**,1.

Anderson, M., 1988, *M.N.R.A.S.* (submitted).

Angel, J.R.P., et al., 1978, in *Pittsburgh Conference on BL Lac Objects* ed. A.M. Wolfe, Pittsburgh: University of Pittsburgh Press.

Babadzanjanz, M.K., and Belokon, E.T., 1975, in *Variable Stars and Stellar Evolution*, IAU Symp. No. 67,(Reidel, Dordrecht).

Bailey, M.E., 1982 *M.N.R.A.S.* **200**, 247.

Barbieri, C., et al., 1983, *Mem. S. A. It.* **54**, 617.

Barbieri, C., et al., 1985, *Astron. Astrophys.* **142**, 316.

Barbieri,C.,Cappellaro, E., Romano, G.,Turatto, M., and Szuszkiewicz, E., 1988, accepted to *Astron. Astrophys. Suppl. Series*

Bardeen, J.M., 1973, in *Black Holes* eds. C. DeWitt and B. DeWitt, (Gordon and Breach, New York).

Barr, P., 1986, in *The Physics of Accretion onto Compact Objects*, eds., K.O. Mason, M.G. Watson and N.E. White, (Springer, Berlin).

Bassani, L., et al., 1983, *Astron. Astrophys.* **125**, 52.

Bath, G.T., and Pringle, J.E., 1982, *M.N.R.A.S.* **199**, 267.

Begelman, M.C., 1978, *Astron Astrophys.* **70**, 583.

Begelman, M.C., Blandford, R.C., and Rees, M.J., 1984, *Rev. Mod. Phys.* **56**, 255.

Begelman, M.C., McKee, C.F., and Shields, G.A., 1983a, b, *Ap. J.* **271**, 70, 89.

Begelman, M.C., and Rees, M.J., 1978, in *Pittsburgh Conference on BL Lac Object*, ed. A. M. Wolfe, University of Pittsburgh Press.

Bechtold, J., et al., 1987, *Ap.J.* **314**, 699.

Binette, L., Prieto, A., Szuszkiewicz, E., and Wei Zheng, 1988, submitted to *Ap.J.*

Blaes, O.M., 1985, *M.N.R.A.S.* **216**, 553.

Blaes, O.M., 1987, *M.N.R.A.S.* **227**, 975.

Blaes, O.M., and Glatzel, W., 1986, *M.N.R.A.S.* **220**, 253.

Blaes, O.M., and Hawley, J.F., 1988, *Ap. J.* **326**, 277.

Blandford, R.D., 1986, in *Superluminal Radio Sources*, eds. J.A. Zensus and T.J. Pearson.

Blandford, R.D., Jaroszyński, M., and Kumar, S., 1985, *M.N.R.A.S.* **215**, 667.

Blandford, R.D., and Rees, M.J., 1978, in *Pittsburgh Conference on BL Lac Objects*, ed. A.M. Wolfe.

Boss, A.P., 1988, *M.N.R.A.S.* **231**, 739.

Brandt, A., and Lanza, A., 1988, *Class. Quantum Grav.* **5**, 713.

Bregman, J.N., et al., 1986, *Ap. J.* **301**, 708.

Broadfoot, A.L., Duran, C.M., and Stalio, R., 1988, *Santa Maria: An International Orbiting Observatory for Multispectral (200 - 7000 A) Observations of Astrophysical and Solar System Objects.*

Burbidge, G., and Perry J., 1976, *Ap. J. Letters* **205**, L55.

Carter, B., and Luminet, J.P., 1982, *Nature* **296**, 211.

Cavaliere, A., and Morrison, P., 1983, *Ap. J. Letters* **283**, L63.

Cavaliere, A., et al., 1986, *Astron. Astrophys.* **156**, 33.

Chakrabarti, S.K., 1986, in *Accretion Processes in Astrophysics*, eds. D. Audouze and J.T.T. Van, (Editions Frontières, Gif-sur-Yvettes), p. 155.

Chakrabarti, S.K., et al., 1987, in *Supermassive Black Holes*, ed. M. Kafatos, (Cambridge University Press).

Chandrasekhar, S., 1961, *Hydrodynamic and Hydromagnetic stability*, (Dover, New York).

Clavel, J., 1988, preprint

Collin-Souffrin, S., 1986, *Astron. Astrophys.* **166**, 27.

Cox, A.N., and Stewart, J.N., 1970, *Ap.J. Suppl.* **19**, 243.

Czerny, B., 1983, Ph.D. Thesis

Czerny, B., and Czerny, M., 1986, in *New insights in Astrophysycs (8 years of UV Astronomy with IUE* ESA-SP 263.

Czerny, B., and Elvis, M., 1987, *Ap. J.* **321**, 305.

Danks, A.C., et al., 1979, *Ap. J. Letters* **227**, L59.

Deeming, T.J., 1975, *Astrophys. Space Sci.* **36**, 137.

Dent, W.A., and Balonek, T.J., 1980, *Nature* **283**, 747.

Dibai, E.A., 1980, *Sov. Astron.* **24**, 389.

Dibai, E.A., 1984, *Sov. Astron.* **28**, 245.

Drury, L.O'C., 1985, *M.N.R.A.S.* **217**, 821.

Elliot, J.L., and Shapiro, S.L., 1974, *Ap. J. Letters* **192**, L3.

Elvis, M., et al., 1985, *Ap. J.* **292**, 357.

Elvis, M., 1986, in *Quasars*, eds. G. Swarup and V.K. Kapahi, (Reidel, Dordrecht), p. 371.

Epstein, E.E., et al., 1982, *A. J.* **87**, 449.

Fabian, A.C., 1987, in *Variability...* , ed. A. Treves., p. 111.

Fabian, A.C., et al., 1986, *M.N.R.A.S.* **221**, 931.

Ferrari, A., Trussoni, E., Rosner, R., and Tsiganos, K., 1985, *Ap. J. Letters* **277**, L35.

Flammang, R.A., 1982, *M.N.R.A.S.* **199**,833.

Frank, J., 1979, *M.N.R.A.S.* **187**, 883.

Frank, J., King, A.R., and Raine, D.J., 1985, *Accretion power in Astrophysics*, Cambridge University Press.

Frank, J., and Robertson, J.A., 1988, *M.N.R.A.S.* **232**, 1.

Frohlich, A., 1973, *IAU Circ.* No. 2525.

Ghisellini, G., 1987, *M.N.R.A.S.* **224**, 1.

Glatzel, W., 1987, *M.N.R.A.S.* **225**, 227.

Goldreich, P.,Goodman, J., and Narayan, R., 1986, *M.N.R.A.S.* **221**, 339.

Goldreich, P., Narayan, R., 1985, *M.N.R.A.S.* **213**, 7P.

Goodman, J., and Narayan, R., 1988, *M.N.R.A.S.* **231**, 97.

Gorshkov, A.G., and Popov, M.V., 1972, *Astron. Zh.* **49**, 722.

Gott, J.r., and Gunn, J.E., 1974, *Ap. J. Letters* **190**, L105.

Guilbert, P.W., Fabian, A.C., and Rees, M.J., 1983, *M.N.R.A.S.* **205**, 593.

Hagen-Thorn, V.A., et al., 1977, *Pis'ma Astron. Zh.* **3**, No. 2.

Halpern, J.P., 1985, *Ap. J.* **290**, 130.

Hawley, J.F., 1986, in *Radiation Hydrodynamics in Stars and Compact Objects*, (Springer, Berlin).

Hawley, J.F., 1987, *M.N.R.A.S.* **225**, 677.

Hewitt, A., and Burbidge, G., 1987, *Ap. J. Suppl. Series* **63**, 1.

Hills, J.G., 1975, *Nature* **254**, 295.

Hills, J.G., 1988, *Nature* **331**, 687.

Hoshi, R., 1977, *Prog. Theoretical Phys.* **58**, 1191.

Ilovaisky, S.A., 1987, in *Variability...*, ed. A. Treves., p. 175.

Jaroszyński, M., Abramowicz, M.A., and Paczyński, B., 1980, *Acta Astron.* **30**, 1.

Joly, M., et al., 1985, *Astron. Astrophys.* **152**, 282.

Jurkevich, I., et al., 1971, *Astrophys. Space Sci.* **10**, 402.

Kato, S., et al., 1982, *Publ. Astron. Soc. Japan* **34**, 51.

Kato, S., Honma, F., and Matsumoto, R., 1988, *M.N.R.A.S.* **231**, 37.

Kato, S., and Matsumoto, R., 1988, in Proc.of *Big Bang, Active Galactic Nuclei and Supernovae*, eds Hayakawa, S. and Sato, K., Tokyo:Universal Academy Press, Inc.

Kemp, J.C., et al., 1986, *Ap. J.* **305**, 805.

Kidger, M.R., and Beckman, J.E., 1986, *Astron. Astrophys.* **154**, 288.

Kikuchi, S., et al., 1988, *Astron. Astrophys.* **190**, L8.

Kinman, T.D.,et al., 1968, *Ap. J.* **152**, 357.

Kinman, T.D., 1970, *Report at the Symp. IAU.* No. 44, Uppsala.

Kiplinger, A.L., 1974, *Ap. J. Letters* **191**, L109.

Kojima, Y., 1986, *Prog. Theor. Phys.* **75**, 251.

Kochanek, C.S., Shapiro, S.L., and Teukolsky, S.A., 1987, *Ap. J.* **320**, 73.

Kollatschyny, W., et al., 1981, *Astron. Astrophys.* **102**, L23.

Kormedy, J., 1987, in *Supermassive Black Holes* ed. M. Kafatos, Cambridge University Press.

Kozłowski, M., Jaroszyński, M., and Abramowicz, M.A., 1978, *Astron. Astrophys.* **63**, 209.

Krolik, J.H., 1988, *Ap. J.* **325**, 148.

Kwan, J., and Krolik, J.H., 1979, *Ap. J. Letters* **233**, L91.

Kwan, J., and Krolik, J.H., 1981, *Ap. J.* **250**, 478.

Lawrence, A., et al., 1985, *M.N.R.A.S.* **217**, 685.

Lawrence, A., 1987, *P.A.S.P.* **99**, 309.

Liang, E.P.T., Thompson, K.A., 1980, *Ap.J.* **240**, 27.

Lightman, A.P., 1974, *Ap. J.* **194**, 429.

Lightman, A.P., and Eardley, D.M., 1974, *Ap. J. Letters* **187**, L1.

Lü, P.K., and Hunter, J.H., 1969, *Nature* **221**, 755.

Lin, D.C.N., Pringle, J.E., and Rees, M.J., 1988, *Ap. J.* **328**, 103

Lin, D.C.N., and Shields, G.A., 1986, *Ap. J.* **305**, 28.

Loska, Z., 1982, *Acta Astron.* **32**, 13.

Lu, J.F., and Abramowicz, M.A., 1988, *Acta Astron. Sinica* **8**, 1.

Luminet, J.P., 1987, *Ann. Phys. Fr.* **12**, 23.

Luminet, J.P., Carter, B., 1986, *Ap. J. Suppl. Series* **61**, 219.

Lynden-Bell, D., and Pringle, J.E., 1974, *M.N.R.A.S.* **168**, 603.

Lyuty, V., 1979, *Sov. Astron.* **23**, 518.

Lyuty, V.M., and Pronik, V.I., 1975, in *Variable Stars and Stellar Evolution*, IAU Symp. No.67, (Reidel, Dordrecht), p. 592.

Madau, P., 1988, *Ap. J.* **327**, 116.

Malkan, M., 1983, *Ap. J.*, **268**, 582.

Malkan, M., and Sargent, W.C., 1982, *Ap. J.* **254**, 22.

Mardalajevic, J., et al., 1988, *Astrophys. Letters* **26**, 357.

Mark, J.W.-K., 1976, *Ap. J.* **205**, 363.

Matsumoto, R., Kato, S., Fukue, J., and Okazaki, A.T., 1984, *Publ. Astron. Soc. Japan* **36**, 71.

Maxwell, J.C., 1875, *Nature* **11**, 357.

McClintock, J.E., 1986, in *The Physics of Accretion onto Compact Objects*, eds., K.O. Mason, M.G. Watson and N.E. White, (Springer, Berlin).

McGimsey, B.Q., et al., 1975, *Astron. J.* **80**, 895.

McHardy, I., and Czerny, B., 1987, in *Variability...*, ed. A. Treves., p. 59.

Meyer, F., and Meyer-Hofmeister, E., 1981, *Astron. Astrophys.* **104**, 40.

Meyer, F., and Meyer-Hofmeister, E., 1983, *Astron. Astrophys.* **128**, 420.

Meyer, F., and Meyer-Hofmeister, E., 1984, *Astron. Astrophys.* **132**, 143.

Moncrief, V., 1980, *Ap. J.* **235**, 1038.

Morini, M., et al., 1986, *Ap. J.* **307**, 486.

Muchotrzeb, B., 1983, *Acta Astron.* **33**, 79.

Muchotrzeb-Czerny, B., 1986, *Acta Astron.* **36**, 1.

Muchotrzeb, B., and Paczyński, B., 1982, *Acta Astron.* **31**, 1.

Novikov, I.D., and Thorne, K.S., 1973, in *Black Holes* eds. C. DeWitt and B. DeWitt, (Gordon and Breach, New York).

Okazaki, A.T., Kato, S.,and Fukue, J., 1987, *Publ. Astron. Soc. Japan* **39**, 447.

Ostriker, J.P., and Vietri, M., 1985 *Nature* **318**, 446.

Ozernoy, L.M., and Chertoprud, V.E., 1966, *Soviet Astron.-A.J.* **10**, 15.

Ozernoy, L.M., and Usov, V.V., 1977, *Astron. Astrophys.* **56**, 163.

Pacholczyk, A.G., 1972, in *External Galaxies and Quasi-Stellar Objects* IAU Symp. No.44, p.165.

Paczyński, B., 1974, *Nature* **249**, 329.

Paczyński, B., 1978, *Acta Astron.* **28**, 91.

Paczyński, B., 1980, *Acta Astron.* **30**, 347.

Paczyński, B., 1986, *Ap. J.* **301**, 503.

Paczyński, B., 1987, *Nature* **325**, 572.

Paczyński, B., and Abramowicz, M.A., 1982, *Ap. J.* **253**, 897.

Paczyński, B., and Bisnovatyi-Kogan, G., 1981, *Acta Astron.* **31**, 283.

Paczyński, B., and Wiita, P., 1980, *Astron. Astrophys.* **88**, 23.

Papaloizou, J.C.B., Faulkner, J.,and Lin, D.N., 1983, *M.N.R.A.S.* **205**, 487.

Papaloizou, J.C.B., and Pringle, J.E., 1984, *M.N.R.A.S.* **208**, 721.

Papaloizou, J.C.B., and Pringle, J.E., 1987, *M.N.R.A.S.* **225**, 267

Peterson, B.M., 1988, *P.A.S.P.* **100**, 18.

Peterson, B.M., et al., 1985, *A.J.* **88**, 926.

Peterson, B.M., and Ferland, G.J., 1986, *Nature* **324**, 345.

Phinney, E.S., 1983, Ph.D. Thesis, University of Cambridge.

Pica, J.T., et al., 1980, *Astron. J* **85**, 1442.

Pippard, A.B., 1985, *Response and Stability*, Cambridge University Press.

Piran, T., 1978, *Ap. J.* **221**, 652.

Pollack, J.T., et al., 1979, *A. J.* **84**, 1658.

Pollock, J.T., et al., 1974, *Astron. Astrophys* **30**, 41.

Pounds, K.A., 1985, in *Galactic and Extragalactic X-ray Sources*, eds. Y. Tanaka and W.H.G. Lewin (Inst. Spac. Astronaut.

Sci.,Tokyo).

Pounds, K.A., et al., 1987, *M.N.R.A.S.* **224**, 443.

Pounds, K.A., and Turner, T.J., 1987, in Variability... , ed. A. Treves, p.1.

Press, W.H., Flannery, B.P., Teukolsky, S.A.,and Vetterling, W.T., 1986, Cambridge University Press.

Pringle, J.E., 1981, *Ann. Rev. Astr. Ap.* **19**, 137.

Pringle, J.E., and Rees, M.J., 1972, *Astron. Astrophys.* **21**, 1.

Pringle, J.E., Rees, M.J., and Pacholczyk, A.G., 1973, *Astron. Astrophys.* **29**, 179.

Rees, M.J., 1978, *Phys. Scripta* **17**, 193.

Rees, M.J., et al., 1982, *Nature* **295**, 17.

Rees, M.J., 1984, *Ann. Rev. Astr. Ap.* **22**, 471.

Rees, M.J., 1988, *Nature* **333**, 523.

Reike, G.H., and Lebofsky, M.J., 1979, *Ap. J.* **227**, 710.

Różyczka, M., and Muchotrzeb, B., 1982, *Acta Astron.* **32**, 285.

Salonen, E., et al., 1987, *Astron. Astrophys. Suppl. Ser.* **70**, 409.

Sanduleak, N., and Pesch, P., 1984, *Ap. J. Suppl. Series* **55**, 517.

Seguin, F.M., 1975, *Ap. J.* **197**, 745.

Schneider, P., and Weiss, A., 1987, *Astron. Astrophys.* **171**, 49.

Schul, H., and Rafanelli, P., 1981, *Astron. Astrophys.* **103**, 216.

Shakura, N.I., and Sunyaev, R.A., 1973, *Astron. Astrophys.* **24**, 337

Shakura, N.I., and Sunyaev, R.A., 1976, *M.N.R.A.S.* **175**, 613.

Shields, G.A., 1977, *Astrophys. Lett.* **18**, 119.

Shields, G.A., 1978, *Nature* **272**, 706.

Siemiginowska, A., and Czerny, B., 1988, preprint.

Sikora, M., 1981, *M.N.R.A.S.* **196**, 257.

Sikora, M., and Zbyszewska, M., 1986, *Acta Astron.* **36**, 255.

Sillanpää, A., et al., 1985, *Astron. Astrophys.* **147**, 67.

Sillanpää, A., et al., 1988, *Ap. J.* **325**, 628.

Smak, J.I., 1984, *P.A.S.P.* **96**, 5.

Smith, H.J., 1965, in *Quasi-Stellar Sources and Gravitational Collapse*, (University of Chicago Press), p. 221.

Smith, M.J., and Wolstencroft, R.D., 1970, *Astrophys. Space Sci.* **8**, 471.

Soltan, A., 1982, *M.N.R.A.S.* **200**, 115.

Stanger, V.J., and Pounds, K.A., 1986, preprint.

Stoeger, W.R.,1976, *Astron. Astrophys.* **53**, 267.

Stoeger, W.R.,1980, *Ap. J.* **235**, 216.

Svensson, R., 1987, *M.N.R.A.S.* **227**,403.

Schwartz, D.A., et al., 1979, *Ap. J. Letters* **229**, L53.

Tassoul, J.-L., 1974, *Theory of Rotation Stars*, (Princeton University Press).

Treves, A., Maraschi, L., and Abramowicz, M.A., 1988, *P.A.S.P.*, in press.

Turner, T.J., and Pounds, K.A., 1988, *M.N.R.A.S.* **232**, 463.

Ulrich, M.H., 1986, in *New insights in Astrophysycs (8 years of UV Astronomy with IUE* ESA-SP 263.

Urry, C.M., et al., 1987, in *Variability...*, ed. A. Treves, p.15.

Visvanathan, N., and Elliot, J.L., 1973, *Ap. J.* **179**, 721.

Wagner, R.M., 1986, *Ap. J.* **308**, 152.

Walker, R.C., et al., 1982, *Ap. J.* **257**, 56.

Walker, R.C., et al., 1984, in *IUE Symposium 110, VLBI and Compact Radio Sources*, eds. R.Fanti, K. Kellerman, and G.Setti (Dordrecht:Reidel).

Wandel, A., 1986, in *Structure and Evolution of Active Galactic Nuclei*, eds. G. Giurichin et al., Dodrecht:Reidel.

Wandel, A.,and Yahil, A., 1985, *Ap. J. Letters* **295**, L1

Wandel, A.,and Mushotsky, R.F., 1986, *Ap. J. Letters* **306**, L61

Warwick, R.S., 1986, in *The Physics of Accretion onto Compact Objects*, eds. K.O. Mason, M.G. Watson and N.E. White, (Springer, Berlin).

Webb, J.R., et al., 1988, *Astron. J* **95**, 374.

Wills, D., et al., 1980, *A. J.* **85**, 1555.

Wilson, A.S., et al., 1979, *M.N.R.A.S.* **187**, 109.

Wilson, D., 1984, *Nature* **312**, 620.

Wlerick,G., Westerlund, B., and Garnier, R., 1979, *Astron. Astrophys.* **72**, 277.

Wolf, M., 1916, *Astron. Nach.* **202**, 415.

Woltjer, L., 1959, *Ap. J.* **130**,38.

Zamorani, G. et al., 1984, *Ap. J.*, **278**, 28.

Zdziarski, A.A., and Lightman, A.P., 1987, in *Variability...* , ed. A. Treves., p. 121.

Zurek, W.H., and Benz, W., 1986, *Ap. J.* **308**, 123.